2014

Predictions of precipitation reaction mechanisms for 7xxx series aluminum alloys cast by CDS technique

Luca Sobrino
University of Windsor

Recommended Citation

Sobrino, Luca, "Predictions of precipitation reaction mechanisms for 7xxx series aluminum alloys cast by CDS technique" (2014). *Electronic Theses and Dissertations.* Paper 5177.

Predictions of precipitation reaction mechanisms for 7xxx series aluminum alloys cast by CDS technique

By

Luca Sobrino

A Thesis
Submitted to the Faculty of Graduate Studies
through the Department of Mechanical, Automotive & Materials Engineering
in Partial Fulfillment of the Requirements for
the Degree of Master of Applied Science
at the University of Windsor

Windsor, Ontario, Canada
2014

Predictions of precipitation reaction mechanisms for 7xxx series aluminum alloys cast by CDS technique

by

Luca Sobrino

APPROVED BY:

J. Sokolowski
Department of Mechanical, Automotive & Materials Engineering

D. Green
Department of Mechanical, Automotive & Materials Engineering

R. Riahi, Advisor
Department of Mechanical, Automotive & Materials Engineering

A. Sobiesiak, Co-Advisor
Department of Mechanical, Automotive & Materials Engineering

September 12, 2014

Declaration of originality

I hereby certify that I am the sole author of this thesis and that no part of this thesis has been published or submitted for publication.

I certify that, to the best of my knowledge, my thesis does not infringe upon anyone's copyright nor violate any proprietary rights and that any ideas, techniques, quotations, or any other material from the work of other people included in my thesis, published or otherwise, are fully acknowledged in accordance with the standard referencing practices. Furthermore, to the extent that I have included copyrighted material that surpasses the bounds of fair dealing within the meaning of the Canada Copyright Act, I certify that I have obtained a written permission from the copyright owner(s) to include such material(s) in my thesis and have included copies of such copyright clearances to my appendix.

I declare that this is a true copy of my thesis, including any final revisions, as approved by my thesis committee and the Graduate Studies office, and that this thesis has not been submitted for a higher degree to any other University or Institution.

Abstract

The need to reduce the fleet fuel consumption is pushing the automotive industry to reduce vehicles weight.

In this context high strength aluminum alloys are a viable alternative to the heavier steel currently adopted. In particular 7xxx series *wrought alloys*, thanks to their excellent strength to weight ratio, are drawing the attention of carmakers.

The development of the *Controlled Diffusion Solidification* (CDS) technique allows now the casting of these alloys into near net shapes, thus reducing all the costs related to the manufacturing process and making them attractive.

Because of the completely different microstructure resulting from the CDS process, a new design of the heat treatments is required to achieve the best mechanical properties.

This project therefore evaluates the macro and microhardness evolution of CDS cast 7xxx alloys in T4 and T6 conditions to predict their precipitation sequence, thus providing useful information for the heat treatments design.

A mia nonna,
per il suo affetto; questa laurea e' anche merito tuo.

Ai miei genitori,
per i loro insegnamenti e incoraggiamenti, e per il nostro bellissimo rapporto.

Ai miei nonni,
per essere ineguagliabili e sempre disponibili.

To my grandmother,
for her love; this degree is even because of you.

To my parents,
for their teachings and encouragements, and for our beautiful relationship.

To my grandparents,
for being incomparable and always available.

Acknowledgements

This project is the result of the double degree program set up between Politecnico di Torino and University of Windsor, with the collaboration of Fiat Group Automobiles and Chrysler LLC; I would therefore thank all the people involved in its organization.

With particular regard to the thesis itself, I would like to express my gratitude to Mohammed Malik from Chrysler LLC, for having introduced me to the research group of Chrysler LLC and McMaster University; this thesis is indeed a small part of the wide research born from the collaboration between these two institutions. On the other side instead, I am truly grateful to Stephen Logan, from Chrysler LLC, and to Dr. Shankar, from McMaster University, for having allowed me to take part in this project and for sharing their deep knowledge with me.

An active and essential contribution in the organization of the experimental part was provided by my Advisor at the University of Windsor, Dr. Riahi, to whom I am profoundly thankful.

The understanding of the different processes underlying the analyzed topic was made possible by the continuous explanations of Reza Ghiaasiaan, from McMaster University, who I sincerely thank for his availability and patience.

I besides express my gratitude to Kora Farokhzad, Gang Li, Andrew Jenner, Bruce Durfy and Dean Poublon from the University of Windsor, for being very helpful during the execution of the experiments.

I further want to thank my Advisors from Politecnico di Torino, Prof. Maizza and Prof. Belingardi, together with Fabio D’Aiuto from Fiat Group Automobiles, for their support and suggestions.

I am also grateful to my Co-Advisor, Dr. Sobiesiak, and to the committee members, Dr. Green and Dr. Sokolowski, for their considerations, which helped me refining my thesis.

A huge “thank you” is owed to my friends Francesca, Luca and Marco, for helping me with the experiments when I needed it.

I will never thank enough my parents who, once again, allowed me to take part in this beautiful experience, and continuously encouraged and advised me. What I am today

is all because of you. I would besides express my apologies to my Dad, but having an engineer in the family is better than having a doctor.

I am deeply grateful to my girlfriend Ilaria, for her patience and understanding over the past year. We knew it wouldn’t have been easy, but we made it through this.

I would eventually thank all my adventure fellows, Francesca, Luca, Federico, Giuseppe, Marco, Tom, Ashley and Kyle, and Felicia (aka 19), for the great times spent together.

Table of contents

List of tables

List of figures

List of appendices

List of abbreviations

MPGe	Miles per gallon equivalent
CDS	Controlled diffusion solidification
DSC	Differential scanning calorimetry
SSSS	Super saturated solid solution
VRC	Vacancy rich clusters
GPI	Guinier Preston zone type I
GPII	Guinier Preston zone type II
TTP	Time temperature property
TEM	Transmission electron microscope
SEM	Scanning electron microscope
SAD	Selected area diffraction
3DAP	3D Atom probe
RT	Room temperature
UTS	Ultimate tensile strength
YS	Yield strength
El. %	Elongation at fracture
HRF	Hardness Rockwell F
HV	Hardness Vickers
IP	Incubation period

Nomenclature

σ_y	Yield Strength [MPa]
σ_0	Resistance of the lattice to dislocation motion [MPa]
k_y	Strengthening coefficient [MPa*mm$^{1/2}$]
d	Average grain size [mm]
N_v	Total number of vacancies
N	Total number of atomic sites
Q_v	Energy required for the formation of a vacancy [J]
k	Boltzmann's constant [$\frac{J}{atom\ k}$]
T	Temperature [K]
e_0	Penetration depth when minor load is applied [mm]
e_2	Penetration depth when major load is removed [mm]
F	Vickers applied load [g]
l	Arithmetic mean of the diagonals of a Vickers indentation [µm]

1. Introduction

Nowadays one of the main challenges for the automotive industry is the reduction of the average fleet fuel consumption. In fact, the growing concerns on global warming and the greenhouse effect, together with a slight worry about the provision of fossil fuels for the future, pushed many governments to establish strict legislations for vehicles fuel consumption.

The main responsible factor for the greenhouse effect, and therefore for global warming is CO_2, whose production is directly related to the type and quantity of fuel burnt. Even though the main sector that releases CO_2 into the environment is the industry, precautions and new rules in the automotive segment were needed as well.

For this reason Mr. Obama, after decades of immobility on fuel consumption legislations in the US, introduced new stringent parameters to be met by vehicles.

The following graph illustrates as an example the trend of fuel efficiency regulations for passenger cars and light duty trucks[1] between 1978 and 2025 in the US.

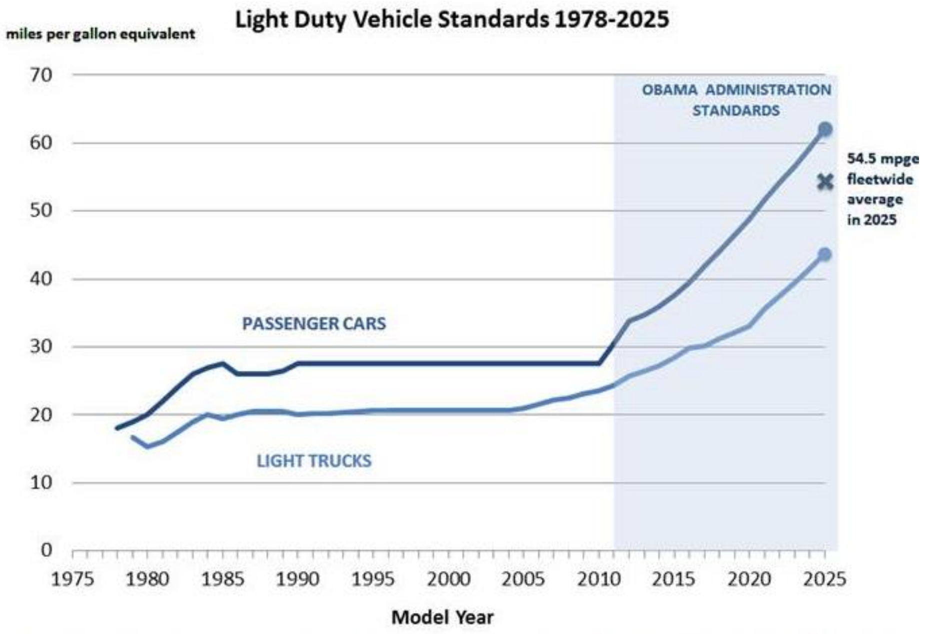

Figure 1.1: US fuel effinciency standards for cars and light trucks [1].

---

[1] According to the United States Environmental Protection Agency (EPA), passenger cars are those vehicles with a gross weight lower than 8500 lbs. Light duty trucks are characterized instead by a maximum gross weight of 8500 lbs, a maximum curb weight of 6000 lbs and a maximum frontal area of 45 ft^2 [47].

The *miles per gallon equivalent* (MPGe) present on the *y* axis is a measure to compare the fuel efficiency of alternative fuel vehicles to that of gasoline driven ones, so that all the different types of propulsions are comparable to each other. For instance the electricity used by electric cars is converted into MPGe through the relationship 33.7 KWh = 1 MPGe [1].

According to the figure above the challenge carmakers have to face is apparent, since they have to move the actual fleet average from 33 MPGe up to 54.5 MPGe in 11 years. For the sake of clarity it is better to reiterate that these values refer to vehicles that enter the market in the shown year, and not to those already present on the streets.

One of the most obvious ways to lower fuel consumption and improve MPGe figures is the reduction of vehicles weight. According to different studies, indeed a 10% mass reduction leads to fuel savings between 1.9% and 3.2% in gasoline engines and between 2.6% and 3.4% in diesel engines; these values refer to non re-sized powertrains. Instead, in the case of re-sizing to match the lower vehicle weight, fuel saving would be more conspicuous that what is shown [2].

Weight reduction is usually achieved by designing smaller components or, more frequently, by replacing heavy materials with lighter ones. In this particular context, aluminum alloys, together with other light materials such as magnesium and titanium, have been preferred to the heavier steel alloys in some applications. This replacement though could deteriorate the properties of the new parts, if precautions are not taken.

Generally lighter alloys do not provide the same mix of properties in strength, fatigue, impact toughness and corrosion resistance as steel does. It is therefore necessary to be careful in the selection of light alloys according to the different requirements of the components; for instance magnesium is adopted in parts without a structural function, such as steering wheel and seats skeletons, because of its low strength [3]. When structural parts are concerned though, aluminum alloys are generally adopted. Nevertheless their mechanical properties are usually lower than steel, so that aluminum components have to be designed with bigger cross sections with respect to steel ones. Then the low aluminum density, one third of the steel, is not fully exploited since the addition of material decreases the theoretical weight loss.

The need to further reduce vehicles weight in order to meet the legislation requirements is now pushing the automotive industry to focus on high strength aluminum alloys which have never been used in this sector. The adoption of stronger alloys would in fact allow the design of smaller cross sections and would therefore result in a lower weight.

Particular interest is drawn by 7xxx series alloys which, in the *wrought* composition, has strength higher than the *cast* composition, are already widely employed in the aerospace industry because of their high strength to weight ratio [4, 5]. The tendency of *wrought alloys* to develop cracks, when cast into near net shapes, requires however that they are cast into ingots and subsequently submitted to metal forming processes such as rolling and forging to reach the desired final shape. All these processes obviously increase the cost of the component, which is why 7xxx series aluminum alloys have never been attractive for carmakers [6].

With the development of the *Controlled Diffusion Solidification* (CDS) process these alloys can now be cast into finite shapes, so that all the costs related to metal forming processes are eliminated and they become suitable for carmakers [7, 8].

To obtain the desired mechanical properties 7xxx alloys are then submitted to precipitation hardening heat treatments. Though, due to the characteristic microstructure resulting from the CDS technique, new heat treatments, different from those implemented for conventionally cast products, need to be designed. A fundamental step in this design is the understanding of the microstructure evolution during the precipitation hardening steps [9].

The aim of the present project is therefore to analyze the microstructural changes and precipitates evolution in CDS cast 7xxx *wrought alloys* submitted to T4 and T6 heat treatments. This evaluation was carried out through microhardness and macrohardness measurements performed during the ageing stage.

2. Objective

7xxx aluminum *wrought alloys* have to be cast into ingots if conventional casting techniques are employed. The final product is indeed the result of different metal forming processes that, through different phases, change the shape of the ingot into the desired one. As it will be better explained in the next chapter, while being submitted to these processes the material undergoes a phenomenon known as work hardening, meaning that during deformation its strength increases. The final mechanical properties of conventionally cast 7xxx alloys are therefore the result of both material composition and work hardening.

With the CDS technique instead components are no longer the output of deformation processes, since the material is directly cast into semi finite shapes. By doing so, all the costs related to the forming steps are eliminated and 7xxx *wrought alloys* are thus affordable for the automotive industry. Nevertheless the strength increase is eliminated as well, so that a new hardening method has now to be adopted to obtain the desired mechanical characteristics.

Since 7xxx series aluminum alloys are age hardenable, meaning their strength can be enhanced through precipitation hardening as discussed in the next chapter, they are usually submitted to heat treatments, so that small precipitates form inside the microstructure improving the mechanical properties [5, 10, 4]. The most widely implemented heat treatment is the T6, since it leads to the highest strength, even though T4 treatments could be adopted as well. The differences between T4 and T6 are going to be addressed in the next chapter.

At this point of the discussion an objection could be raised against the CDS casting – heat treatment production process; the CDS process was developed with the aim of lowering manufacturing costs, but the need to submit the final parts to heat treatments increases the costs again. This is certainly true, since T6 and T4 treatments are expensive; nevertheless their costs are lower than those of forming processes. As a matter of fact, all the costs related to the manufacturing of dies used to deform ingots are avoided with the CDS - heat treatment sequence, where the only needed die is the casting one. In addition, given the material composition does not change, several components with different geometries can be submitted simultaneously to the same heat treatment, whereas each geometry requires its own die and deformation sequence. Moreover, the possibility to store many components in the furnace at the same time reduces the operating costs as well.

Finally it should be mentioned that conventionally cast products, to further enhance their strength, are sometimes heat treated as well, in which case the economic advantage of the CDS is even bigger. On the other side from the table below, comparing the uniaxial tensile properties of conventionally cast – forged – T6 treated samples with those of CDS cast – T6 treated ones, it is clear how the absence of deformation processes does not necessarily penalize the strength of CDS cast components.

Table 2.1: Uniaxial tensile properties of Al 7050 submitted to T6 heat treatment [9].

Process	**UTS [MPa]**	**YS [MPa]**	**El. %**
Forging	570	469	11
CDS	551	540	1.2

The figure for the *Ultimate Tensile Strength* (UTS), the stress at which cracks propagate in the part, is almost the same between the two samples. Regarding the *Yield Strength* (YS), which is the most relevant parameter to evaluate the strength of a component since it measures the stress at which deformation occurs, CDS samples are instead characterized by a value higher than 71 MPa with respect to forged ones. On the other side the *Elongation at Fracture* (El. %), the percentage elongation at which fracture occurs, presents a very low value in CDS components.

The data overall indicate how the CDS casting – T6 treatment sequence is a viable alternative to the conventional one, since the obtained values of strength are encouraging. Nevertheless, from a careful analysis, it is clear how the studied CDS samples are characterized by a brittle behavior (similar UTS and YS values with a very low El. %), meaning they fail at very low deformations and almost suddenly. Obviously such a behavior is not desirable in mechanical components, therefore the design of a new specific heat treatment is required.

The parameters of the adopted T6 treatment were indeed assumed from publications on conventionally cast 7xxx series alloys. Then, since the microstructure resulting from the CDS technique is completely different, as it will be explained in the next chapter, it is likely that the material evolution mechanisms are different as well, so that newly designed heat treatments are required. For a proper design, in turn, it is essential to understand how the microstructure behaves during the precipitation hardening stages, especially during the last stage, ageing, when precipitates nucleate in the material matrix [9].

The study of the precipitation sequence is therefore the first fundamental step in the conception of an optimized heat treatment that would eventually lead to the implementation of CDS cast 7xxx series aluminum components in the automotive industry.

The objective of this project is then to predict the precipitation reactions taking place in CDS cast samples during the T4 and T6 treatments. In doing so, the cost effectiveness of the treatments will not be taken into account, since the only aim is the analysis of precipitates evolution. In fact the optimization of the production process will be the objective of another project that will move from the results here obtained.

The analysis will be carried out through macrohardness and microhardness measurements which, by indenting the material surface, provide a direct measure of the resistance of the matrix to be deformed, hence of its strength. The measurements will be performed at different time steps during the ageing phase, so that curves showing the hardness trend will be obtained.

The results are expected to be similar to Figure 2.1, where the same type of study was carried out on an A356.2 Al alloy. The microhardness variation with respect to ageing time is illustrated in the case of natural ageing (T4 heat treatment).

Since the different precipitation stages and compounds variously affect the resistance of the matrix to indentation, from the curves variations it is possible to make hypotheses on the type of precipitates present in the microstructure at a determined time.

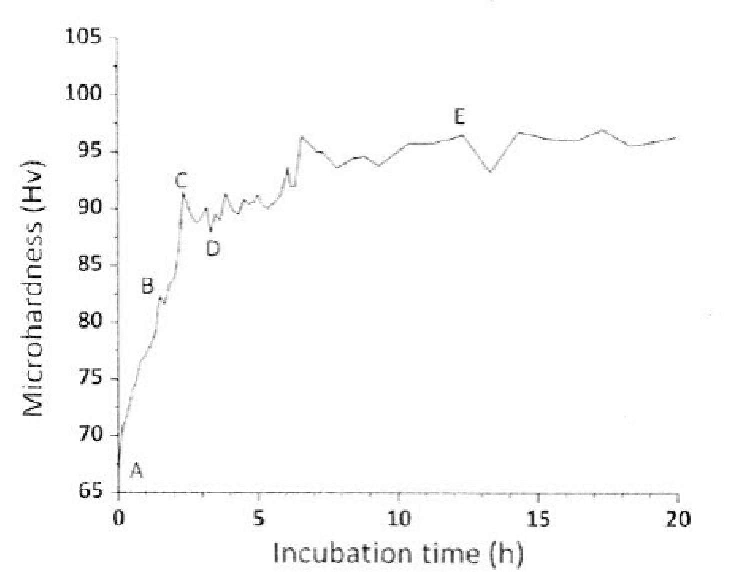

Figure 2.1: Microhardness values as a function of natural ageing (incubation) time at room temperature. Letters show the different steps in the precipitation sequence [11].

It is essential to stress that only the trend of the hardness curves will be analyzed during this project and not the values of hardness reached in the different conditions, unless as a mean of comparison between the trends of different curves. Once again this is because the aim is to predict the precipitation sequence from the variation of the material hardness, and not to explore in which conditions the samples achieve their highest strength.

For the same reason a direct relationship between the measured hardness and the material strength is not sought here.

3. Literature review

The methodology and the theory behind the *Controlled Diffusion Solidification* process will be analyzed in this section, together with the mechanisms involved in the precipitation hardening of 7xxx series aluminum alloys.

3.1 *Controlled Diffusion Solidification* process

As previously mentioned, the impossibility to cast 7xxx series aluminum *wrought alloys* into near net shapes through conventional casting techniques led to the development of the *controlled diffusion solidification* (CDS) process.

Due to their chemical composition, these alloys are characterized by a dendritic microstructure if conventionally cast. Dendrites, in turn, by hindering a proper flow of the liquid metal into the shrinkage cavities being formed during solidification, are responsible for the development of defects such as hot tears, when the final part is a near net shape (Figure 3.1 (b)) [7, 8].

This is why generally aluminum *wrought alloys* are cast into ingots and subsequently submitted to metal forming processes to obtain the desired final shape.

Figure 3.1: Differences between samples cast with the CDS process (a) and a conventional casting technique (b) [9].

Although, with the development of the CDS process, aluminum *wrought alloys* can now be cast directly into their final shapes without the occurrence of casting defects, so that the cost of the final products is suitable for the automotive industry.

The absence of hot tears in CDS products is directly related to a microstructure characterized by globular grains (Figure 3.2 (a)), since this is an ideal condition for a proper filling of the interdendritic cavities by the liquid metal during solidification.

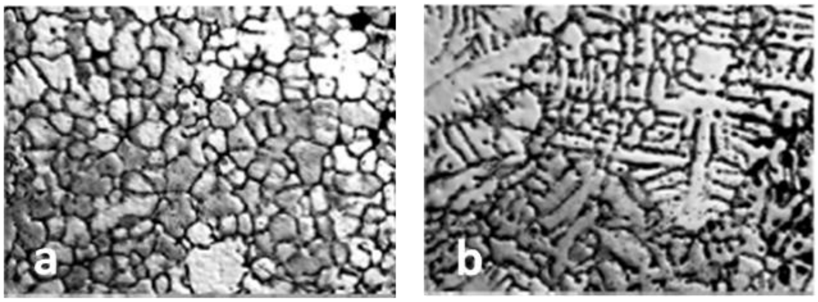

Figure 3.2: Comparison between microstructures obtained through the CDS process (a) and a conventional casting technique (b) [7].

The differences between the two types of microstructures (Figure 3.2 (a)-(b)) are attributable to the different mechanisms involved in the CDS process.

In the CDS process, whose principles have been described by different authors [7, 8, 9, 6, 12, 13], the target alloy (Alloy 3) results from the mixing of two precursor alloys: one pure (Alloy 1), or with a very low percentage of alloying elements, and another one with a higher solute concentration (Alloy 2). The liquid metal is poured into the mold just when the mixing between these two alloys is complete (Figure 3.3).

Three parameters concerning the precursor alloys need to be selected: their composition, their amounts and their liquid temperatures. They are determined according to five boundary conditions: the desired chemical composition of the final alloy and four fundamental requirements of the CDS process, which are stated below.

The two starting alloys must be characterized by low superheats, meaning their liquid temperatures should be slightly higher than their respective liquidus temperatures (temperature below which solid nuclei begin to form). Besides, the difference between the liquid temperature of Alloy 1 and the liquid temperature of Alloy 2 should be at least 50 – 80 °C. The mass ratio between the precursor alloys should be at least 3, with Alloy 1 in higher quantity. Lastly, once Alloy 1 and Alloy 2 have been mixed, the maximum temperature reached by Alloy 3 should be higher than its liquidus temperature [9, 12].

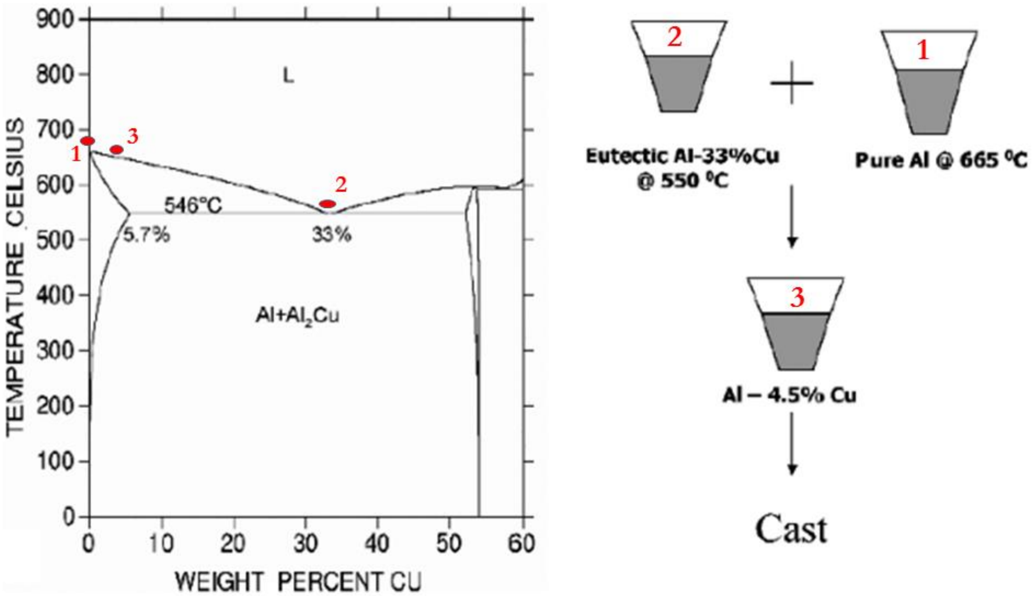

Figure 3.3: Phase diagram of Al-Cu alloys and mixing principle of the CDS process for an Al-Cu alloy. The respective compositions and liquid temperatures of the precursors and final alloys are shown in the phase diagram [7].

The temperature profile resulting from the mixing of the precursor alloys is shown in Figure 3.4.

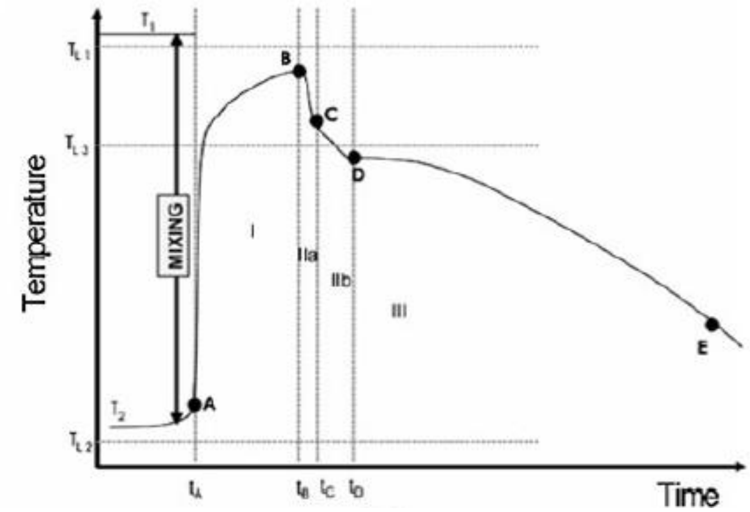

Figure 3.4: Temperature-time curve of the final alloy showing the three phases typical of the CDS process. T_{L1}, T_{L2} and T_{L3} are respectively the pure alloy, the solute containing alloy and the resulting mixture liquidus temperature [13].

The above figure can be divided into three regions: *mechanical mixing* (AB), *redistribution of the thermal and solute field* (BD) and *final nucleation* (DE) [9, 12].

During the *mechanical mixing* stage, Alloy 1 at temperature T_1 is poured into Alloy 2 at temperature T_2. As Figure 3.4 shows, the temperature of the resultant mixture never exceeds the liquidus temperature of Alloy 1 (T_{L1}). As a result Alloy 1, being in an environment much colder that its liquidus temperature, starts to nucleate. Indeed, since this stage lasts for a couple of seconds only, solute atoms diffuse from Alloy 2 to Alloy 1 but not sufficiently to lower the liquidus temperature of the second alloy and prevent its nucleation [9, 12, 13].

The amount of nuclei being formed during this stage determines the grain size of the final microstructure. In fact, a copious nucleation results in a higher number of grains and therefore in smaller grains. A proper selection of the precursor alloys and the adherence to the aforementioned requirements, promotes a copious nucleation. In addition grain refinement techniques could be adopted to increase the nuclei density.

At point B the system is characterized by a high density of small Alloy 1 solid nuclei, surrounded by a liquid mixture of Alloy 3 above its liquidus temperature T_{L3}. Here the solute concentration and the temperature fields of the mixture, as a function of the distance from the solid interface, have a trend such as that shown in Figure 3.5 (a).

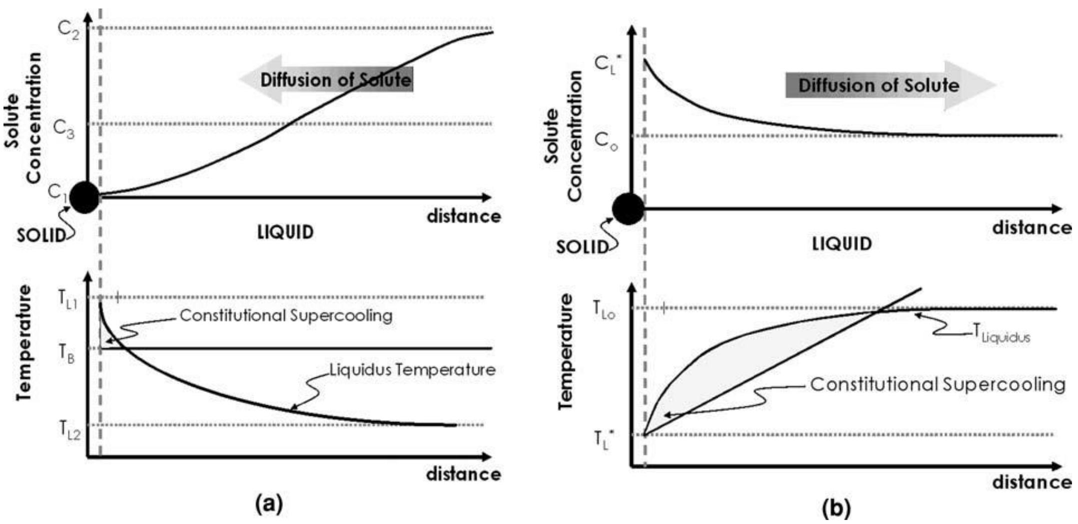

Figure 3.5: Solute and temperature profiles at the solid/liquid interface for a CDS (a) and a conventional casting technique (b) [12].

It is in the difference between the two solute fields of the above figure that lies the reason for which a globular microstructure is obtained in the CDS process whereas dendrites are present in a conventionally cast sample.

At the end of the *mechanical mixing* stage the concentration of solute atoms increases with the distance from the solid interface. This is because, as already mentioned, solute atoms do not have enough time to diffuse from Alloy 2 to Alloy 1 (solid particle) during mixing. Therefore, during the *redistribution of the thermal and solute field* stage, solute atoms flow towards the solidifying interface.

On the other side, in the conventional casting technique the concentration of solute decreases with the distance from the solid interface. This is because the solidifying liquid rejects solute atoms, which pile up at the solid interface. Therefore, since the system tends to equilibrium, solute diffuses away from the solidifying interface during solidification.

As it can be seen from the phase diagram in Figure 3.3, the concentration of solute deeply affects the liquidus temperature of a material; more precisely the higher the concentration the lower the liquidus temperature and vice versa. Then, in the CDS process, the liquidus temperature is higher at the solid interface than in the liquid solution. In a conventional casting instead the liquidus temperature increases with the distance from the solid nuclei.

Looking at the liquid temperature trend of the solidifying solution (straight lines in the temperature profiles of Figure 3.5) it is then possible to notice how the supercooling, namely the negative difference between the temperature of a liquid and its liquidus temperature, decreases in the CDS process and increases in a conventional casting.

Thus, since with a high level of supercooling the tendency to form dendrites during solidification increases, it can be explained why in the CDS process the already formed nuclei continue to grow globularly in the second region.

Once the liquidus temperature becomes homogenous throughout the mixture (point C in Figure 3.4) and the solute as well is evenly distributed in the remaining liquid (point D in Figure 3.4) the *final nucleation* stage begins, where the solidification mode is the same of a conventional casting technique [12].

In the last stage therefore, the formation of dendrites would be expected. Nevertheless, due to the amount of material already solidified the space available for their growth is limited. Thus the overall microstructure of the material is characterized by globular grains [9, 12].

A typical light optical micrograph of a 7050 CDS cast alloy, in the as cast condition, is shown in the figure below.

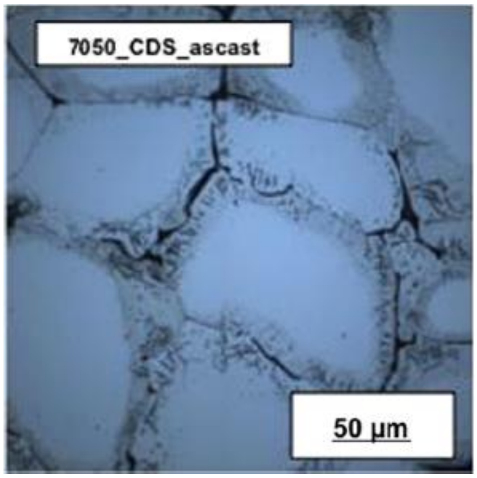

Figure 3.6: Light optical micrograph of a 7050 CDS cast alloy in the as cast condition [9].

It is possible to see how the grains become darker from the center towards the grain boundaries. This characteristic is linked to the particular solidification mechanism taking place in the CDS process, where the nuclei formed during the *mechanical mixing* stage are of pure Alloy 1, with a very low concentration of solute, from which the lighter color at the center of the grains results. In the following stage solute atoms diffuse towards the solidifying interface while grains grow globularly, so that color evolves into darker tones. The dark grey bands and the black regions at the grain boundaries are instead the eutectic phases being formed during the *final nucleation* stage, where the CDS process is similar to a conventional casting technique [9].

Having discussed the novelty and advantages of this innovative casting technique, it should be mentioned that a possible drawback of the CDS process is linked to the impossibility of the reuse of scrap coming from cast parts. Indeed, as already explained, two precursor alloys are needed for a successful operation and these alloys cannot be obtained by melting final products.

To reduce material waste and therefore costs, the design of the adopted mold has to be as close as possible to the final shape of the product. The remaining scrap can then be reused in a conventional casting aimed at producing parts whose final shape can be obtained through low cost metal forming processes that wouldn't justify the implementation of the CDS technique.

3.2 Precipitation hardening

Al-Zn-Mg-Cu alloys are usually submitted to different heat treatments to enhance their strength through a process called precipitation hardening or age hardening [5, 14].

They are indeed characterized by a high decrease in solid solubility of alloying elements such as Zn, Mg and Cu with decreasing temperature, meaning the solubility limit of these elements in the Al matrix is much lower at lower temperatures, which is the main requirement for an alloy to be heat treatable [15]. As a matter of fact, if an alloy which does not exhibit this property was submitted to an age hardening heat treatment its mechanical properties wouldn't be affected to a great extent.

With precipitation hardening small solute rich phases called precipitates are formed throughout the material matrix. They act as an obstacle to dislocations motion, so that a higher energy is required to deform a part, meaning the material is stronger.

It should be reiterated here that dislocations are linear crystalline defects of the lattice, involved in the material deformation. More precisely, a component deforms because of the movement of dislocations, which results in a shift of atoms in the crystalline structure and therefore into an atomic change of shape. Considering the high density of dislocations ($10^8 \frac{cm}{cm^3}$ in undeformed metals [16]) the overall effect of their simultaneous motion leads to the sample deformation. It is therefore clear how anything hindering dislocations motion results in an increase of the material strength.

The strengthening mechanism deriving from the interaction between precipitates and dislocations is illustrated in the figure below.

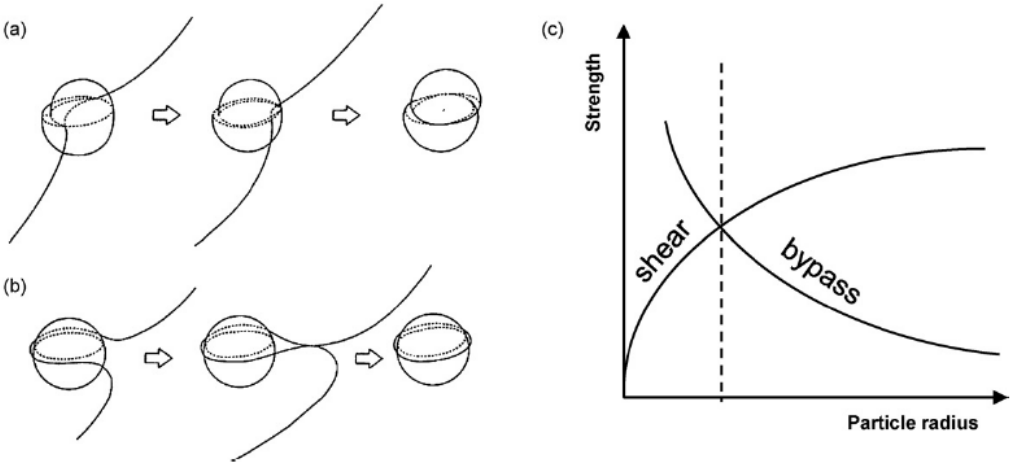

Figure 3.7: Dislocations passing precipitates by shearing (a) or bowing (b). (c) Dependance of the strength from the precipitates radius when sheared or bypassed by a dislocation [17].

When dislocations encounter obstacles during their motion they overcome them by shearing (Figure 3.7 (a)) or bypassing (Figure 3.7 (b)) them. As usual, the chosen method is the one that requires the least amount of energy.

As Figure 3.7 (c) shows, the material strength and therefore the required energy associated with each method depends on the radius of the particles to be passed. Below a certain threshold the energy required to shear the precipitate is lower than that required to bypass it; therefore dislocations choose the former way. Above that threshold instead dislocations bypass the precipitate, since shearing would require more energy. It will be explained later in this section how this mechanism is crucial in the design of the different precipitation hardening heat treatments.

In this project two different heat treatments will be analyzed: T4 and T6. They both are made of the same sequence of thermal cycles: solution heat treatment, quenching and ageing (Figure 3.8, Figure 3.9).

During solution treatment the material is heated up to a temperature above its solvus line; the temperature line (dashed line in Figure 3.8) below which β solute rich second phases begin to form into the aluminum matrix α. After a varying holding time the sample is then quenched and brought back into the phase diagram region where β second phases are present again. Finally, in T6 heat treatments, the part is held for a varying time at temperatures below the solvus line, otherwise, in T4 heat treatments, it is kept at room temperature (RT). In the former case the ageing process is addressed as artificial ageing and as natural ageing in the latter.

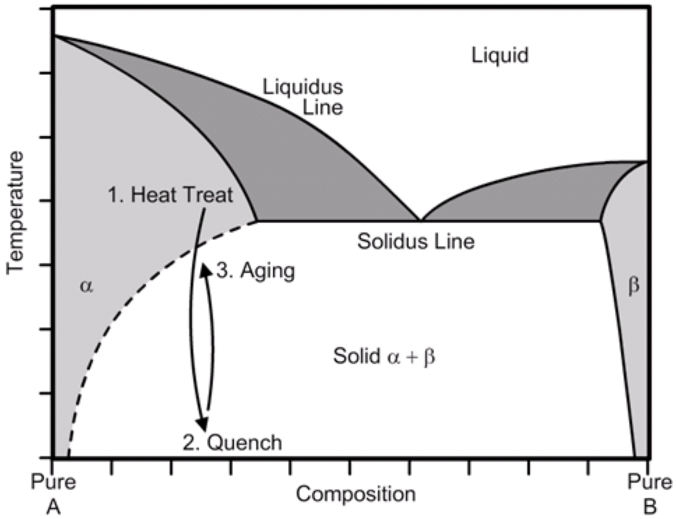

Figure 3.8: Generic phase diagram showing the three different thermal cycles required in precipitation hardening T6 heat treatment [18].

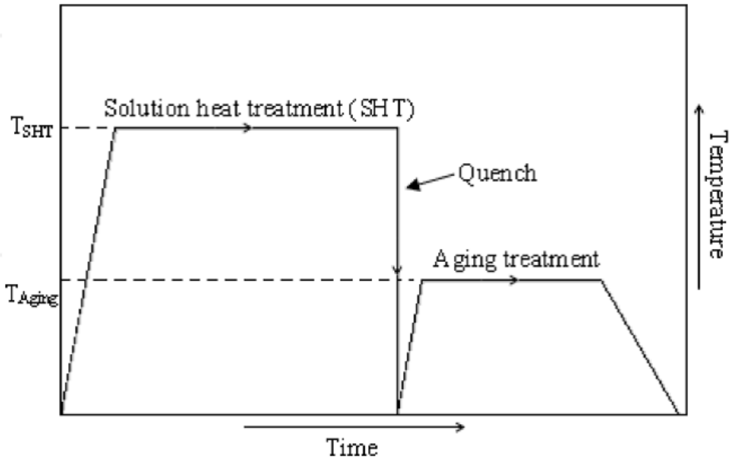

Figure 3.9: Temperature trend in a T6 heat treatment [19].

While in conventionally cast 7xxx *wrought alloys* precipitation hardening heat treatments may not be performed, they become essential in CDS cast alloys. In the case of conventional casting techniques the final part is obtained through metal forming processes. These, deforming the material, increase the density of dislocations ($10^{12}\,\frac{cm}{cm^3}$ in deformed metals [16]) and consequently the probability that their motion will be hindered. As a consequence the material strength is increased as well; this phenomenon is called work hardening.

In CDS castings instead the final product is still in the as-cast condition. Therefore precipitation hardening is the only available means to obtain an enhancement of the material strength.

3.2.1 As cast microstructure

Before giving a detailed explanation of the microstructure changes related to the different steps of precipitation hardening heat treatments, the features of CDS 7xxx aluminum *wrought alloys* microstructure in the as cast condition should be discussed.

As already mentioned for Figure 3.6, grains are characterized by a growing concentration of solute atoms from the center towards the grain boundaries. During the *final nucleation* stage instead part of the remaining liquid solidifies into eutectic structures at the grain boundaries. The solidification path followed by the liquid solution of a 7050 alloy in the last region of Figure 3.4, where the composition has become homogeneous, is shown in the figure below.

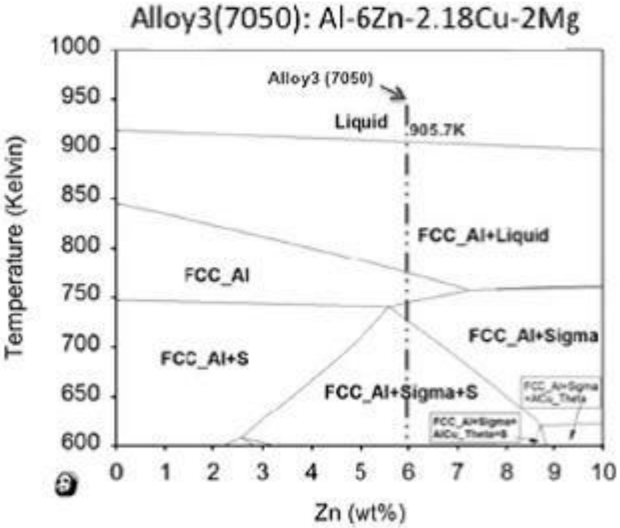

Figure 3.10: Example of a simulated section of multi-component phase diagram of a AA7050 having the shown chemical composition [9].

Following the dashed line, representing the indicated chemical composition, and starting from the liquid region above 905.7 K (632.55 °C) it is possible to notice how, with decreasing temperature, the first phase to solidify is the main aluminum matrix having a FCC crystal structure. Then, at a temperature close to 750 K (476.85 °C), the first eutectic phase Sigma $Mg(Zn,Cu,Al)_2$ forms while the S eutectic phase $CuMgAl_2$ appears at lower temperatures [9].

When the material is further cooled down (section not shown in Figure 3.10) the θ phase Al_2Cu appears. Besides, in the presence of impurity elements such as Fe and Si, intermetallic compounds like Mg_2Si and rod-like Cu_2FeAl_7 are visible [9].

It should be repeated that intermetallic compounds, differently from second phases, only form at a precise composition. This is because in their crystal structure atoms occupy a specific position, while in a normal phase solute atoms randomly replace atoms of the main matrix [20]. This characteristic results in a very high stability, which affects the behaviour of the alloy to solution treatment, as will be explained in the following section.

A SEM image of a CDS cast 7050 alloy in the as cast condition is shown in the figure below.

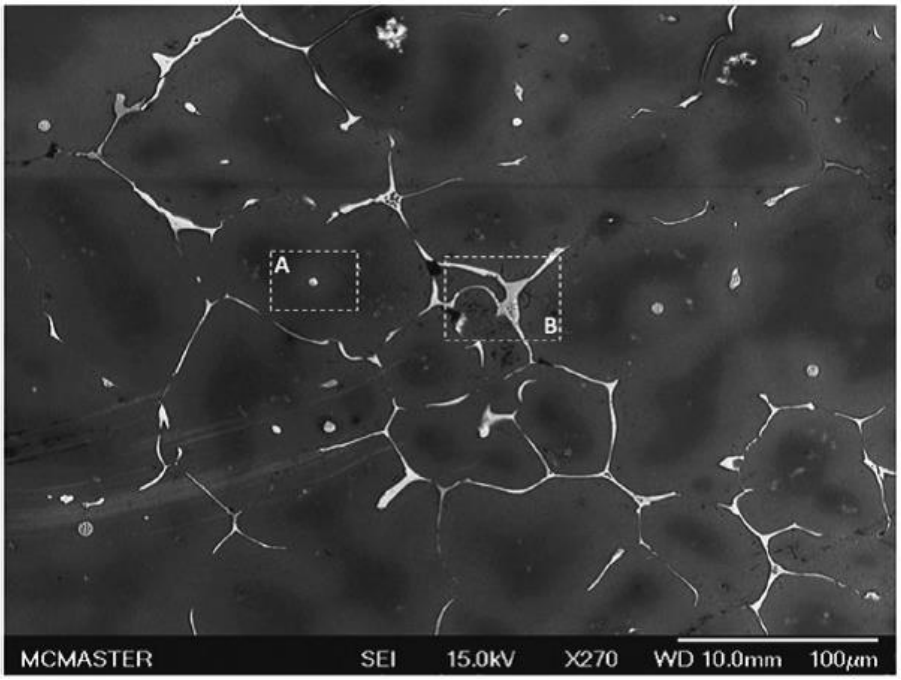

Figure 3.11: SEM microstructure of CDS cast 7050 samples in the as cast condition [9].

Differently from Figure 3.6, where just few grains were analyzed, it is clearly visible how eutectic phases (white regions) do form at the grain boundaries (box B), but at the same time they may also be present in small amounts inside the main aluminum matrix (box A). It is even useful to notice again how the as-cast microstructure is characterized by globular grains. A focus on the eutectic phases of the two highlighted regions is provided below.

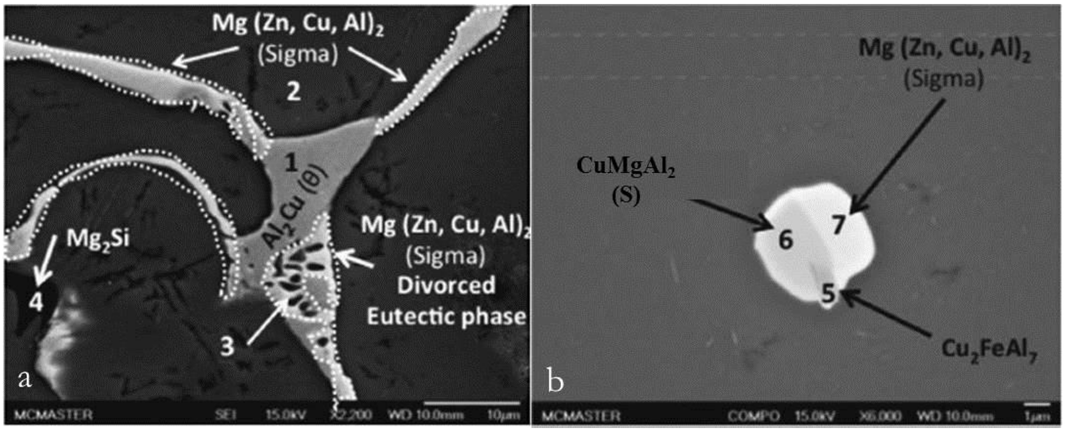

Figure 3.12: Magnified view of the eutectic structures of regions A (a) and B (b) in Figure 3.11 [9].

It is interesting to notice how in region B the S and Sigma phases grew around Cu_2FeAl_7. This means that eutectic phases form inside the grains when there are impurities acting as nucleating sites, such as intermetallic compounds, or alternatively when they form from late solidifying liquid [9].

3.2.2 Solution treatment

As previously mentioned, the solution treatment consists in heating the material up to a temperature above its solvus line (Figure 3.8), in a region of the phase diagram where all the second phases formed during solidification dissolve into the main material matrix, so that solute atoms become available for precipitation hardening.

However some eutectic phases do not dissolve completely during solution treatment, but their shape is profoundly modified by the thermal cycle. Generally they appear more rounded than before the treatment, thus the strength of the material is increased. It should be pointed out here that sharp and acicular phases, acting as stress concentration sites, increase the chance of crack propagation during deformation, so that failure occurs earlier.

Lastly, besides second phase dissolution and modification, the high temperatures adopted in the first step of the T4 or T6 heat treatments enhance the homogenization of solute atoms already dissolved into the aluminum matrix [17, 19, 21]. Indeed, in the as cast condition, solute atoms are not evenly distributed throughout the metal matrix. Particularly in the case of CDS castings it was explained how solute concentration varies from the center towards the edges of the grains. When submitted to high temperatures instead atoms can diffuse easily and again, since every system tends to the lowest energy condition, they distribute homogeneously in the matrix. This occurs because solute atoms, having different sizes with respect to aluminum atoms[2], introduce stresses inside the material which are lower when solute atoms are equidistant, meaning they are evenly distributed.

Two parameters have to be properly set in the design of a solution treatment process: temperature and time. Time should be selected according to the industrial costs, meaning that beyond a certain period the gain in phase dissolution is so low not to justify a further use of energy. On the other side though, a too short holding time may not allow the occurrence of the three aforementioned effects.

As far as what concerns the temperature, it has a major effect on the dissolution of eutectic phases; high temperatures lead to high atoms mobility and therefore to a better dissolution of second phases, given a constant solutionizing time. This relationship is confirmed by the following graph.

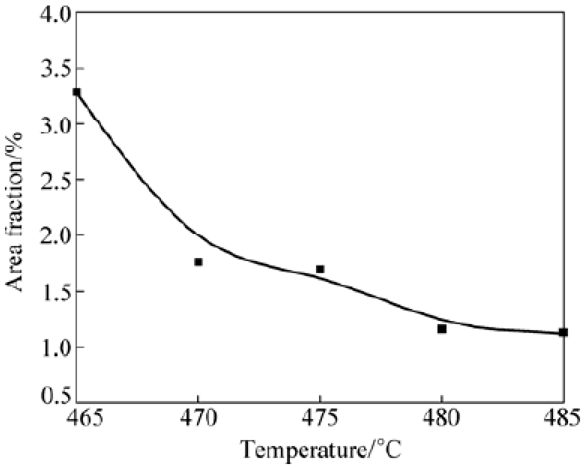

Figure 3.13: Area fraction of residual second phases as a function of solution treatment temperature in a AA7050 alloy [4].

Figure 3.14 illustrates the microstructure evolution of a conventionally cast 7055 alloy related to the different temperatures adopted in the solutionizing step.

The amount of eutectic phases at the grain boundaries is drastically reduced with respect to the as cast condition (Figure 3.14 (a)) and the higher the solutionizing temperature the lower the remaining fraction. Moreover those phases still visible present a globular shape, since they underwent a profound transformation.

---

[2] Zn, Mg and Cu atoms have respective sizes of 142 pm, 145 pm and 145 pm compared to Al atom size of 118 pm [46].

It is finally worthwhile to observe how the microstructure of this alloy, cast with a conventional technique, does not present globular grains.

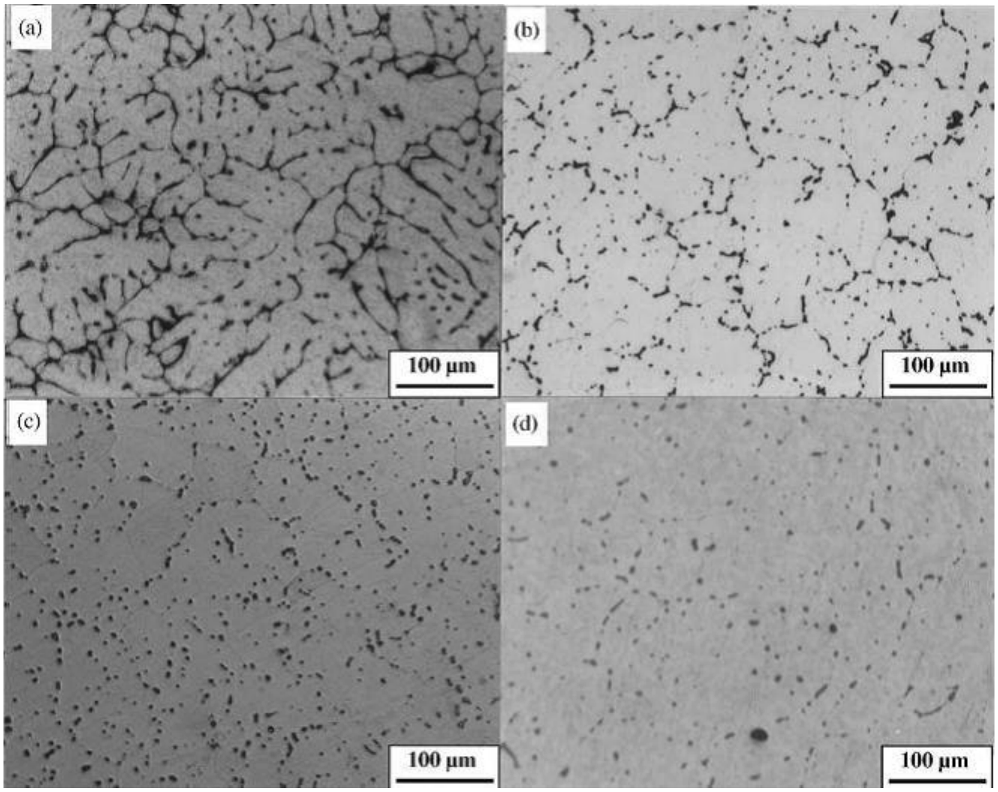

Figure 3.14: Optical micrographs of 7055 alloy ingots in the as cast condition (a) and after 50 h of solution treatment at 455 °C (b), 470 °C (c) and 475 °C (d) [22].

A high dissolution of eutectic phases is desirable, since it increases the saturation level of the metal matrix and therefore its precipitation hardening response; too high solution treatment temperatures should be avoided instead to prevent the phenomenon of incipient melting [23]. This consists in the non-equilibrium melting of the residual phases, meaning that they melt at a temperature lower than the one expected from the phase diagram. This usually occurs when phases characterized by high stability, which would need a long time to be dissolved, are heated up too quickly above their dissolution temperature[3].

The main drawback of incipient melting is related to the formation of porosities in the subsequent quenching step. In fact, when cooled down the molten metal solidifies but, being surrounded by a solid matrix and not by liquid as during casting solidification, its shrinkage is

---

[3] The dissolution temperature is equal to the solvus temperature and varies according to the material composition.

not compensated by any flow of liquid. Therefore small voids are left in the matrix. These porosities, diminishing the cross area of the component, increase the stress level, given the same loading conditions, and therefore lead to early failure of the part [23, 24].

The relationship between percentage porosity and solution temperature is illustrated in the figure below. The graph is purely demonstrative since the alloy analyzed belongs to the Al-Si-Cu system.

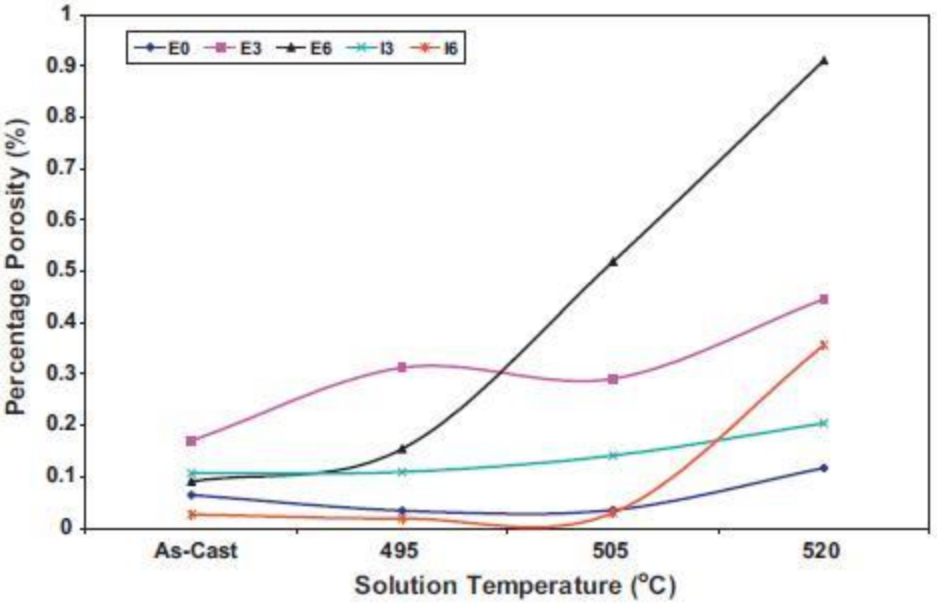

Figure 3.15: Relationship between percentage porosity and different solution treatment conditions for 319 experimental alloys with 0.0017 wt % (E0), 0.2675 wt % (E3) and 0.588 wt % (E6) of Mg, and 319 industrial alloys with 0.2945 wt % (I3) and 0.6 wt % (I6) of Mg [23].

The different behaviours of the tested compositions are related to the amount of Mg that, reducing the incipient melting temperature, strongly influences the percentage porosity [24].

What is useful to observe is that, no matter the composition, the higher the solution temperatures, the higher the molten phases and therefore the higher the amount of voids formed during quenching.

Solution treatment temperatures are therefore usually selected according to the incipient melting temperature, which can be detected with a differential scanning calorimetry (DSC).

In this device samples and a reference material can be either cooled down or heated up. Based on the difference between the heat delivered to the sample and to the reference, the DSC outputs a curve showing the relationship between heat flux and sample temperature.

Since phase formation and dissolution are respectively exothermic and endothermic processes, their occurrence is then shown by the curve trend. In the particular case of incipient melting the quantity of heat delivered to the sample is greater than to the reference; therefore a negative endothermic peak is visible [25].

A typical DSC curve relative to the incipient melting in a 7050 aluminum alloy is represented by Figure 3.16.

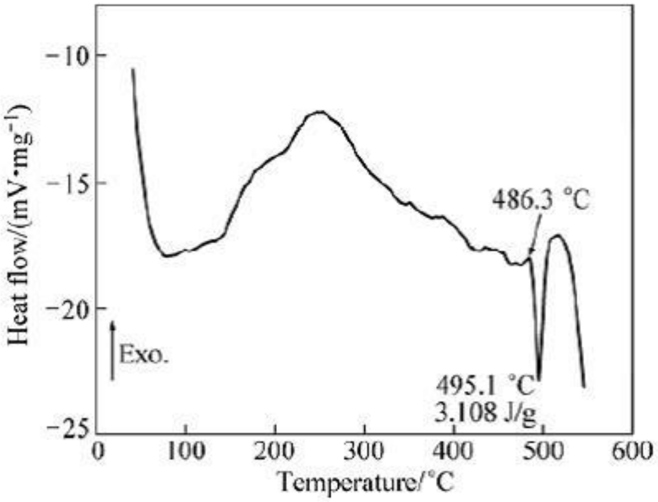

Figure 3.16: Results from the DSC experiments for as rolled AA7050 [4].

The endothermic peak begins at 486.3 °C, which is then the maximum acceptable temperature during a solution treatment.

More generally, according to the different material composition, it was found that the incipient melting temperature for 7050 alloys varies in the range between 482 °C and 486 °C [9, 4, 26].

It is common belief that the phase responsible for incipient melting in 7050 alloys is the S $CuMgAl_2$ phase. Because of its stability it does not dissolve earlier than $Mg(Zn,Cu,Al)_2$ Sigma phase, as it would be expected according to the equilibrium phase diagram of Figure 3.10, so that if the adopted temperature is too high it locally melts before dissolving.

S is therefore the main eutectic phase present in the microstructure after solution treatment, as illustrated by Figure 3.18.

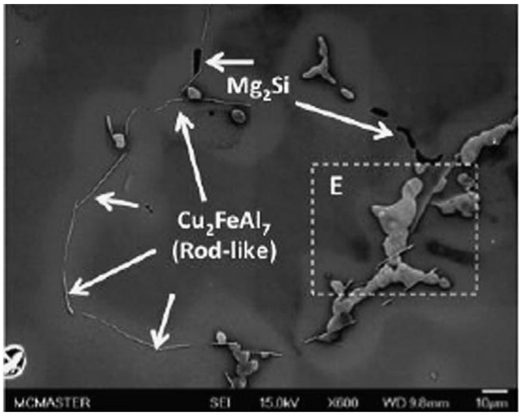

Figure 3.17: SEM micrograph of a CDS cast 7050 alloy after solution treatment and quenching [9].

Comparing the above image to Figure 3.12 (a) the reduction of eutectic phases following the solution treatment is visible. It is essential to observe then how solution treatment does not decrease the amount of intermetallic compounds, which actually increases. This is because these compounds dissolve at much higher temperatures than those adopted. The only effect visible on them is instead related to their shape which, in the case of iron intermetallic Cu_2FeAl_7, could evolve from rod like to bulk like (not present in Figure 3.17) [9].

According to the magnified image of region E, presented below, S is the predominant phase in the as quenched condition. Small fractions of Sigma are still visible inside S, whereas Al_2Cu completely dissolved during solution treatment and Cu atoms became available for the formation of Cu2FeAl7 and CuMgAl2, or simply distributed in the Al matrix [9].

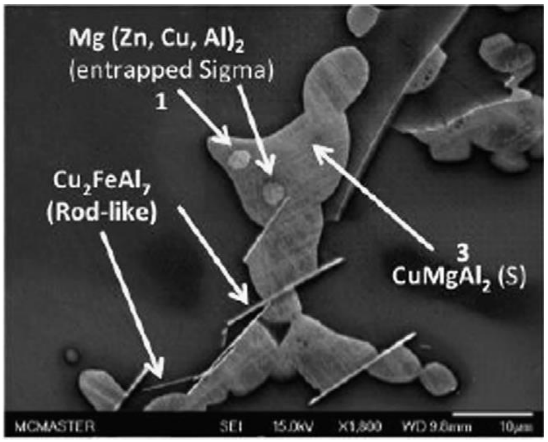

Figure 3.18: Magnified SEM image of the eutectic phases and intermetallic compounds of region E in Figure 3.17 [9].

It should be pointed out here that, besides material composition, another parameter which deeply affects the incipient melting temperature is the solution treatment heating rate.

For 319 aluminum alloys Chen et al. found that the incipient melting temperature could be raised as much as 10°C by lowering the heating rate to 0.5 °C/min. This is because it would help the dissolution of eutectic phases before the treatment temperature is achieved [27].

Xu et al. found instead in AA7150 alloys that the same effect could be achieved by increasing the heating rate from 10 °C/min to 50 °C/min [28]. In this case though it is likely the shift is not related to a better dissolution of second phases, but to the reaction lag of the microstructure to temperature changes. Indeed it is easy to understand how, assuming the microstructure takes a constant time to react to a temperature change, melting is registered at a higher temperature if the material is heated up faster. Therefore this method shouldn't be considered significant to explain the mechanisms taking place during solution treatment.

An alternative method to improve the dissolution of second phases and prevent incipient melting at low temperatures is to solutionize a sample in two or three different steps. The same principle of the slow heating rate applies as well; by solution treating a part below incipient melting temperature for a variable amount of time, a lower fraction of second phases is left when the temperature is increased, so that incipient melting occurs at a higher temperature and a higher quantity of solute atoms can be dissolved in the matrix [22, 29, 30]. The effect of a double step solution treatment is presented in the image below.

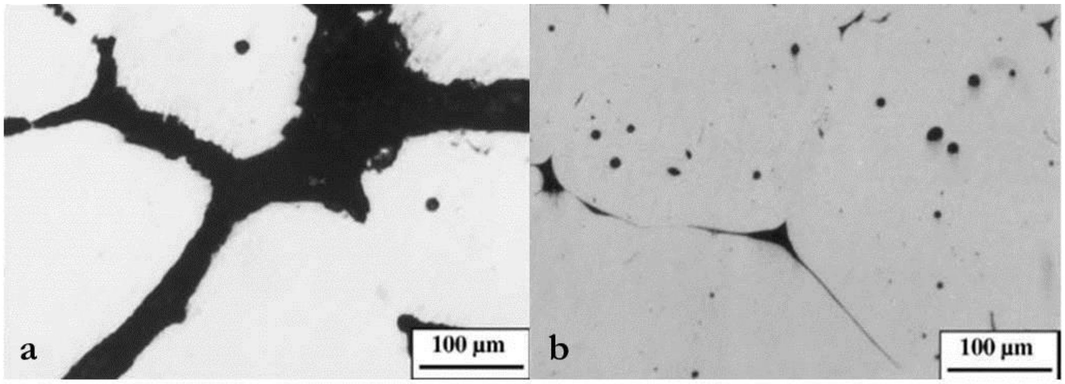

Figure 3.19: Optical micrograph of 7055 alloy ingots after 490 °C/50 h (a) and 455 °C/24 h followed by 490 °C/50 h solution treatment [22].

In the single step 490 °C/50 h solution treatment all the eutectic phases at the grain boundaries melted. Instead, by submitting the part to a prior step at 455 °C/24 h followed by 490 °C /50 h only few patches of molten metal are visible. Furthermore in the latter condition the fraction of residual phases is much lower, indicating more atoms are dispersed in the solid solution, so that better mechanical properties are achievable through precipitation hardening.

An additional drawback of high solutionizing temperatures is related to grain growth and recrystallization. In fact, the elongated grains typical of a rolled microstructure become globular and grow during solution treatment [21, 4], as well as the grains of a CDS microstructure.

Grain growth should be limited since, according to the Hall-Petch relationship below [16], it leads to a decrease in the material yield strength (the stress at which the component starts to plastically deform).

$$\sigma_y = \sigma_0 + \frac{k_y}{\sqrt{d}} \tag{3.1}$$

In the Hall-Petch equation σ_y [MPa] is the yield strength, σ_0 [MPa] is the resistance of the lattice to dislocation motion, k_y [MPa*mm$^{1/2}$] is a strengthening coefficient and *d* [mm] is the average grain size. σ_y, σ_0 and k_y are parameters typical of the material, while *d* obviously depends on the microstructure.

It is therefore clear how small grains generate an increase in the material strength (the high area of grain boundary prevents dislocation motion) and big grains cause a drop in the yield strength instead.

Summarizing, solution treatment temperature and time should be designed to obtain the maximum dissolution of second phases and to improve solute atoms homogenization in the metal matrix. This eventually results in a higher hardness and strength of the component since more atoms are available for the precipitation stage.

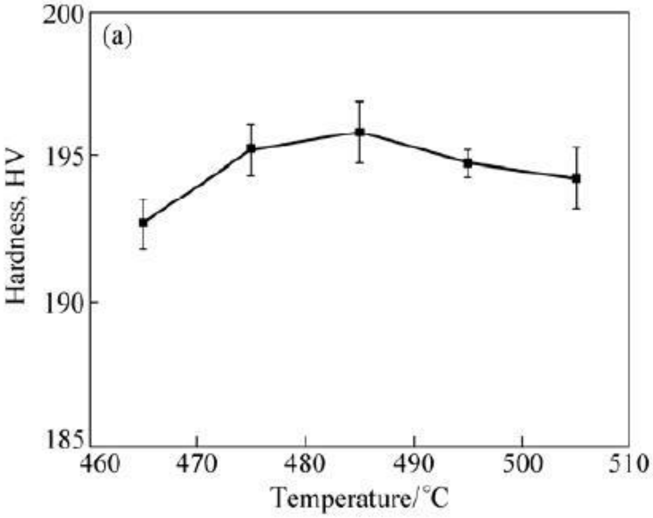

Figure 3.20: Effect of solution treatment temperature on hardness after T6 heat treatment in a AA7050 alloy [4].

Although attention must be paid not to overtake incipient melting temperature, otherwise a lower fraction of eutectic phases is dissolved and porosities form during quenching, thus worsening material hardness and strength.

However, adopting a slow heating rate or stepped solution treatments the incipient melting point can be increased, so that higher mechanical properties are attainable.

Lastly, the grains size and the level of recrystallization should be monitored to avoid lowering the material yield strength.

3.2.3 Quenching

The second step of T4 and T6 heat treatments is quenching. Here the material in the solution treated condition is cooled down to a temperature where second phases should be present inside the microstructure. According to the phase diagram indeed the solubility of atoms inside the Al matrix decreases with decreasing temperature, so that different compounds are formed (Figure 3.8).

Nevertheless the aim of quenching is to prevent the formation of these compounds, called quench induced precipitates, and maintain the solution treated condition at room temperature, in order to obtain a *Super Saturated Solid Solution* (SSSS). In a SSSS the quantity of solute atoms dispersed in the metal matrix is higher than what the solubility limit allows; it is therefore a metastable condition.

The SSSS is a fundamental step for the success of the precipitation hardening process. It is essential indeed to retain as many solute atoms as possible in the metastable condition, so that during the subsequent ageing phase they gather to form small precipitates which hinder dislocation motion. On the other side, a low level of supersaturation leads to a lower amount of ageing precipitates and therefore to a smaller increase in the material strength, meaning the age hardening response of the material is worse.

To obtain a SSSS the formation of quench induced precipitates should be avoided during quenching. When atoms gather into these compounds they are in fact no longer available for the nucleation of ageing precipitates and the supersaturation level of the Al matrix is decreased, and so does the ageing response of the material [5, 14, 4, 10, 31].

The two variables affecting the formation of quench induced precipitates are atoms diffusion rate and supersaturation level. In aluminum alloys the critical temperature range, where nucleation and growth of these precipitates are maximum, is between 450 °C and 200 °C [17]. Above this range the supersaturation level is not high enough, while below it the diffusion rate is too low to cause a fast precipitation of second phases.

A properly designed quenching should then ensure that as little time as possible is spent in this critical region; to do so a proper cooling rate has to be selected.

The exact temperature range of the critical region and therefore the cooling rate to be adopted during quenching depends from the quench sensitivity of each material, whose concept can be better explained by referring to the *Time Temperature Property* (TTP) diagram of the figure below.

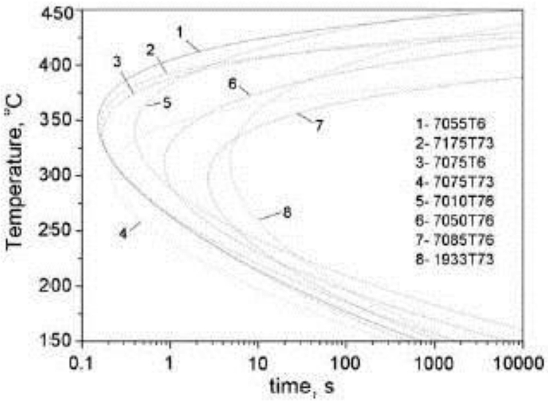

Figure 3.21: TTP diagrams for different Al-Zn-Mg-Cu alloys submitted to different tempers [14].

In a TTP diagram each curve is an iso-property curve, meaning that each point on a single curve is characterized by a strength that is a fixed percentage of the maximum attainable strength of the considered alloy [14]. This percentage is expressed as a function of the time spent at a specific temperature during the quenching stage. In other words the coordinates of each point indicate quenching holding time and holding temperature that lead to the expressed properties. Indeed, as mentioned above, holding a component in a certain temperature range may induce the formation of quench induced precipitates and therefore affects the mechanical properties.

In the particular case of Figure 3.21 each curve represents the 99.5% of the highest properties of the considered alloy. Thus, given a fixed temperature, if a longer time than the one indicated by the curve is spent at that temperature, the obtained mechanical properties will be lower than 99.5%.

From TTP curves two important quenching parameters can be introduced: the critical temperature range and the transformation time at nose temperature. The former is identified by each curve, given a fixed transformation time (e.g. 176 °C – 435 °C for 7055T6 at 100 s of transformation time), while the latter is the maximum time that can be spent at the nose temperature to get at least 99.5% of the highest properties.

Based on these two parameters the quench sensitivity can be defined for each alloy; the bigger the critical temperature range or the smaller the transformation time at the nose temperature the more quench sensitive an alloy is.

Referring to the above figure, Alloy 1 with a nose holding time shorter than 0.2 s is therefore more quench sensitive than Alloy 8, whose nose holding time is around 7 s; then a faster cooling rate should be adopted to quench Alloy 1 with respect to Alloy 8.

To better understand how isothermal holding during quenching influences sample mechanical properties such as the hardness, the image below is presented.

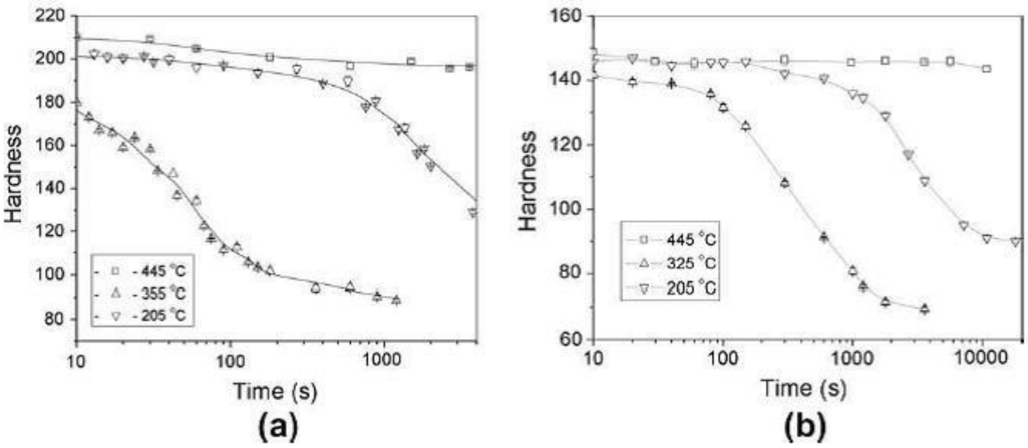

Figure 3.22: Quenching isothermal holding hardness curves of 7055T6 (a) and 1933T73 (b) [14].

The analyzed alloys are respectively Alloy 1 and Alloy 8 of Figure 3.21.

In both cases it is possible to evaluate how holding time is not an issue for those temperatures which lie outside the critical temperature range. The component could be held at 445 °C or 205 °C for periods as long as 200 s before noticing a decrease in its microhardness.

For the more critical nose temperatures instead the microhardness starts to decrease at shorter times; at these temperatures the effect of quench sensitivity stands out. For the more quench sensitive Alloy 1 the hardness values always decrease with increasing holding time, whereas for Alloy 8 their decrease begins to be appreciable after 80 s only.

As Figure 3.21 indicates, quench sensitivity is a particular issue in Al-Zn-Mg-Cu alloys [5, 14, 4]. Within this series other factors such as the total amount of solute atoms, the Zn/Mg ratio, the presence of Cr or Zr dispersoids and tempers have an impact on quench sensitivity [14].

As previously mentioned, the level of supersaturation influences precipitation kinetics during quenching, therefore the higher the amount of solute atoms in Al matrix the higher the chance they gather into quench induced precipitates.

With regards to Zn/Mg ratio it was found instead how a high level of Zn compared to Mg reduces the quench sensitivity. This result is likely to be a consequence of the importance of Mg in the formation of precipitates in 7xxx alloys [32], therefore the lower its relative amount the lower the tendency to form precipitates.

To understand the influence of Cr and Zr it should be remembered that quench induced precipitates usually nucleate at the grain boundaries or on dispersoids (Figure 3.23 (b)) and that incoherent interfaces attract atoms more easily than coherent interfaces [14, 33, 34]. Then, since Zr dispersoids are finer and coherent with the matrix and Cr dispersoids are coarse and incoherent, the presence of Zr is preferable to Cr from a quench sensitivity perspective [14].

Lastly, the effect of temper on ageing has been verified, but the mechanisms behind the relationship are not clear yet, even though it is likely the implemented cooling rate affects the ageing dynamics and so the mechanical properties [14].

As said before, if the cooling rate is not properly selected and the component is held for long times in the critical temperature range quench induced precipitates will form in the microstructure. These can be $MgZn_2$ (η), $MgCuAl_2$ or the T phase $Al_3Zn_3Mg_{3,}$ $(AlZn)_{49}Mg_{32}$ [10, 34]; this last compound nucleates only at high concentration of Mg, namely at high Mg/Zn ratios [35].

Figure 3.23 demonstrates how with high cooling rates (water quenching) quench induced precipitates are not present in the material microstructure and the bigger particles are $AlZr_3$ dispersoids. With air cooling instead η nucleates both at the grain boundaries and on dispersoids, while S and T components are visible in the material substructure [10].

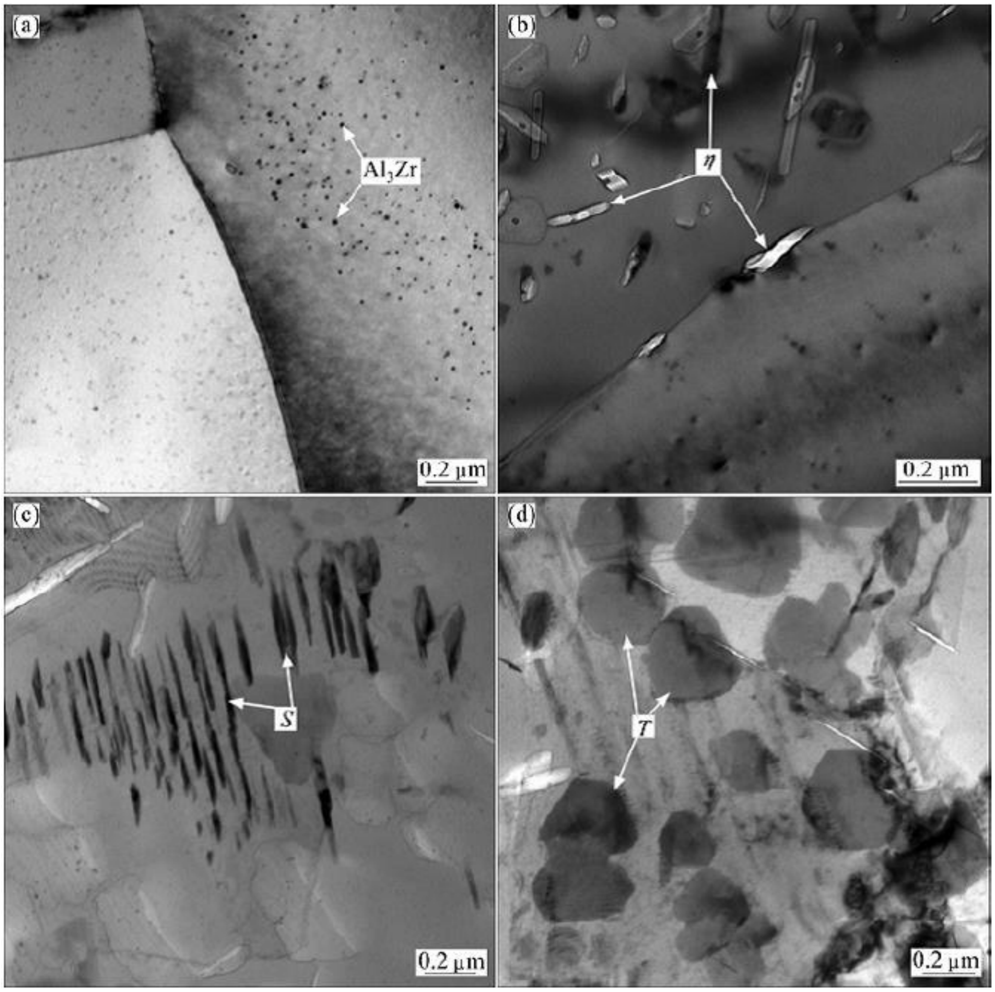

Figure 3.23: TEM micrograph of Al-8.02Zn-1.75Mg-1.99Cu after solution treatment and water (a) or air (b, c, d) quenching [10].

Besides the already mentioned effect on the reduction of the supersaturation level, the formation of precipitates during quenching drastically decreases the number of vacancies, which are an essential element for the diffusion of solute atoms during ageing.

Vacancies are point defects of the crystal structure consisting of positions in the material lattice where atoms are not present. Their formation is a function of different factors and their number is expressed by the formula below [20].

$$N_v = Ne^{-\frac{Q_v}{kT}} \tag{3.2}$$

N_V is the total number of vacancies, N is the total number of atomic sites, Q_V is the energy required for the formation of a single vacancy, k is the Boltzmann's constant ($1.38 * 10^{-23} \frac{J}{atom\ k}$) and T is the temperature expressed in Kelvin.

During solution treatment the high temperatures reached create vacancies (the higher T the higher N_V). As aforementioned, vacancies are a fundamental requirement for atoms motion; these can indeed diffuse inside the lattice only if there are empty sites in their surroundings [20]. Though, when atoms jump from one vacancy to the next one, the vacancy they leave behind is destroyed and therefore can no longer be used for diffusion. It is thus clear how the gathering of atoms in quench induced precipitates reduces solute mobility during the last stage of the heat treatment and therefore the ageing response of the material [11].

The last drawback of quenching precipitation is related to the evolution of the material microstructure during ageing. The presence of already formed coarse and incoherent precipitates indeed deeply affects solute atoms behavior; while they would gather into small and dense precipitates in a properly quenched component, with quench induced precipitates they are attracted by the incoherent interfaces of these [10, 36]. Again this occurs because the energy required to join an already nucleated and big precipitate is lower than forming a new one.

The attraction results thus in the formation of areas where precipitates are absent, known as *precipitates free zones* (PFZ). In these zones dislocations are free to move without any obstacle, so that the material strength is further decreased with respect to a properly quenched part [10, 36].

PFZ are located in the surroundings of quench induced precipitates and the coarser the precipitates the wider their extension. Therefore in a slow cooled sample, where quenching precipitates grow bigger and in a higher number, the area fraction of PFZ is higher than in a fast cooled one [10, 36].

The difference between PFZ for water and air quenched samples is illustrated in the image below.

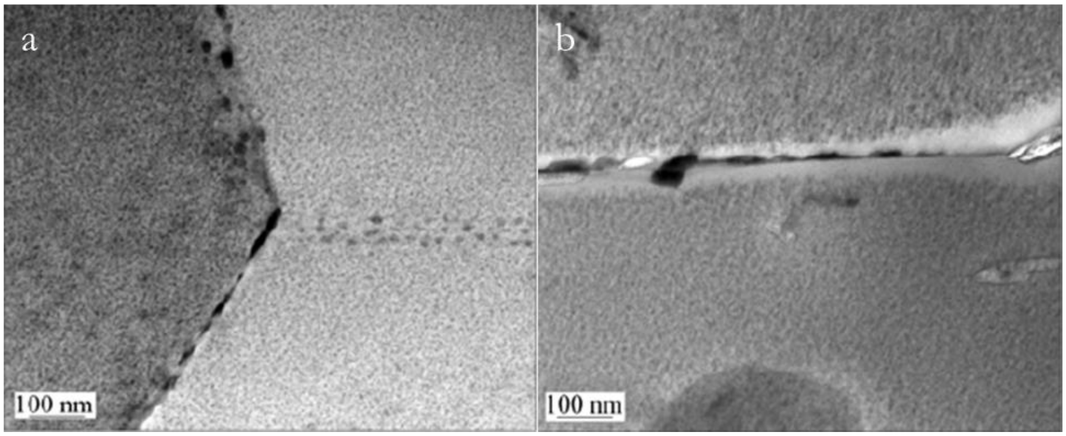

Figure 3.24: TEM micrographs of Al-Zn-Mg-Cu alloy after T6 heat treatment for water (a) and air (b) quenched samples [10].

In water quenched components the cooling rate is higher than in air quenched ones, therefore in the former case η quench induced precipitates (black spots), visible at the grain boundaries, are smaller and more continuous than in the latter condition. For this reason in the air cooled part wider PFZ (light grey areas around η) evolve during ageing [10].

Having described the main drawbacks related to a slow quenching, the overall influence of water and air cooling on the material microhardness during ageing is summarized by Figure 3.25.

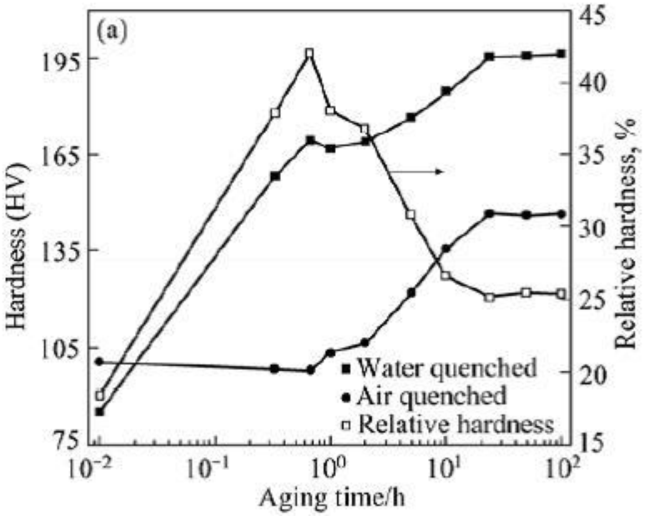

Figure 3.25: Microhardness of Al-8.02Zn-1.75Mg-1.99Cu aged at 120 °C as a function of ageing time and cooling rate [10].

The trend highlights what stated above. Air quenched samples are characterized by lower values of microhardness than those obtained in water quenched ones. The difference reaches a peak higher than 40% for an ageing time shorter than 10 h, before decreasing to a constant value of 25 % for longer times of artificial ageing.

Nevertheless it should be mentioned that a too high cooling rate should be avoided. During cooling indeed a compressive state is introduced in the surface of the component while the interior is submitted to tensile stresses. A high temperature gradient, as results from a very high cooling rate, would increase these residual stresses, which in turn may lead to an early failure of the component [31]; the presence of residual stresses in fact decreases the load a part can withstand before the occurrence of deformation.

Summarizing, during quenching the material is cooled from the solution treatment temperature to obtain a metastable SSSS of solute atoms inside the Al matrix. A high supersaturation level is indeed useful to enhance the mechanical properties during the ageing stage.

To prevent the loss of solute atoms available for the nucleation of ageing precipitates, the formation of quench induced precipitates has to be avoided. It is therefore necessary to select a cooling rate which shortens the time spent in the critical temperature region, where the precipitation rate is higher. Water quenching is usually preferred to air quenching to attain these characteristics.

On the other side though a too fast cooling rate should be avoided as well since it may introduce in the component residual stresses which could result into an early failure.

3.2.4 Ageing

Ageing is the last stage of precipitation hardening heat treatments. As already stated, the difference between the two heat treatments carried out in this project lies in the temperature at which the ageing step is performed. If samples are held at room temperature we are dealing with natural ageing and T4 treatment. Instead when components are heated up to a temperature below the solvus line artificial ageing takes place and the heat treatment is addressed as T6.

It has already been explained how after quenching the microstructure is in a metastable condition, since the concentration of solute atoms in the Al matrix is higher than what the solubility limit allows. During ageing therefore solute atoms gather into small and dense precipitates which, hindering dislocations motion, increase material hardness and strength.

This section is then focused on the main precipitation sequences occurring during both natural and artificial ageing in Al-Zn-Mg-Cu alloys and on the evolution of the different phases.

The driving force leading to the formation of precipitates is once again the need to minimize the energy of the system in the quenched condition. According to what was previously mentioned, a high supersaturation level results in a higher density of precipitates. This, from the energy point of view, means that a high concentration of solute generates an increase in the system energy which therefore, to minimize it in the shortest time, forms a high number of precipitates. To understand this concept it should be remembered that during ageing the part is in the region of the phase diagram where second phases should be present (Figure 3.8), thus destroying the SSSS and nucleating precipitates lowers the overall energy.

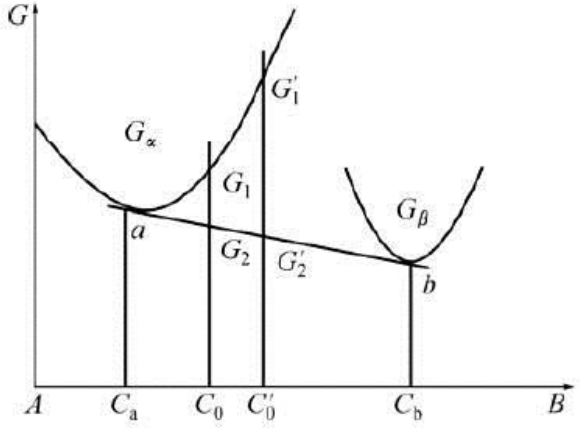

Figure 3.26: Free energy change of precipitation under different supersaturated conditions [4].

Figure 3.26 illustrates the idea. Given that G_α and G_β represents respectively the Gibbs free energy of the Al matrix α and of the second phase β, by increasing the concentration of solute B from C_0 to C'_0, the matrix energy increases as well from G_1 to G'_1. Then, drawing a straight line between the minimum of the two curves and finding the points on this line that correspond to the two different concentrations (G_2 and G'_2), the energy difference G_1 - G_2 or G'_1- G'_2 is defined as the precipitation driving force. As it was expected, the driving force is higher with a higher concentration of B since the energy of the matrix is higher as well. In turn, the precipitation driving force is inversely proportional to the critical radius of nucleation, that is to say, with a high driving force less atoms are required for nucleation. In the end, a small nucleation radius means a shorter time is needed for the formation of a phase, so that a high nucleation rate is obtained and the density of precipitates is increased [4].

After this whole explanation it should be clearer why quenching design is usually addressed to get the highest possible level of supersaturation; there is indeed a direct relationship between solute concentration and density of precipitates.

The main precipitation sequence taking place in Al-Zn-Mg-Cu alloys is the one that follows [33, 35, 36, 37, 38].

$$\text{SSSS} \rightarrow \text{VRC} \rightarrow \text{GPI and GPII} \rightarrow \eta' \rightarrow \eta(\text{MgZn}_2) \qquad (3.3)$$

From the SSSS, in presence of *Vacancy Rich Clusters* (VRC), namely patches of the lattice where the density of vacancies is particularly high, Guinier Preston zones of type I (GPI) and type II (GPII) evolve. These are regions of the crystal structure where the concentration of solute atoms is higher. They are the precursors to the metastable η' and stable η.

It should be highlighted that η does not always generate according to the shown sequence. Ageing precipitation is in fact an extremely dynamic process and many factors influence the microstructure evolution; then the above sequence is not strictly followed.

What SSSS and vacancies are has already been explained earlier in this chapter, therefore features and formation mechanism of GP zones, η' and η are going to be analyzed.

Before starting, it is essential to remind here that every concept reported in the following is related to conventionally cast 7xxx aluminum. The first precipitation sequence analysis of these alloys, cast with the CDS technique, is indeed the aim of this project. In addition all the reported information about artificial ageing regard samples which have been heated up right after quenching, so that only a negligible time was spent at room temperature.

3.2.4.1 Natural ageing

In the presence of available vacancies solute atoms dissolved in the Al matrix start to diffuse to form precipitates as soon as quenching is completed. During natural ageing the sample is held at room temperature, then the diffusion rate is low and long times are required for the formation of second phases. Although, because of the low energy available for atoms diffusion, the precipitation sequence stops at GPI [37], which are therefore responsible of material hardening during natural ageing.

Unfortunately, due to the best strength enhancement attainable with T6 treatments, an extensive study of GPI zones formation sequence during natural ageing has not been undertaken yet.

The main information are reported by Sha and Cerezo who assert that, after 1.5 h of natural ageing, small clusters of solute that eventually evolve into GPI are present in the microstructure. According to studies performed on the composition of GPI zones in natural ageing, after 90 min these clusters are characterized by a Zn/Mg equal to 0.85 that, together with analyses on GPI activation energy, suggests Mg diffusion is the crucial factor in GPI nucleation [32].

From artificial ageing results it is known that the Zn/Mg ratio of big GPI is equal to 1. This induces to believe in natural ageing the early stages of precipitation are characterized by the presence of small Mg rich clusters which, evolving into GPI zones and increasing in size, attract Zn atoms until Zn/Mg is 1 [32]. When this condition is reached the precipitation sequence ends and the microstructure is stable.

It was found that early GPI zones show a composition of Cu close to 12 at. %. This value decreases in bigger GPI to 5 at. %, meaning Cu is involved only in the early stages of GPI formation. The presence of Cu inside small GPI is essential, since it promotes a higher hardening response of the material in the first precipitation stages [32].

As far as what concerns the morphology of stable GPI zones it is widely accepted they are fully coherent with the Al matrix and feature a spherical shape of alternate Zn and Mg layers [37, 38].

Lastly GPI zones usually form from room temperature up to 140 °C and do not necessarily need the presence of VRC to nucleate [32, 35, 37, 38].

Summarizing, during natural ageing the only precipitate featuring in the microstructure are GPI zones, which in the early stages of their formation are small Mg rich clusters. In the coherent and stable condition they are instead characterized by a spherical shape of alternate Zn and Mg layers (Zn/Mg = 1). Moreover the presence of Cu may enhance the hardening in the early stages of precipitation.

3.2.4.2 Artificial ageing

During artificial ageing the sample is held at higher temperatures with respect to natural ageing, therefore more energy is available for atoms diffusion.

As in natural ageing the first precipitate forming from the SSSS are GPI zones; nevertheless their nucleation occurs in a much lower time. If at room temperature GPI takes almost one day to reach their stable condition, between 121 °C and 130 °C instead they just need 60 min, while their presence is already reported after 15 min only [32, 35]. These observations were obtained through TEM images and *Selected Area Diffraction* (SAD), a special technique that, exploiting the small wave lengths of electrons emitted in a TEM, provides a pattern of the compounds present in the matrix. Normally electrons pass between atomic sizes and hit the microscope lens, so that the obtained image is bright. In those spots where atoms or other particles are present, electrons are diffracted and the image presents black spots. According to the different sizes of these spots it is then possible to realize what types of compound are present in the microstructure [39].

In Figure 3.27 GPI zones after 15 min of holding time at 130 °C are visible. From their distribution and density it is deduced that they originate from homogeneous nucleation throughout the Al matrix [32].

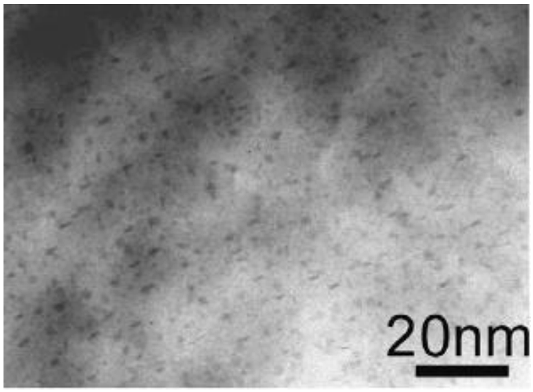

Figure 3.27: TEM image of a 7050 alloy aged 15 min at 130 °C [35].

Through 3D *Atom Probe* (3DAP) analysis a 3D reconstruction of the precipitates, together with their composition analysis, can be performed. In this technique a specific microscope exploits an electric field to cause the evaporation of atoms from the sample being studied. The atoms leaving the samples are then detected by a spectrometer and based on the collected data the entire microstructure can be reconstructed in a 3D shape [40].

Data about the Zn/Mg ratio of GPI zones are obtained with this technique. It was found that after 30 min at 121 °C the Zn/Mg ratio equals 0.91, indicating that the stable condition has not been reached yet since Mg is still the dominant element (stable condition at Zn/Mg = 1) [32]. Moreover this datum demonstrates that GPI zones evolve faster in T6 than in T4; after only 30 min at 121 °C indeed their Zn/Mg ratio is higher than after 90 min at RT.

As aforementioned, after 60 min of artificial ageing GPI are stable, therefore Zn/Mg ratio reaches 1. While in natural ageing this condition is the end of the precipitation sequence, in artificial ageing GPI can still evolve into η'. In this case more Zn atoms would be attracted and, starting from their spherical shape, GPI would grow in one direction and would be characterized by an elongated shape and a Zn/Mg ratio of 1.2. Eventually the growth would begin in another direction parallel to the first one and η' would be formed. Alternatively GPI can grow in size and become coarse blocky clusters with Zn/Mg of 1 that would feature in the microstructure even after 24h of ageing [32].

The effect of Cu reported for natural ageing holds in artificial ageing as well.

If GPI begin to form from RT, GPII instead nucleate only above 70 °C, so that they evolve during artificial ageing only, directly from the SSSS. Differently from GPI, VRC have to be present for their formation, since GPII were found only in samples quenched from solution treatment temperatures higher than 450 °C, meaning the amount of vacancies in the matrix is an influential factor [35, 37].

Specific studies on the formation sequence of GPII were not found. The only information in the literature is that they are characterized by Zn rich layers organized into a plate like morphology [32, 35, 37]. No particular reference about their coexistence with GPI zones was found.

It should be mentioned that, despite the analyzed conditions were those reported for the nucleation of GPII, both Sha and Cerezo and Wu et al. did not find any evidence of GPII zones in their studies on artificial ageing of 7xxx series alloys [32, 38]. Therefore no explanation of the evolution process of GPII into η' was provided.

η' are metastable Zn rich plate like precipitates that are semi coherent with the Al matrix [35, 37]. It was explained before how these compounds evolve from GPI zones; although they may nucleate directly from the SSSS attracting solute atoms of dissolving GPI. It should be pointed out indeed that small GPI may grow into stable blocky clusters, evolve into η' or alternatively dissolve [38].

SAD patterns of a 7050 alloy aged at 121 °C reveals how η' begin to form after 60 min and keep increasing in size up to 24h, where they feature in the material microstructure with big and stable GPI. According to DAP analysis newly formed η' are characterized by a Zn/Mg ratio of 1.07, while after 24 h of ageing it increases to 1.26. This datum, with those relative to the Zn/Mg ratio of GPI, shows that stable conditions are characterized by a high Zn/Mg, meaning that Zn plays an important role in the stability of the precipitates [32].

An image of a 7050 alloy aged at 121 °C for 24h is reported below; the present precipitates are η' which appear as big disks or as rods. This is linked to their different orientation in the material microstructure (viewed form the top or from the side); they are indeed all characterized by the same shape. It is interesting to notice the size difference with GPI illustrated in Figure 3.27; these are usually in the range of 3 nm, while η' are usually 7 nm long [38].

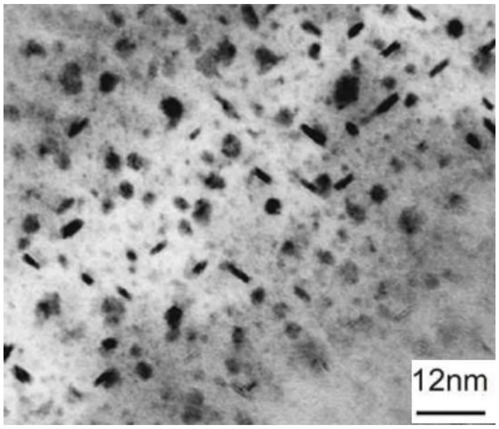

Figure 3.28: TEM image of a 7050 aluminum alloy aged at 121 °C for 24h [32].

In SAD patterns of samples aged at 121 °C for 24h very small diffraction spots indicate that η begins to form. η ($MgZn_2$) is a stable and fully incoherent precipitate with a plate like morphology and a size of 15 nm that evolves from η' or directly from the SSSS [32, 37, 38].

Overall η can have nine different orientations in the crystal structure. The most frequent ones are η_1, η_2 and η_4, to which different evolution paths are associated; η_1 nucleates directly from the SSSS, η_4 grows on defects such as grain boundaries and dislocations while η_2 evolves from η'. This transformation occurs gradually and consists in η' attracting Zn atoms and slowly changing their shape [38].

Briefly summarizing the precipitation sequence taking place during artificial ageing, in the early stages small GPI zones with a Zn/Mg of 0.91 nucleate. These can grow in size reaching a stable condition with Zn/Mg of 1, grow and evolve into η' or dissolve.

GPII zones described in the literature instead were not observed during experimental analysis.

The metastable and semi coherent precipitate η' begins to form after 60 min of ageing at 121 °C and stabilizes after 24h with a Zn/Mg of 1.26. It can evolve from GPI or directly from the SSSS. At longer ageing times Zn atoms join η' which further transforms into the stable and incoherent $MgZn_2$ η. This precipitate can alternatively nucleate on lattice defects or from the SSSS.

The evolution of cluster density and average cluster size as a function of ageing time during the precipitation sequence can be observed in the following graphs.

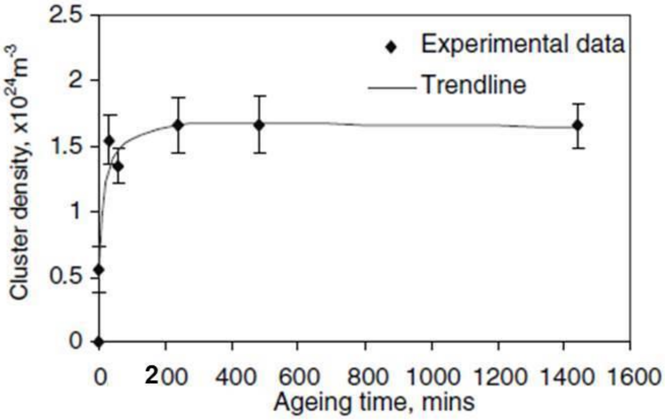

Figure 3.29: Average cluster density during ageing of a 7050 alloy up to 24h at 121 °C [32].

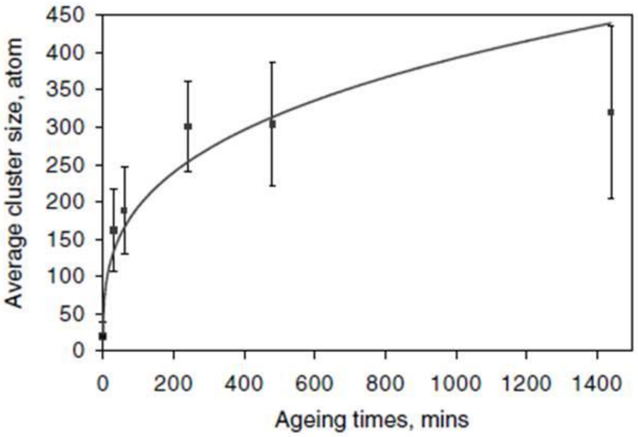

Figure 3.30: Average cluster size during ageing of a 7050 alloy up to 24h at 121 °C [32].

In the first 30 min of ageing the rate of increase in cluster density is the highest. This is linked to the high nucleation rate of GPI zones, which reach their maximum density after 30 min. The stable value of cluster density is then gradually approached with the formation of η', that is complete after 240 min of ageing; the flat trend in Figure 3.29 indicates that after 240 min precipitates nucleation is no longer taking place in the microstructure. Although, at longer times, the present η' increase in their size, as clearly shown in Figure 3.30 [32], whose trend is perfectly explained by the afore-described precipitation sequence.

For a better understanding of the variety of the precipitation sequence the average cluster size evolution should be analyzed. In the first stages, up to 240 min, where nucleation ends, the increase is clear and the size variability is almost constant. This is because at this time the only precipitates present are small GPI and big GPI, characterized by a small size difference, plus newly evolved η', slightly bigger than GPI.

When ageing continues instead the experimental average cluster size is still constant, while the high variability of the data leads to a continuous increase in the trend line cluster size. This variability increase provides a direct hint on the heterogeneity of the precipitates present in the microstructure; After 24h of ageing the material is characterized by big and coarse GPI, big and stable η', elongated η' evolving into η and some η directly nucleating form the SSSS. The high variability therefore reflects the width of the precipitates size range.

Lastly the effect of the different precipitates on the material microhardness and therefore strength is illustrated below.

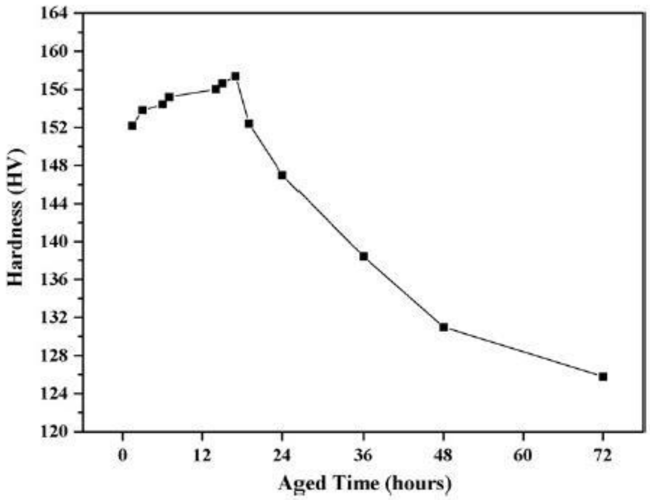

Figure 3.31: Microhardness evolution of a Al-Zn-Mg-Sc-Zr alloy aged at 140 °C [38].

It must be pointed out that this curve is only used as an example since the alloys analyzed in this project do not contain Sc or Zr.

The curve reaches a peak of 158 HV after almost 18h of ageing, when only η' and GPI are present in the microstructure. After that, when η begins to appear as well, the strength of the material decreases. This indicates that GPI and η' are the hardening precipitates, while η growth should be avoided since it causes a drop in the material strength [38].

To understand this behaviour, the strengthening mechanism explained in Figure 3.7 has to be referred to. In the first 18h of ageing the precipitates present inside the matrix (GPI and η') are characterized by a relatively small radius, therefore they are sheared by dislocations, so that the material strength increases. η precipitates instead are beyond the threshold radius and are bypassed by dislocations, leading to lower properties.

It is thus usually desirable to stop the ageing treatment at the peak strength before η nucleates and the strength decreases, in which case ageing would be addressed as overageing. To avoid overaged conditions the selection of ageing time is therefore crucial. Nonetheless the main parameter to be monitored is the ageing temperature.

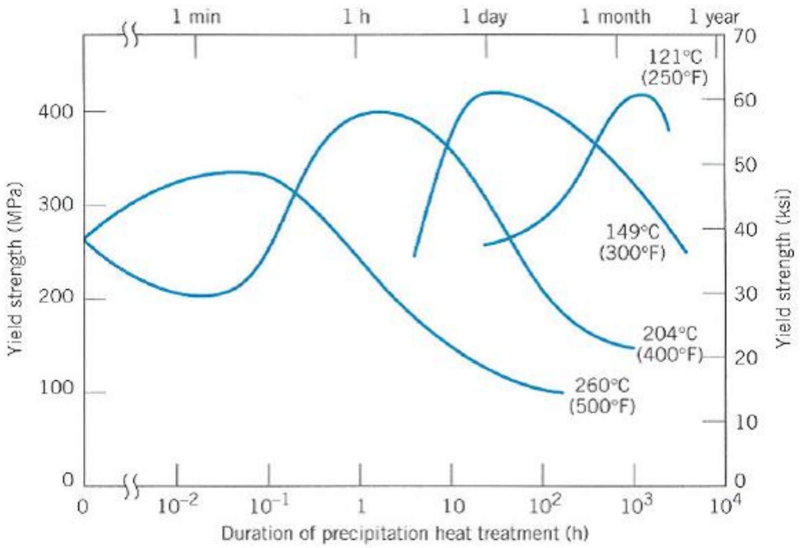

Figure 3.32: Artificial ageing temperature and time effect on aluminum alloys yield strength [15].

Figure 3.32 indicates how increasing ageing temperature the peak strength is reached in a shorter time since the diffusion rate of atoms increases, but the obtained value is lower than what results from lower temperatures ageing.

It is thus now clearer how ageing temperature and time should be appropriately chosen in order to obtain the desired mechanical properties.

4. Experimental

In this chapter the studied alloy compositions and the procedure from which samples were obtained are going to be presented, together with the main concepts behind macrohardness and microhardness. A detailed sequence of the project outline and of the measurement schedule is going to be reported as well.

4.1 Material and samples

As already mentioned in the previous chapters, the analyzed alloys are CDS cast 7xxx *wrought aluminum alloys*. More precisely, three different compositions (wt%) were tested.

- Al-3.6Zn-1.8Mg
- Al-6.5Zn-2Mg-1.5Cu
- Al-6Zn-2.2Mg-2.3Cu

These were chosen to evaluate the influence of different Cu contents and Zn/Mg ratios on the precipitation sequence; it has already been presented in the previous chapter how these two parameters strongly affect the microstructure evolution during ageing.

The Cu content is respectively of 0 wt%, 1.5 wt% and 2.3 wt%, while the Zn/Mg ratio is equal to 2, 3.25 and 2.72. Obviously in the alloy without Cu, not all the precipitates previously illustrated can nucleate.

The alloys were obtained through the CDS technique described in section 3.1[4] and reported by Ghiaasiaan et al. [9], and cast into the shapes of Figure 3.1. The cast parts were characterized by two tensile specimens on the sides; from the gauge lengths of these tensile bars the experimental samples were sectioned with a saw.

For a better control of the flatness, essential to perform accurate hardness measures, the samples were then mounted and their height adjusted on a lathe (Figure 4.1).

---

[4] The composition of the precursor alloys cannot be reported here for secrecy reasons.

Figure 4.1: Mounted and flattened samples.

The surface preparation consisted in grinding those samples on which the macrohardness test would have been performed and in polishing those for the microhardness.

The final samples, once removed from the mount, are cylinders with a height of 10 mm and a diameter of 12.5 mm.

Figure 4.2: Final sample.

4.2 Hardness measurements

The hardness of a material is a measure of the lattice resistance to the penetration of a specific indenter. A certain load is applied to the indenter and, after a varying holding time, removed, so that the trace of the indentation left on the sample surface indicates how hard the evaluated sample is; the higher the hardness the smaller the penetration.

During the test the material undergoes a surface deformation and then dislocations movement is implied. Therefore, since the formation of precipitates hinders the motion of dislocations which, in turn, results into lower deformation and penetration, the measured hardness values provide a direct idea on the amount and type of precipitates present in the microstructure. For example GPI zones, being small and coherent with the matrix, do not require a lot of energy to be overcome, so that the hardness during natural ageing is low. On the other hand during artificial ageing, when η' nucleates, dislocation motion is hindered and the material hardness increases.

As it was probably understood, the relationship between hardness and precipitates is the same as that between strength and precipitates illustrated in section 3.2; therefore a direct relationship exists between hardness and strength, both YS and UTS. Since the analysis of the specific values of hardness and strength is not the scope of this project, it will be just mentioned here their relationship is linear and the angular coefficient is a function of parameters such as the different material analyzed, the material strength, the processes components have been submitted to and the adopted hardness tests [41].

To predict the precipitation sequence both macrohardness and microhardness were evaluated. The difference between them lies in the size of the indentation; the former, with a bigger indenter, tests the surface hardness on a macro scale (mm), while the latter measures the hardness on a micro scale (μm). For this reason the microstructure features affecting the obtained values of macrohardness are different from those affecting the microhardness; in the first the indentation covers a variety of compounds, while in the second the indenter usually hits only the metal matrix. For a better understanding, with reference to Figure 3.11 the whole shown field would lie underneath a macrohardness indentation, whereas only a fraction of the dark grey areas of each grain would be covered by a microhardness indentation. Therefore what affects microhardness values are metal matrix and ageing precipitates, while macrohardness values are additionally influenced by eutectic phases and grain boundaries.

4.2.1 Macrohardness

Different tests and scales can be adopted for macrohardness measurements; they differ for the type of indenter and applied load. Usually their selection depends from the material being analyzed. Aluminum alloys are generally tested with the Rockwell B scale; although, since the corresponding major load was too high for the hardness observed in the early stages of ageing, a Rockwell F scale was implemented in this project.

In the Rockwell F, whose unit of measurement is *Hardness Rockwell F* (HRF), the indenter is a steel ball with a diameter of $\frac{1}{16}$ in. Referring to the image below, from the left to the right, a minor load of 10 kg is applied to the indenter and the penetration depth e_0 is registered. Then the load is increased of 60 kg (major load in Rockwell F) and the indenter stops at a depth e_1. Finally the major load is removed and the steel ball penetration e_2 is measured again [42].

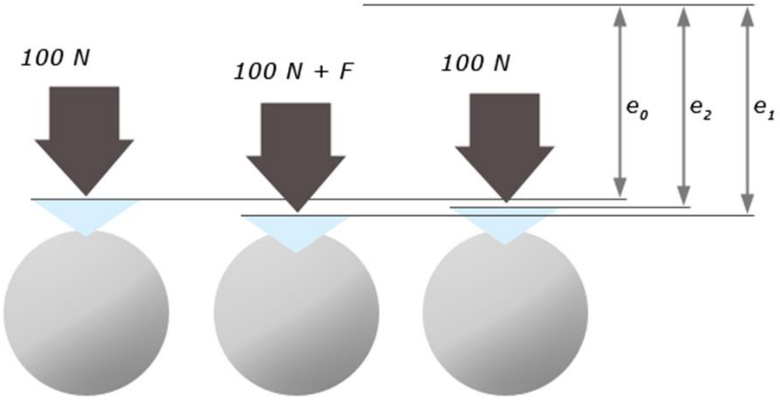

Figure 4.3: Indentation depth and load application steps in Rockwell F [43].

From the recorded penetration depths and the relationship below, the macrohardness value is then obtained [42].

$$HRF = 130 - 500(e_2 - e_0) \tag{4.1}$$

As required for an accurate measurement, a minimum distance of 2.5 indenter diameters was left between the center of each indentation and the edge of the specimen, while a distance of at least 3 indenter diameters was left between the centers of two indentations [42].
All the tests were carried out with the Mitutoyo HR 400 Rockwell hardness testing machine of the figure below, whose output was the obtained HRF.

Figure 4.4: Mitutoyo HR 400 Rockwell hardness testing machine used during the project.

4.2.2 Microhardness

Differently from the macrohardness, only two different scales are available for the microhardness; the Vickers test was chosen to carry out the measurements.

For this scale the indenter is characterized by a pyramidal shape, with a square base, and both the applied load and the holding time are selected by the operator; in this project a load of 25 g and a holding time of 10 s were chosen.

A typical trace of a Vickers indentation on the material surface is shown below, where the square base pyramidal indenter can be recognized.

Figure 4.5: Optical micrograph of a Vickers indentation [44].

By knowing the length of the two diagonals and the applied load, the hardness value can be calculated through the equation [45]:

$$HV = 1854 * \frac{F}{l^2} \tag{4.2}$$

Where HV stands for *Hardness Vickers*, F is the applied load [g] and l is the arithmetic mean of the two diagonals [µm].

As previously mentioned, since the microhardness test aims at evaluating the influence of metal matrix and ageing precipitates, all the indentations were performed inside the grains and away from eutectic phases and grain boundaries. Besides, as for the macrohardness, attention was paid to leave enough space between two indentations (at least 5 times the diagonal length).

The measurements were performed with the Buehler Micromet II microhardness testing machine.

Figure 4.6: Buehler Micromet II microhardness testing machine used during the project.

4.3 Project outline

The first step of the project consisted in evaluating the macrohardness evolution of the three alloy compositions during natural ageing, in other words during the T4 heat treatment. Based on the results, the alloys with the higher and lower level of hardness were selected and the following of the analysis was carried out only on these two.

The remaining alloys were then submitted again to the T4 treatment and their microhardness variation was measured.

Looking at the microhardness evolution during natural ageing a precipitation theory was formulated; according to this theory the microhardness curve was divided into different regions corresponding to different time intervals. Based on these regions artificial ageing and the T6 heat treatment were designed; more precisely the incubation period, the time spent at room temperature between quenching and the beginning of artificial ageing, was selected.

Finally both macrohardness and microhardness evolution were observed during all the different artificial ageing conditions and, according to the obtained results, the formulated precipitation theory was verified and further developed.

4.3.1 Heat treatments

As previously mentioned, a precipitation hardening heat treatment is made of three different steps: solution treatment, quenching and ageing. Depending on the temperature at which the ageing phase is carried out the heat treatment is labeled as T4 or T6. In the former the sample rests at room temperature and natural ageing takes place, while in the latter the sample is heated up below its solvus line and the process is called artificial ageing.

Solution treatments were carried out in a Lindberg 51442 model furnace, having a measured temperature variation of ± 2 °C, while artificial ageing was performed in a Furnatrol II furnace characterized by a variation of ± 3 °C. The temperature during the experiments was monitored with a K-type thermocouple embedded in a sample.

In this section the parameters adopted in the three steps are reported.

Based on the incipient melting temperature range reported in the literature for 7050 alloys, between 482 °C and 486 °C, and considering a safe margin of 5 °C / 9 °C, the selected solution treatment temperature was 477 °C; this temperature was adopted for all the analyzed alloys, regardless of their incipient melting temperatures. Therefore, while it is optimal for Al-6Zn-2.2Mg-2.3Cu, whose composition is in the range of 7050 alloys, it is probably lower than the ideal for the other two compositions. In fact, being the S phase the main responsible for incipient melting, and since the amount of S phase in the microstructure is higher with higher Cu content, the alloys containing a smaller or null amount of Cu, with respect to 7050, are characterized by a higher incipient melting temperature. Although a DSC analysis was not performed on them, thus the solution treatment temperature was kept constant since incipient melting wouldn't have occurred.

The samples were solution treated for 25 h, including the time to heat up the furnace. In order to address the industrial feasibility of such a treatment, it should be mentioned again that the scope of this project is not to design an optimal heat treatment, but to understand the precipitation mechanisms occurring during T4 and T6 heat treatments. Therefore 25 h of solution treatment were chosen to prevent the influence of a too short solutionizing time on the microstructure evolution, by ensuring that as much of the eutectic phase as possible was dissolved in the metal matrix.

At the end of the first stage, to avoid the formation of quench induced precipitates and the related drop in age hardening response, the samples were quenched in water at room temperature; followed by the ageing.

As far as the T4 treatment is concerned, samples were left at room temperature for 14 days or more, depending on hardness variation. During this time both macrohardness and microhardness were measured according to the schedules reported in the next section. At the end of the treatment a complete time evolution of the hardness during natural ageing was obtained.

Instead, the T6 treatment samples were kept at 120 °C for 96 h and the hardness was measured at the steps illustrated in the next section. Differently from natural ageing, several conditions of artificial ageing were analyzed. Indeed, according to the formulated precipitation theory, different incubation periods were adopted before artificial ageing was started; this means that samples went through a stage of natural ageing before entering the furnace. The aim of this procedure was to analyze the influence of the natural ageing stages on the artificial ageing behaviour of the material.

For a better understanding of the concept the result of a similar work carried out on A356.2 Al alloy is presented below, where No AA is the microhardness evolution curve for natural ageing, while those labeled with # IP are artificial ageing curves. The number before IP indicates instead the hours of incubation period.

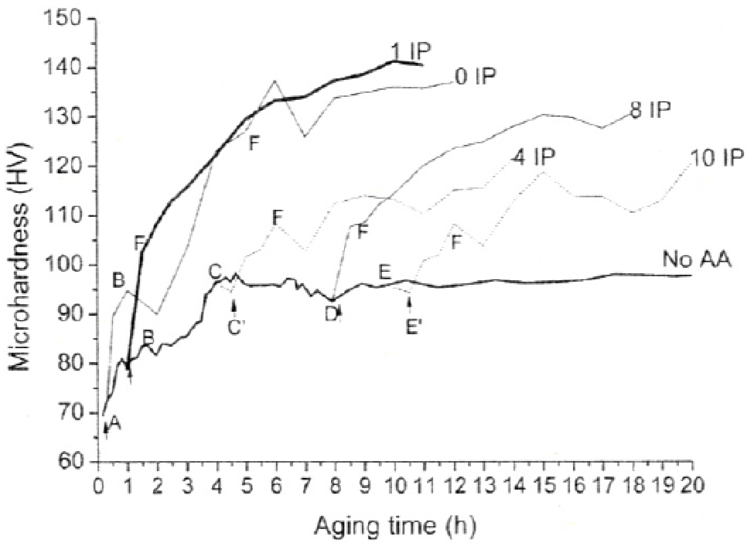

Figure 4.7: Microhardness values as a function of natural (No AA) and artificial ageing time, after 0 (0IP), 1 (1IP), 4 (4IP), 8 (8IP) and 10 (10IP) hours of natural ageing [11].

From the values of microhardness reached it is possible to realize how beginning the artificial ageing after different holding times at room temperature deeply affects precipitates evolution. In fact, even though artificial ageing parameters were constant, the hardness obtained after 12 h of treatment varies according to the various incubation periods, symptom of microstructural changes.

It will be anticipated here that the conditions tested in this project were seven, for incubation periods of 0, 1, 2, 4, 7, 12 and 24 hours. Again, these were chosen according to the natural ageing precipitation theory, which will be illustrated in the next chapter.

4.3.2 Measurements schedule

As previously mentioned, both macrohardness and microhardness were constantly monitored during natural and artificial ageing. In the following the measurements schedules are reported.

The first condition to be analyzed was macrohardness - natural ageing. To obtain the data different samples were used and measurements were taken both on their top and bottom faces. When there was no space left for indentations on a sample, the following one was tested.

Table 4.1: Macrohardness measurements schedule during natural ageing.

Time of natural ageing	Measurements and time step
0 to 2 hours	1 indentation every 5 minutes
2 to 3 hours	1 indentation every 10 minutes
3 to 4 hours	2 indentations every 20 minutes
4 to 8 hours	2 indentations every 40 minutes
10 hours	2 indentations
13 hours	2 indentations
1 day	2 indentations every 8 h
2 to 6 days	2 indentations every 12 h
7 to 14 days	2 indentations every day

For the first 3 h a single measurement per time was taken, therefore the points plotted on the curves are raw data. Instead, when the performed indentations were two, their average was plotted on the final curve.

The higher frequency of measurements in the first hours derives from the need of having a higher density of results to better analyze the hardening behaviour in the early precipitation stages.

This approach was adopted for the microhardness as well, where the time gap between two consecutive indentations did not exceed 15 minutes in the first 16 hours. Such a dense schedule was dictated by the necessity of a very high quantity of data to formulate a truthful precipitation theory.

As for the macrohardness the points plotted in first 16 hours are raw data, instead when 5 indentations were performed at the same time their average was considered.

The measurements were all taken on the top surface of a single sample.

Table 4.2: Microhardness measurements schedule during natural ageing.

Time of natural ageing	Measurements and time step
0 to 3 hours	1 indentation every 2 minutes
3 to 8 hours	1 indentation every 5 minutes
8 to 12 hours	1 indentation every 10 minutes
12 to 16 hours	1 indentation every 15 minutes
1 day	5 indentations every 8 h
2 to 6 days	5 indentations every 12 h
7 to 14 days	5 indentations every day

Regarding artificial ageing the reported measurement schedules are the same for all the different incubation periods and, to freeze the microstructure condition, samples were quenched in water at room temperature when pulled out of the furnace.

For the macrohardness, measurements were again performed on both top and bottom faces but, in this case, the samples were alternated at every measurement session. In such a way it was ensured that they were kept in the furnace for at least 2 hours between two consecutive tests.

The average of the 3 indentations performed per session was then plotted.

Table 4.3: Macrohardness measurements schedule during artificial ageing.

Time of artificial ageing	Measurements and time step
10, 20 and 40 minutes	3 indentations
1.5, 3, 6, 12, 18 hours	3 indentations
24 to 96 hours	3 indentations every 12 h

For artificial ageing the microhardness schedule is the same of the macrohardness, with the only difference that the plotted average is the result of 5 indentations rather than 3, if outliers were not found, as it will be explained later.

Tests were performed only on the polished surface of samples, which where alternated in the first four sessions. After those a single sample was chosen and all the measurements were carried out on it.

Table 4.4: Microhardness measurements schedule during artificial ageing

Time of artificial ageing	**Measurements and time step**
10, 20 and 40 minutes	5 indentations
1.5, 3, 6, 12, 18 hours	5 indentations
24 to 96 hours	5 indentations every 12 h

5. Results and discussion

In this chapter the curves resulting from the hardness measurements and the considerations drawn from the analysis of their trends are going to be illustrated.

It should be remarked that attention will be particularly paid to the microhardness since, as already mentioned, it provides a more direct evaluation of the precipitation sequence with respect to macrohardness; in the latter indeed hardness values are even influenced by factors such as grain boundaries and remaining eutectic phases.

5.1 T4 heat treatment

In the T4 treatment samples were submitted to natural ageing; firstly the macrohardness evolution of the three shown alloy compositions was studied and then, only on two alloys, the microhardness was evaluated as well. Based on the results of the latter, a prediction of the precipitation sequence was formulated.

5.1.1 Macrohardness evolution

Figure 5.1 presents the macrohardness evolution of the three compositions analyzed during natural ageing. The measurements were performed according to Table 4.1 and the standard deviation is shown for those data resulting from the average of two values.

In every alloy the registered level of hardness after quenching is very low, an indication that solute atoms are still dissolved in the SSSS. Thus the main parameters affecting macrohardness in the as quenched condition are residual eutectic phases and solute concentration. With reference to the second, the comparison between the curves highlights how a higher solute concentration leads to a higher hardness; having the lowest solute content Al-3.6Zn-1.8Mg is characterized by the lowest initial hardness, whereas Al-6Zn-2.2Mg-2.3Cu presents the highest one. This occurs because a high quantity of solute atoms increases the residual strain of the matrix and thus acts as a barrier to dislocations motion.

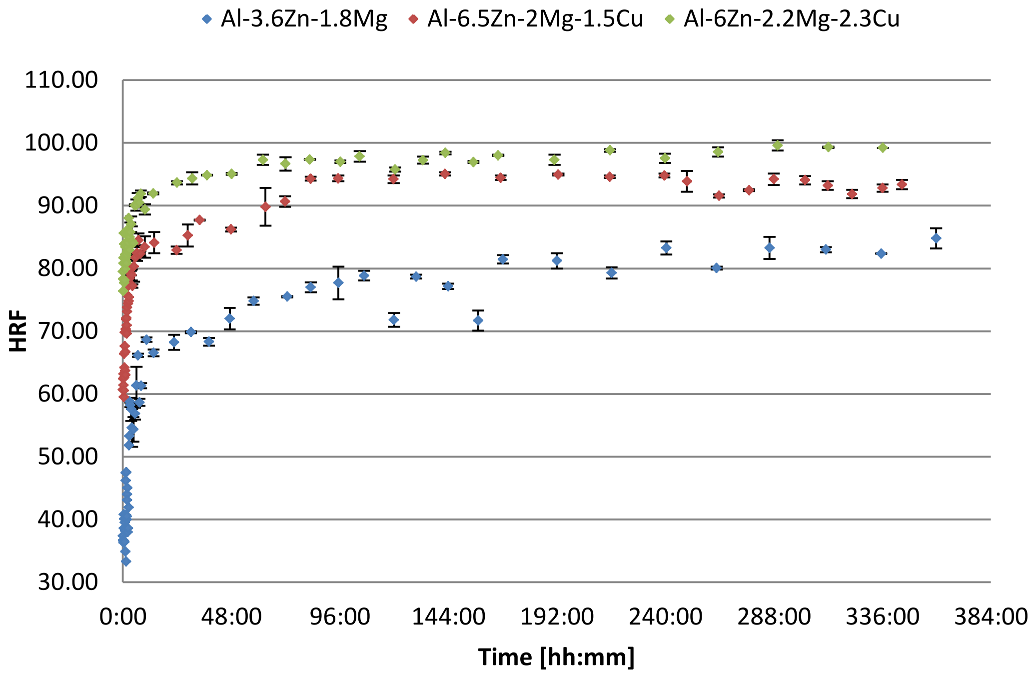

Figure 5.1: Macrohardness evolution of the shown alloy compositions during natural ageing.

Though the hardness difference between the curves decreases with the formation of precipitates and reaches a minimum after 10 days, indicating that alloys with a low solute content are more age hardenable and that, at long ageing times, solute content itself does not influence the hardness as much as in the early stages of precipitation. As it could be expected, this means the influence of precipitates on the material hardness is more relevant than that of the quantity of solute dissolved in the matrix after quenching. Then the only way solute content affects the hardness when stable precipitates are formed is that a higher concentration leads to a greater amount of precipitates, thus to higher macrohardness values. A low level of supersaturation requires longer times for precipitates to form since the solute density is lower and atoms have to diffuse across longer distances. This is confirmed by the image above, where Al-6Zn-2.2Mg-2.3Cu only takes 62 h to form stable precipitates, indicated by a constant hardness level, Al-6.5Zn-2Mg-1.5Cu needs 83 h and Al-3.6Zn-1.8Mg takes between 7 and 10 days.

The low values of standard deviation that were recorded suggest a low variability between the measurements, while the values of those points away from the general trend (data at 119:54 and 157:13 hours in Al-3.6Zn-1.8Mg) are attributable to the particular morphology of certain spots on samples surface. It should be mentioned though that a low variability is typical of the macrohardness, since the indentation area is wide.

The following image presents an enlarged view of the first 30 h of measurements.

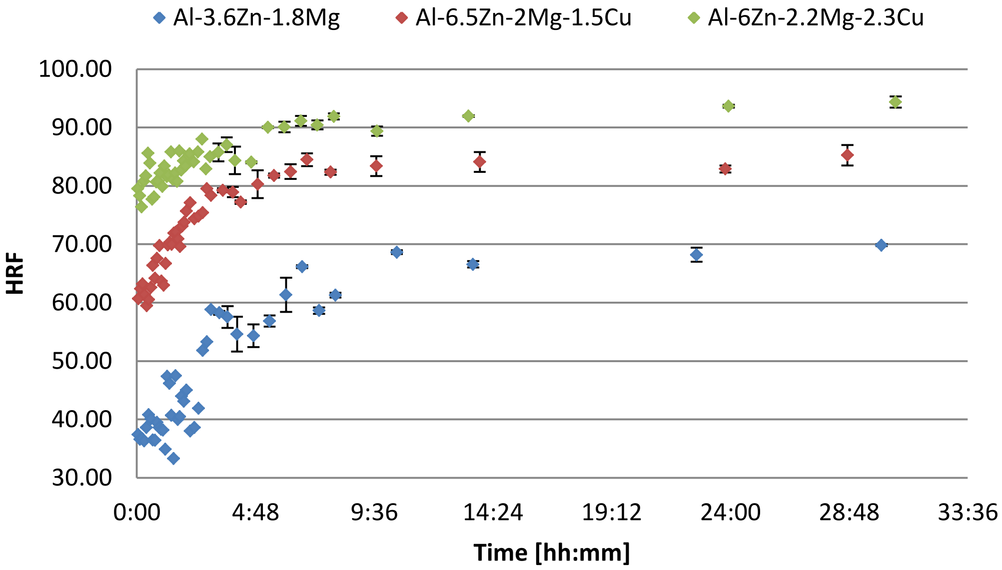

Figure 5.2: Macrohardness evolution of the shown alloy compositions during the first 30 h of natural ageing.

The first 60 minutes of ageing prove how the presence of Cu promotes a rapid hardening of the material in the early precipitation stages [32]. The green and red curves indeed are characterized by an approximate hardness increase rate of 2.2 $\frac{HRF}{h}$ and 5.2 $\frac{HRF}{h}$ respectively, while the Cu free alloy has a slope of 0.1 $\frac{HRF}{h}$[5]. Although, since the highest slope value does not belong to the alloy with the highest Cu content, it is plausible that other factors affect the hardening rate during early ageing. With reference to the importance of the Zn/Mg ratio in the formation of solute clusters and of stable GPI, it can be observed that to a high HRF increase rate corresponds a high Zn/Mg, symptom that this parameter plays an essential role in the nucleation of early precipitates.

Based on the obtained results, the alloys leading to the highest and lowest hardness level were selected to continue the project, thus no further measurements were performed on Al-6.5Zn-2Mg-1.5Cu.

---

[5] Slopes were calculated with a linear fit operation performed on data obtained during the first 60 minutes of ageing.

5.1.2 Microhardness evolution

The microhardness test was carried out on Al-6Zn-2.2Mg-2.3Cu and Al-3.6Zn-1.8Mg alloys only. Indentations were performed according to Table 4.2 and, as for the macrohardness, the standard deviation is shown for those data resulting from the average of different values.

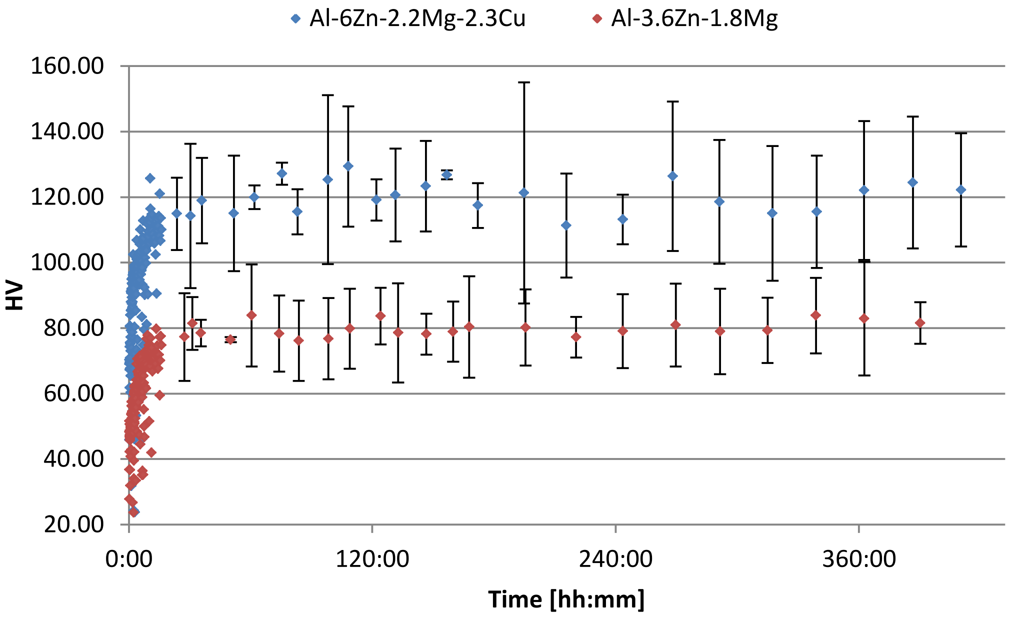

Figure 5.3: Microhardness evolution of the shown alloy compositions during natural ageing.

Like in the macrohardness, HV values are low in the early stages of ageing and increase with the formation of precipitates. Again, the alloy containing the higher amount of solute is characterized by a higher level of microhardness; in this case though the hardness difference between the two curves does not decrease with ageing time, but remains constant. This behaviour is linked to the different nature of microhardness with respect to macrohardness; microhardness values indeed are not as deeply affected by precipitates formation as macrohardness ones. This occurs because, the indented area being smaller, the number of precipitates hindering the indenter penetration does not increase significantly with ageing time, so that microhardness stops increasing once the majority of the precipitates have formed. However in the volume indented by the macrohardness, precipitates nucleating in the late stages of ageing are more numerous and therefore they affect the hardness values to a greater extent.

This concept also explains why, unlike for the macrohardness, the two alloys reach a stable level of microhardness after almost the same ageing time; late nucleating precipitates in fact do not lead to a microhardness increase.

On the other side, a small area of indentation makes the hardness more susceptible to variations, as demonstrated by the standard deviations of Figure 5.3; when only few elements determine the result of a certain quantity, even a small change in their number may cause a relevant variation in the measured quantity. In the microhardness then, the high variability of vacancies and solute clusters distribution is responsible for the obtained variation.

Furthermore, the higher the number of elements submitted to changes, the higher the variation is going to be; this is why in the Cu containing alloy standard deviation values are higher than in the Cu free alloy. If in the latter only two types of regions characterize the microstructure, without precipitates and with precipitates, in the former one more region is present: without precipitates but with Cu atoms dissolved in the matrix.

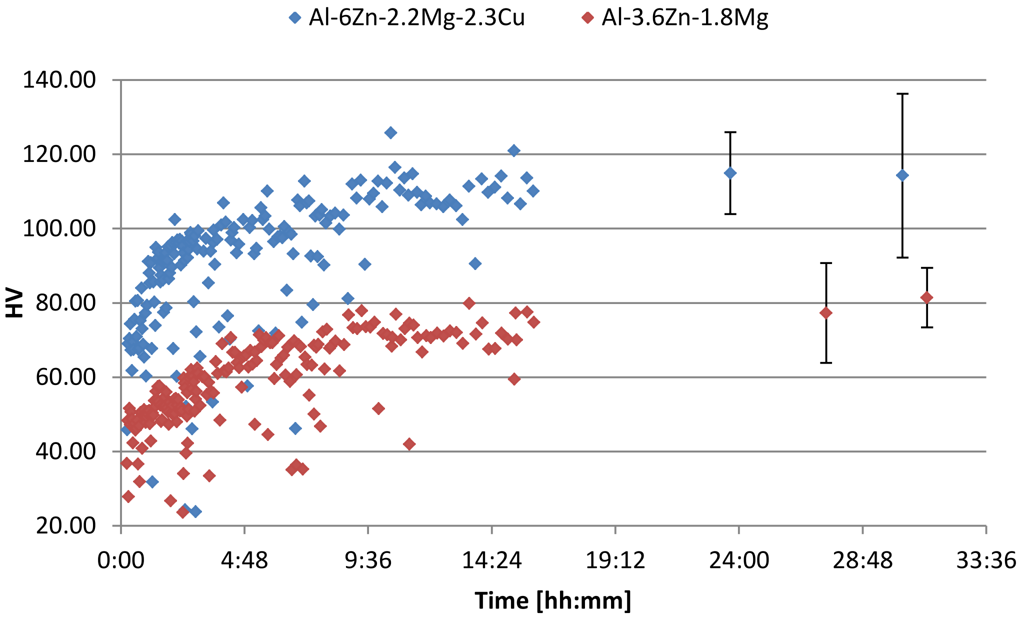

Figure 5.4: Microhardness variation of the shown alloy compositions during the first 30 h of natural ageing.

Figure 5.4 focuses on the first 30 h of natural ageing. Here, more than in Figure 5.2, the influence of Cu and Zn/Mg on the hardening rate in the early precipitation stages is visible. Besides, the more scattered data of Al-6Zn-2.2Mg-2.3Cu in the first 16 h confirm the higher microhardness variation typical of Cu containing alloys.

The presence of the aforementioned microstructure regions is detectable in the above graph. Each alloy is indeed characterized by a band with a high density of data and by a zone, underneath this band, where data are more dispersed; a measurement falls in the former if a patch with precipitates is indented, otherwise it falls in the latter. It is likely that Al-6Zn-2.2Mg-2.3Cu data overlapped to the Al-3.6Zn-1.8Mg curve belong to regions without precipitates and with a low concentration of Cu, whereas those areas without precipitates but with a high Cu content generate those points between the blue and red data dense bands.

More generally these regions can be divided in two categories only, with or without precipitates, and both of them contribute to the microhardness increase during ageing. The contribution of the first one is related to precipitates evolution, whereas that of the second one comes from matrix changes, more specifically from the vacancy depletion caused by atoms diffusion[6]. Indeed, as it was already explained, atoms, by moving, destroy the vacancies present in the matrix, thus leading to an increase in the material hardness.

It should be remembered that the matrix effect is present even in those areas with precipitates, so that vacancy depletion is a phenomenon affecting the overall material hardness. Therefore microhardness is always affected by the matrix morphology and in some cases by the presence of precipitates as well.

In the figures below all the raw data, without averages, are reported and the matrix contribution region is highlighted between two black lines. As it can be observed in Figure 5.5 and Figure 5.6, microhardness values related to vacancies depletion follow the path of those connected to precipitates nucleation and growth. In fact they are strictly related, since the formation of precipitates implies atoms diffusion and then vacancy destruction. When the SSSS still exists the *vacancy induced hardness* is low, then, with the nucleation of the first solute clusters, it starts increasing until it reaches a constant level when stable precipitates, probably GPI, have been formed.

---

[6] Hardness values mainly related to precipitates evolution will be referred at as *precipitates induced hardness*, while those influenced by the depletion of vacancies will be addressed as *vacancy induced hardness*.

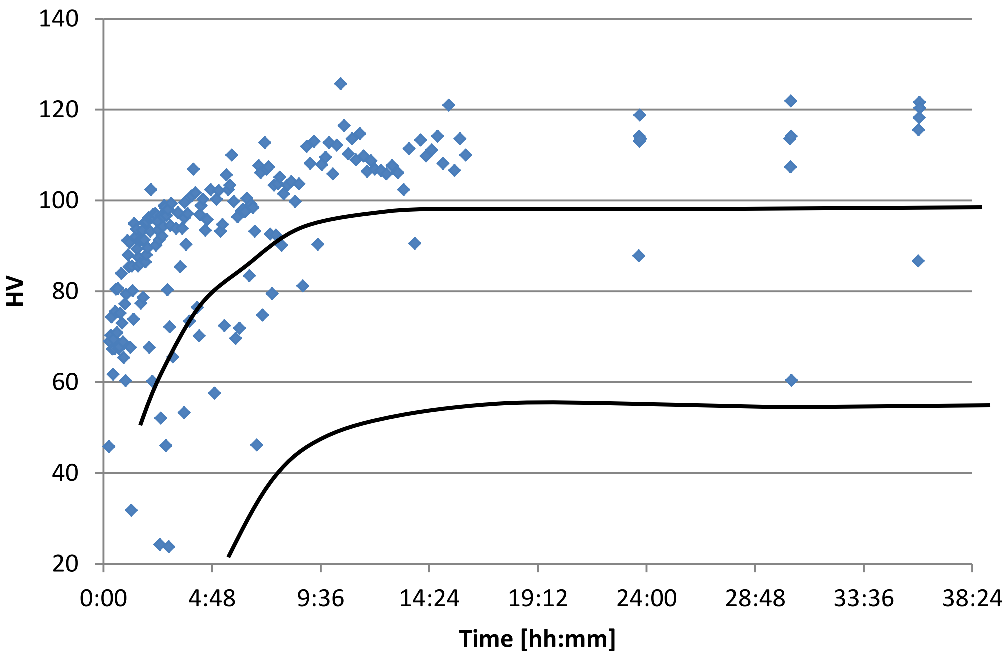

Figure 5.5: Raw microhardness data of Al-6Zn-2.2Mg-2.3Cu alloy in the early stages of natural ageing, with highlighting of *vacancy induced hardness* values.

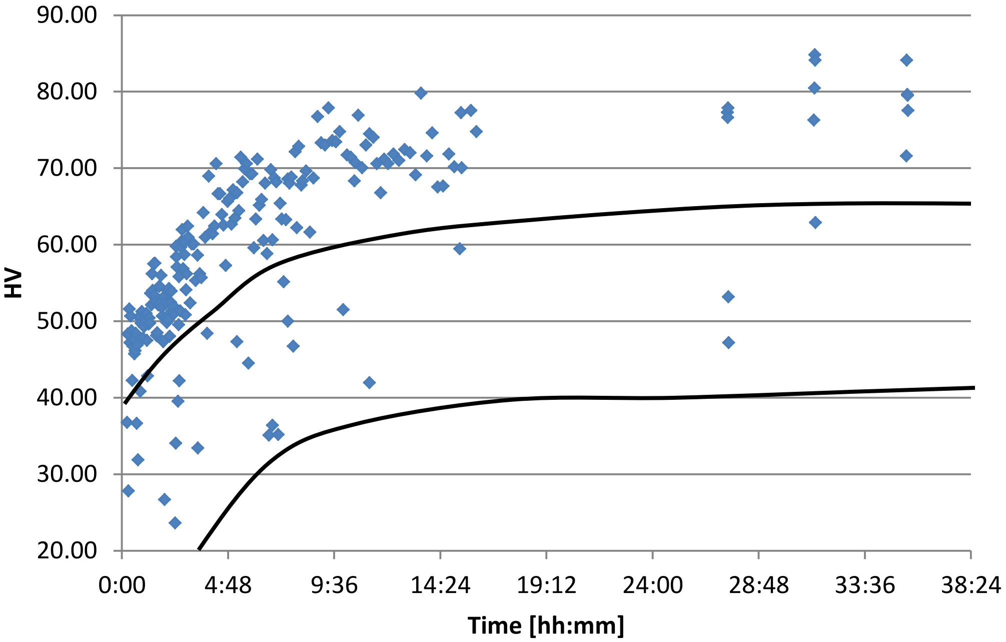

Figure 5.6: Raw microhardness data of Al-3.6Zn-1.8Mg alloy in the early stages of natural ageing, with highlighting of *vacancy induced hardness* values.

By stretching the black lines, it is possible to identify the range of *vacancy induced hardness* at longer ageing times, as shown in Figure 5.7 and Figure 5.8.

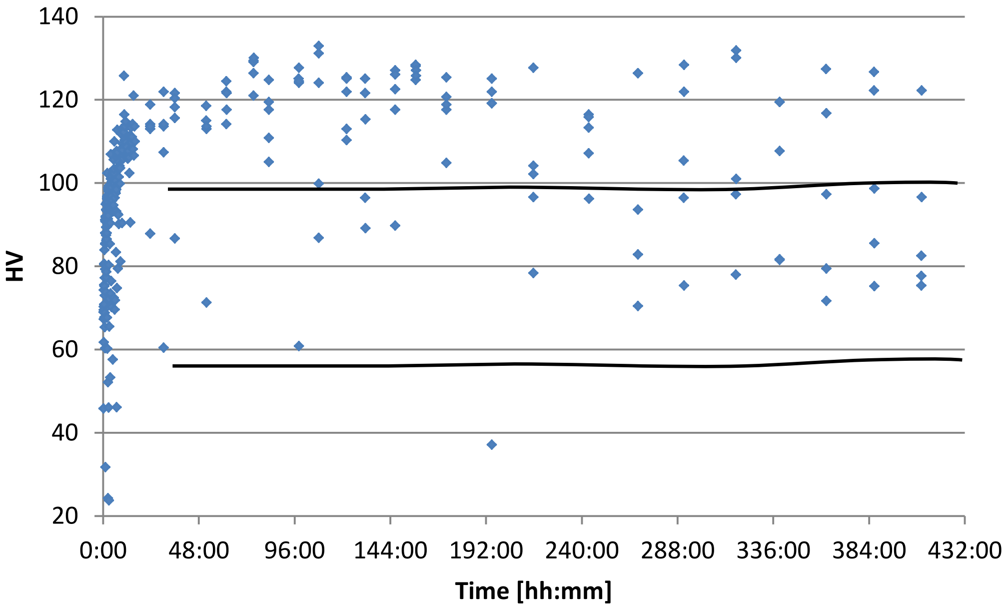

Figure 5.7: Raw microhardness data of Al-6Zn-2.2Mg-2.3Cu alloy during natural ageing, with highlighting of *vacancy induced hardness* values.

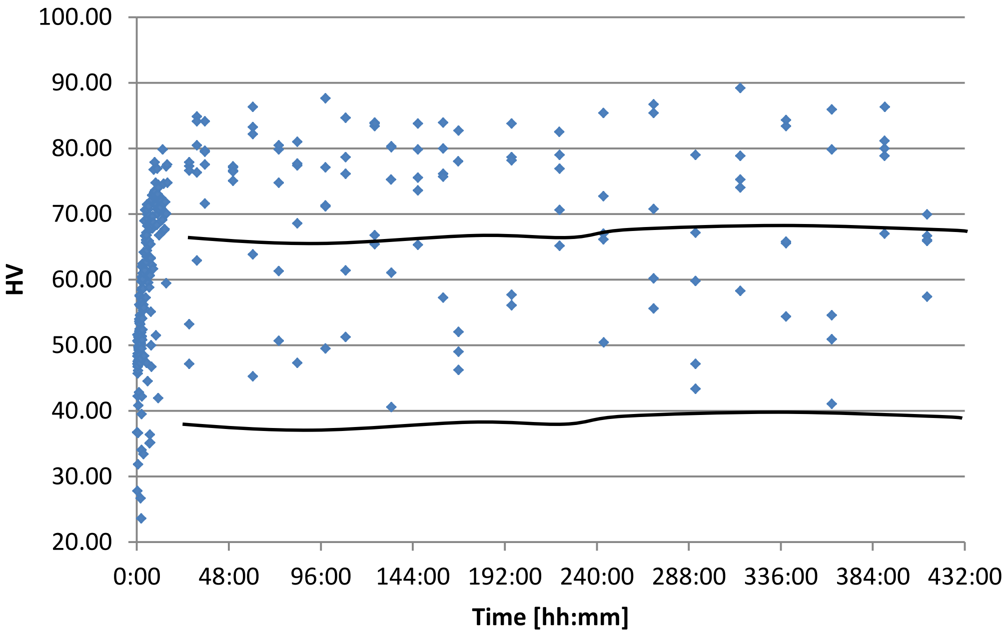

Figure 5.8: Raw microhardness data of Al-3.6Zn-1.8Mg alloy during natural ageing, with highlighting of *vacancy induced hardness* values.

According to the recognized bands of *vacancy induced hardness*, the averages of each measurement session were calculated (averages are plotted in Figure 5.3). More precisely, to avoid too scattered results and to have a graph mostly representative of *precipitates induced hardness*, those data falling into the highlighted regions were considered outliers and not included in the averages computation.

At this point, the objection could be then raised that was stated above, about the results variation linked to the presence of different microstructure regions, is no longer valid since the matrix contribution region was not taken into account in the averages calculation. Actually vacancy depletion is still accounted for, since the matrix effect is present even in those areas with precipitates. In other words, *precipitates induced hardness* is influenced by both precipitates and vacancies, whereas *vacancy induced hardness* is just influenced by vacancies themselves.

Now, it is still necessary to analyze *precipitates induced hardness*, since it is from its trend that assumptions could be made about the precipitation sequence.

From an accurate observation of Figure 5.4, different regions can be recognized in the microhardness evolution. It is interesting to notice how their time division does not vary between the two alloys, hint that precipitates mechanisms occurring in the analyzed compositions are the same, even if they lead to different hardness levels; these regions are illustrated in Figure 5.9.

According to the literature, early stages of precipitation in artificial ageing are characterized by the formation of small GPI with a Zn/Mg ratio smaller than 1, clue that Mg diffusion and agglomeration is a key factor in the nucleation of GPI zones. Therefore, since GPI is the only precipitate evolving during natural ageing, it is likely that early stages of ageing feature the formation of Mg rich clusters. More precisely, with reference to the image below, it is likely in regions *Ia* and *Ib* Mg atoms diffuse to gather into small solute rich clusters.

The nucleation of these clusters is not a one way process, but it is rather dynamic, with Mg atoms continuously associating and dissociating in the matrix. Hardness increase, in this stage, is related to the chance the number of forming clusters is higher than that of dissolving ones, and to vacancies destruction, caused by the continuous atoms diffusion.

To promote a rapid hardening of the material, it is therefore essential that something keeps Mg clusters tied together, in order to prevent their dissolution. According to the literature, this role is played by Cu, which in the early precipitation stages joins Mg clusters, thus bonding them [32]. This idea is confirmed by the image below, where, in the first two hours of ageing denoted as region *Ia*, the slope of Al-6Zn-2.2Mg-2.3Cu is higher than that of Al-3.6Zn-1.8Mg.

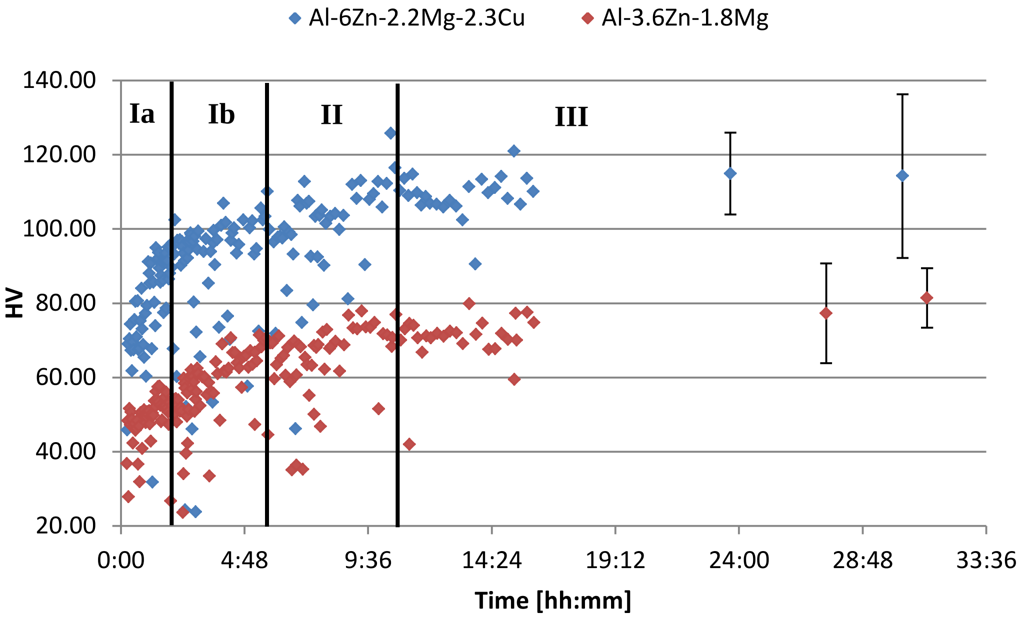

Figure 5.9: Precipitates evolution regions of the shown alloy compositions in the first 30 h of natural ageing.

After the first 2 hours, the two curves run almost parallel through all the other regions, symptom that the effect of Cu on material hardening is over.

In Al-3.6Zn-1.8Mg there is not any difference between region *Ia* and *Ib*, since the subdivision was created to highlight the effect of Cu in Al-6Zn-2.2Mg-2.3Cu. Therefore, because of the continuity with region *Ia*, from the 2nd to the 5th hour of ageing Mg clusters are still forming in both the alloys. It should be mentioned that, according to researches carried out on other Zn containing aluminum alloys [11], it is plausible in the early stages Zn rich clusters are being formed as well. Although, the absence of specific information in the literature, about the presence of these compounds in 7xxx series alloys, and the lack of chemical or microscopical analyses prevent the confirmation of this assumption. Therefore region *I* will be generally addressed as *clusters formation* stage.

Region *II* is characterized by little bounces in the hardness. It is likely these are related to clusters which dissociate and form again with a bigger size, since following peaks are characterized by increasing microhardness values. One possible mechanism explaining this behavior is the formation of Mg and Zn co-clusters, meaning in this stage Mg and Zn atoms are joining together in those compounds that will eventually result into early GPI.

Several are the ways that could lead to co-clusters appearance. Although, knowing for sure that Mg clusters are the starting point of GPI formation and that their Zn/Mg ratio constantly increases until stability is reached, it is possible to assume that Zn atoms join already present Mg clusters. But to do so, some of the Mg or Zn solute rich clusters, formed during the *clusters formation* stage, must dissolve. Zn clusters should dissolve to provide atoms for the formation of co-clusters, whereas Mg clusters should partially dissolve to attract Zn atoms. This whole process would then result into the bounces visible in region *II*, which is going to be called *co-clusters formation* stage.

At the end of the second stage early GPI zones, or co-clusters, are therefore present in the microstructure. In the last region, they slowly grow in size by constantly attracting Zn atoms, until a stable Zn/Mg ratio, greater or equal to 1, is reached.

The *co-clusters growth* stage begins after 10 hours of natural ageing and, because of the slow pace at which remaining Zn atoms join early GPI zones, it is characterized by a low hardness increase rate, which becomes null once stable GPI have been formed.

At this point of the discussion, it is necessary to stress what is reported above is just a hypothesis of the precipitation sequence occurring during natural ageing. Before claiming its correctness, it is indeed necessary to verify it, by analyzing the behavior of the two alloys during artificial ageing.

The verification was performed by submitting the samples to different incubation periods (IP) prior to artificial ageing, in order to study the influence of the various described processes, taking place during natural ageing, on the artificial ageing behavior of the material.

Based on the aforementioned precipitation sequence, 7 different incubation periods were selected, which correspond to the following stages: start, half and end of region *Ia*, half of region *Ib*, half of the *co-clusters formation* stage, start and end of the *co-clusters growth* stage.

5.2 T6 heat treatment

Artificial ageing measurements, in each condition, were carried out according to the schedules illustrated in Table 4.3 and Table 4.4, while the different adopted incubation periods (IP) were 0, 1, 2, 4, 7, 12 and 24 hours.

5.2.1 Macrohardness evolution

Macrohardness evolution curves, obtained for every incubation period, are individually plotted in Appendix A. In the following instead all the curves are presented together, in graphs that clearly show how hardness values evolve during artificial ageing, with respect to natural ageing.

It should be explained, in the following images, points are linked with line for sake of clarity; in fact, if scattered values were plotted the trend of each condition wouldn't have been discernable. The natural ageing curve is labelled as T4, whereas artificial ageing curves are addressed with #IP, where the number before IP indicates the hours of incubation periods.

In every artificial ageing curve, the starting point is the measured natural ageing value closest to the time at which artificial ageing was started. For example, in the 24 IP curve of Figure 5.10, the first point was taken after 22:38 hours of natural ageing. In such a way the hardness trend during the first minutes of artificial ageing, with respect to natural ageing, is immediately visible.

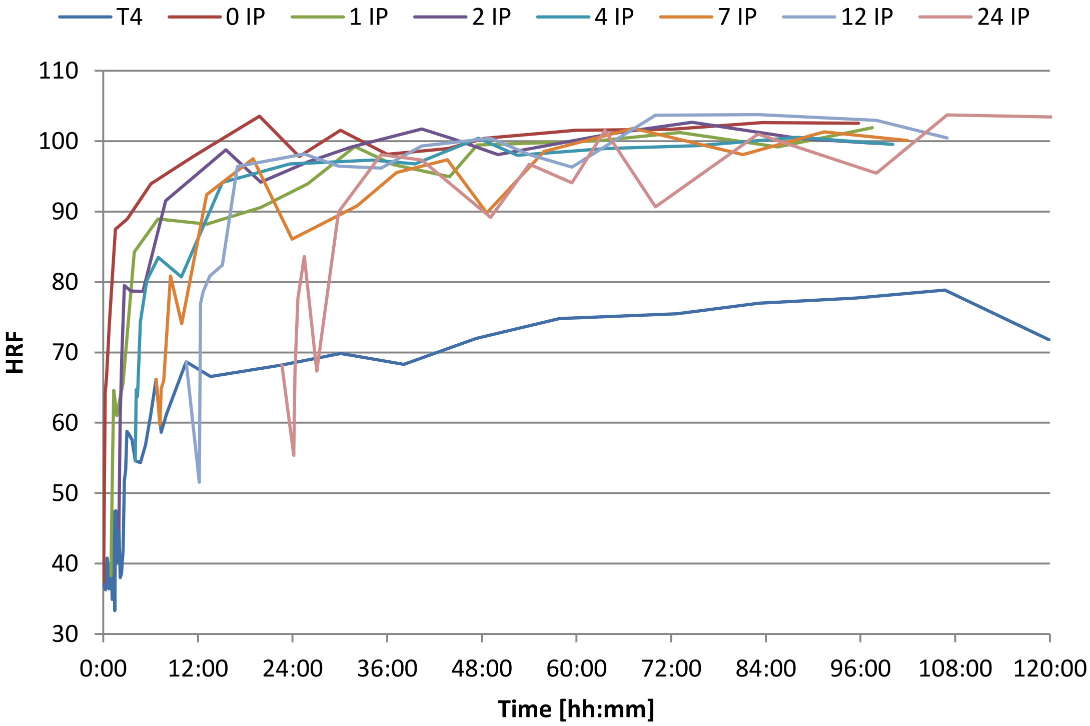

Figure 5.10: Macrohardness evolution of Al-3.6Zn-1.8Mg during the first 120 hours of natural ageing (T4) and in the different artificial ageing conditions (#IP).

The above graph confirms how, by holding samples at ageing temperatures higher than room temperature, the type of precipitates evolving inside the microstructure are completely different and, as explained in section 3.2.4, the measured hardness level is higher. Indeed, while in natural ageing the biggest precipitate forming is GPI, during artificial ageing η' and η may nucleate, so that, since these constitute a bigger obstacle for dislocations motion, the resulting material strength is increased.

It is interesting to notice how, in the obtained results, a decrease in the macrohardness was not observed even after 4 days of artificial ageing, meaning the overaged condition was not reached. Therefore it is possible to claim 120 °C is a safe ageing temperature, since it does not generate a fast overageing, and material properties can thus be preserved.

According to what reported in section 3.2.4, the absence of the overaged condition would induce the belief that η did not form inside the matrix, and only coarse GPI and η' are present. Although, since a microscopical analysis was not carried out to confirm this statement, from now onward precipitates characterizing the microstructure at the end of artificial ageing will be addressed as *artificial ageing stable co-clusters*. These are different from the stable co-clusters found during natural ageing (GPI), even though some of them are probably present in the artificially aged condition as well.

From the analysis of a single curve, it is possible to see how precipitates, present in the matrix at the end of the incubation period, evolve into intermediate compounds (first knee of every curve), which eventually result into *artificial ageing stable co-clusters* (flat final trend). The level of hardness reached by these co-clusters does not vary with changing incubation periods, meaning this parameter does not affect the type of precipitates evolving inside the microstructure. Instead, what it does influence is the time required for the formation of *artificial ageing stable co-clusters*. As it will be better analyzed through the microhardness evolution, the longer a sample is held at room temperature, before artificial ageing, the longer it will take to reach its peak hardness.

Besides, it is interesting to notice how, for the longer incubation periods of 7, 12 and 24 hours, the hardness after 10 minutes of artificial ageing is lower than the one observed in samples naturally aged for a time as long as the incubation period itself. This probably occurs because, as mentioned in section 3.2.4, η' evolves both from small GPI and from solute atoms deriving from dissolving GPI. Therefore, as a clue of the correctness of the formulated precipitation theory, since after 7 hours of natural ageing early GPI begin to form, during artificial ageing some of these dissolve to provide solute for the nucleation of intermediate compounds (probably elongated GPI zones as reported in the literature), so that the macrohardness initially decreases.

Finally, by looking at the standard deviations of figures in Appendix A, it is clear how the discussion about macrohardness variability in natural ageing holds for artificial ageing as well.

In Figure 5.11 the behavior of Al-6Zn-2.2Mg-2.3Cu is illustrated.

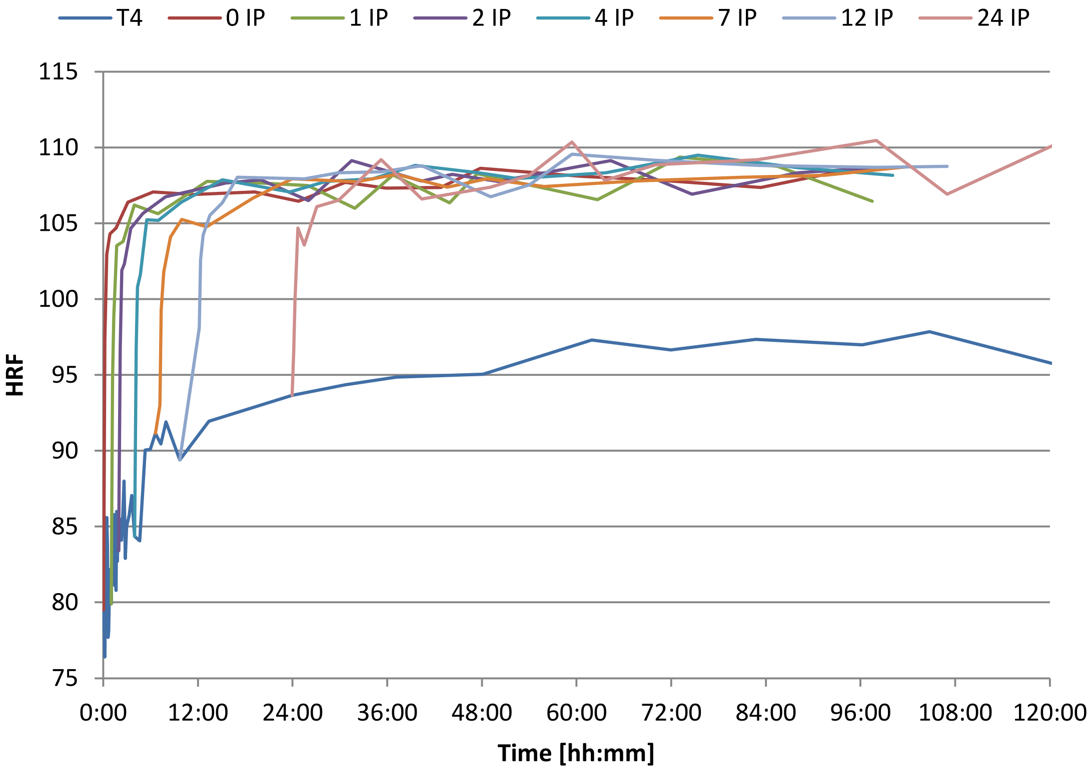

Figure 5.11: Macrohardness evolution of Al-6Zn-2.2Mg-2.3Cu during the first 120 hours of natural ageing (T4) and in the different artificial ageing conditions (#IP).

All the considerations exposed for the Al-3.6Zn-1.8Mg are valid for this alloy as well, apart from the early stages behavior in the 7, 12 and 24 hours incubation period conditions. In Al-6Zn-2.2Mg-2.3Cu indeed the observed hardness, after 10 minutes of artificial ageing, is higher than that of natural ageing. Nevertheless this does not contradict the formulated precipitation theory but, instead, it adds more information. As a matter of fact, as confirmed by studies that are being carried out, contemporary to this, on CDS cast 7xxx series alloys, Cu containing alloys are characterized by denser and smaller precipitates than Cu free alloys. Therefore, if GPI zones present in the microstructure after 7, 12 and 24 hours of incubation period are small, the chance intermediate precipitates will evolve from GPI rather than from the SSSS is higher; thus less GPI dissolve and the hardness does not decrease.

As in natural ageing, the hardness level reached by Al-6Zn-2.2Mg-2.3Cu is higher than in Al-3.6Zn-1.8Mg, since the amount of solute is higher in the first alloy, while the observed overall hardness increase is higher in the second alloy, which confirms that samples characterized by a lower solute content are more age hardenable. This occurs because a lower solute content, as described in Figure 3.26, requires a bigger critical radius for nucleation, so that precipitates forming in the microstructure are bigger, and big precipitates, in turn, result into a higher hardness. Despite this, the difference in solute content between the two studied alloys is so high that the just explained effect is not enough for Al-3.6Zn-1.8Mg to overcome the hardness of Al-6Zn-2.2Mg-2.3Cu.

Obviously, the nucleation radius concept further validates the idea that GPI zones, after 7, 12 and 24 hours of natural ageing, are smaller in the Cu containing alloy than in the Cu free one, because of the highest solute concentration.

5.2.2 Microhardness evolution

Like in natural ageing, microhardness evolution provides a clearer hint on the precipitation sequence with respect to macrohardness, because of its higher sensitivity.

It should be mentioned, unlike in natural ageing, outliers were considered only those measurements 30 HV higher or lower than the computed average.

The same approach used for the macrohardness is adopted here, with single artificial ageing curves plotted in Appendix B, while the main discussion is focused on graphs containing every studied condition.

The analysis of the standard deviations in Appendix B indicates again how microhardness data are characterized by a higher variation with respect to macrohardness ones, as well as the Cu containing alloy with respect to the Cu free.

Figure 5.12 shows the behavior of Al-3.6Zn-1.8Mg. Again, the registered values of microhardness during artificial ageing are higher than those observed during natural ageing. Moreover, better than in macrohardness data, it is visible here how incubation period clearly influences the time to peak hardness, which, on the other side, remains almost constant between the different curves.

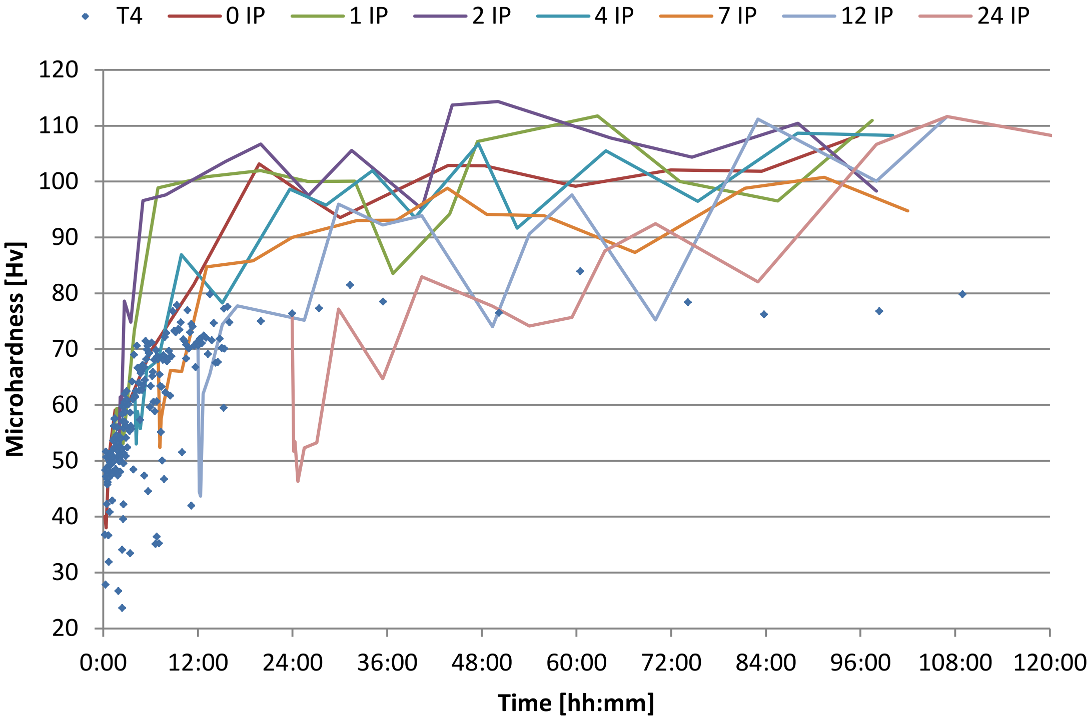

Figure 5.12: Microhardness evolution of Al-3.6Zn-1.8Mg during the first 120 hours of natural ageing (T4) and in the different artificial ageing conditions (#IP).

For a better understanding of the mechanisms taking place during artificial ageing, and to validate the formulated precipitation theory, the hardening rate observed during early ageing stages and the time to peak hardness were plotted with respect to the *vacancy induced hardness*, measured at the different incubation periods.

First of all, based on the band division of Figure 5.5, *vacancy induced hardness* values were separated from *precipitates induced hardness* ones. Then, with a data compiler, the following equation, based on vacancy diffusion law at room temperature, was found to be the best fit for the data[7].

$$y = \frac{a}{x} + bx^2 + cx + d \tag{5.1}$$

Where $a = 0.0168$, $b = -4.68$, $c = 25.3$ and $d = 37$.

---

[7] The fitting of the curve was performed by the PhD student Reza Ghiaasiaan at McMaster University.

From the displayed equation, the values of *vacancy induced hardness* were then calculated and plotted as a function of the different incubation periods examined (Figure 5.13).

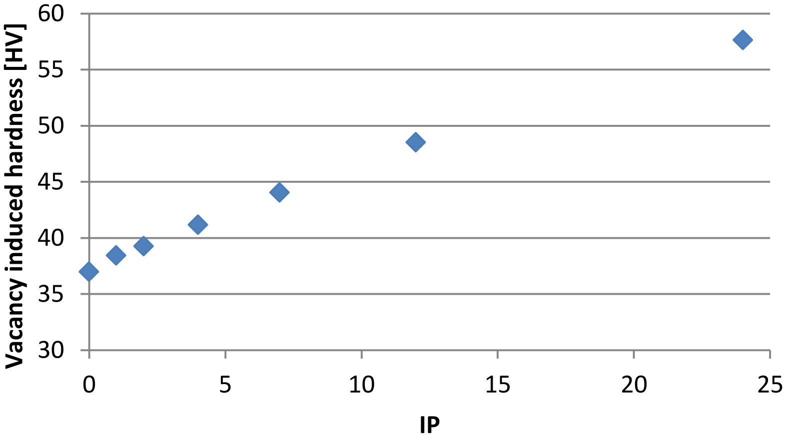

Figure 5.13: Calculated *vacancy induced hardness* values as a function of the incubation period in Al-3.6Zn-1.8Mg.

The initial slope of each curve was computed by considering the points before the knee, in order to study the hardening rate related to the formation of those intermediate precipitates which eventually evolve into *artificial ageing stable co-clusters*. Instead, as far as what concerns the time to peak hardness, the time coordinate of the first point with the highest average hardness was considered.

An example of how the above discussed quantities were obtained is illustrated in Figure 5.14, where the green points are those used to calculate the initial slope, whereas the red one is that considered for the peak hardness.

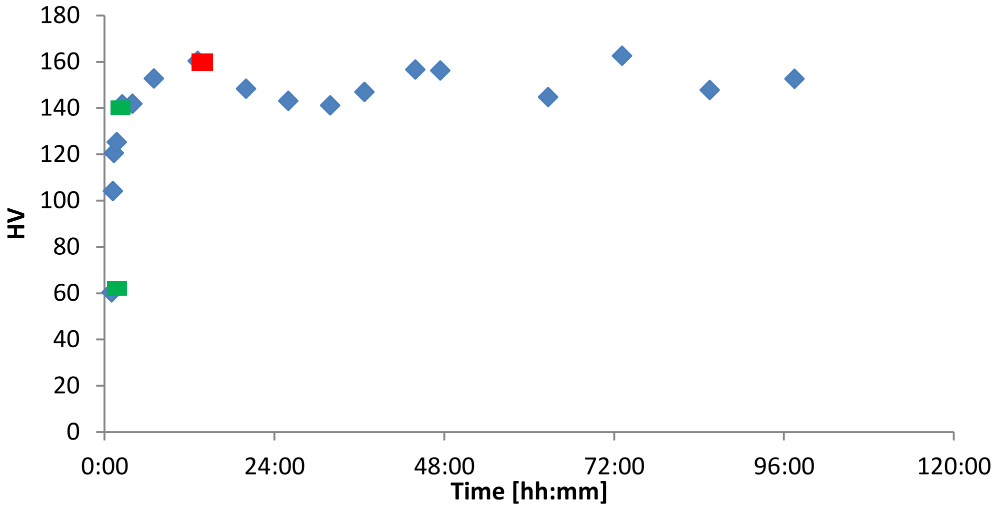

Figure 5.14: Example of points used for the calculation of the initial slope and the selection of the time to peak hardness.

Figure 5.15 shows the final relationship between initial hardening rate and *vacancy induced hardness*. It is clear how the hardening rate decreases with increasing *vacancy induced hardness*, and therefore with increasing IP for the relationship shown in Figure 5.13. This confirms the theory that vacancies are being killed during natural ageing by atoms diffusion, so that atoms mobility is lower in the early stages of artificial ageing. Indeed, a decreasing hardening rate simply means precipitates need more time to be formed, which occurs because vacancies have been depleted during the incubation period and atoms cannot diffuse as fast as if the sample was not held at room temperature.

More precisely, atoms mobility is not lower in the early stages of artificial ageing only, but during the entire ageing process. In fact, how the increasing time to reach the peak hardness demonstrates (Figure 5.16), not only the formation of early artificial ageing precipitates is more time demanding, but even *artificial ageing stable co-clusters* require more time to form and stabilize.

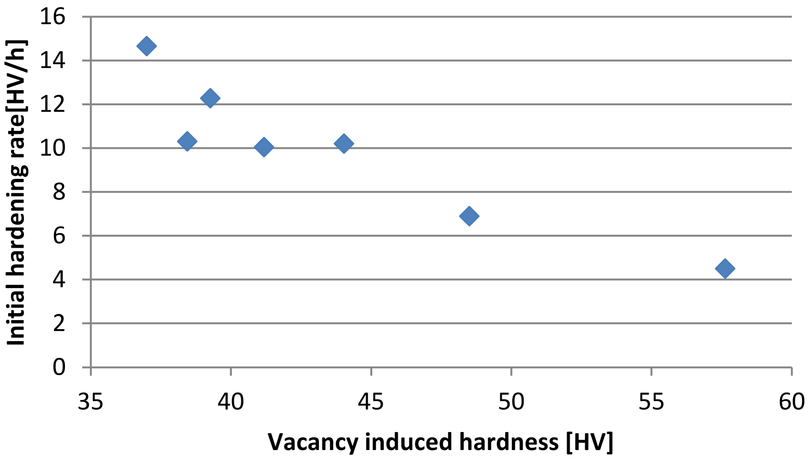

Figure 5.15: Initial hardening rate of Al-3.6Zn-1.8Mg during artificial ageing as a function of *vacancy induced hardness*.

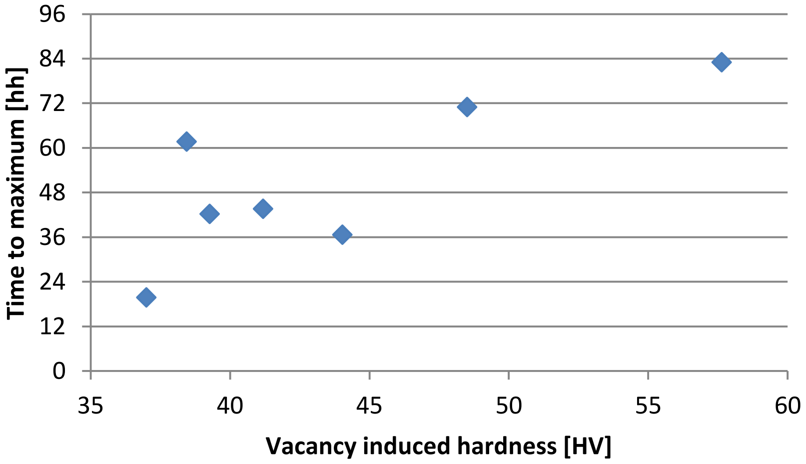

Figure 5.16: Artificial ageing time required to reach the maximum hardness as a function of *vacancy induced hardness*, in Al-3.6Zn-1.8Mg.

To better analyze the influence of the different incubation periods, and to verify the formulated precipitation theory, Figure 5.12 is going to be studied again, without the data relative to natural ageing.

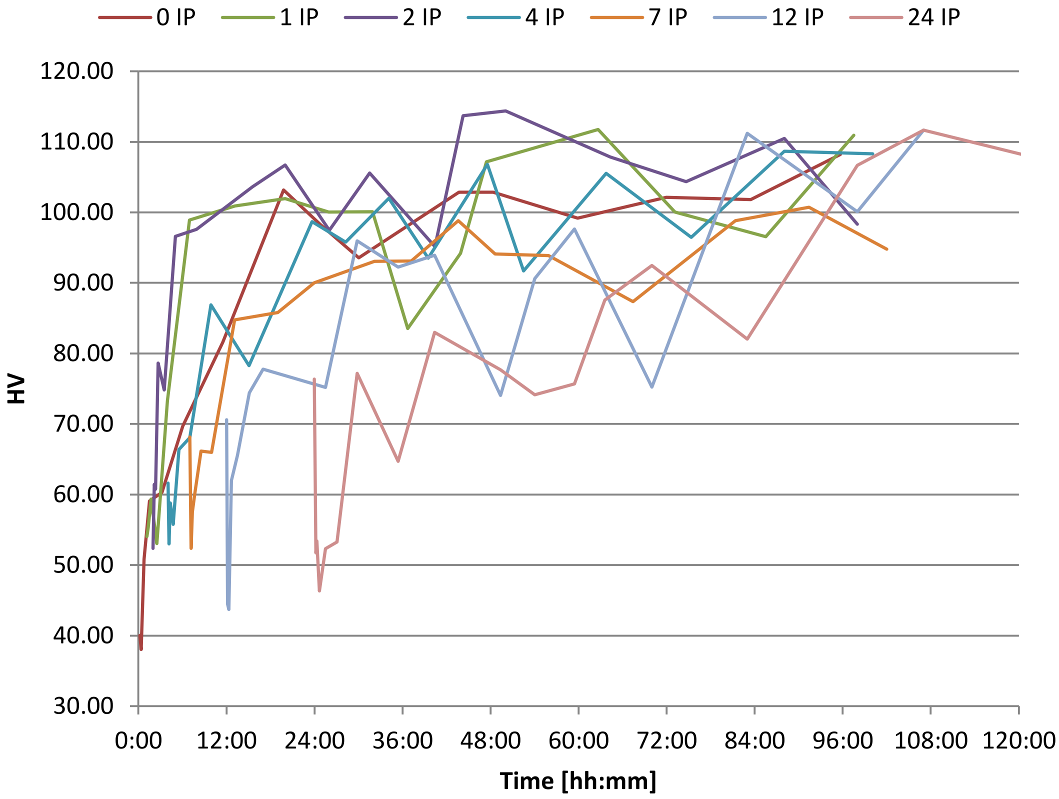

Figure 5.17: Microhardness evolution of Al-3.6Zn-1.8Mg in the different artificial ageing conditions.

- 0 IP curve is characterized by a very high initial slope, symptom that in the first 2 hours of ageing solute atoms quickly gather into small compounds (probably GPI, as reported in the literature) since all the solute and vacancies retained during quenching are still available. Although after 2 hours the slope of the curve drastically decreases. An in depth explanation of this sudden change requires an extensive microscopical analysis of the microstructure, but the idea of a fast initial hardening, related to the formation of GPI and early η', and a subsequent slow hardness increase, linked to the growth of η', was already observed in the literature.
- 1 IP shows a hardening rate lower than 0 IP and 2 IP in the early stages (Figure 5.15) and a particularly long *time to maximum* (Figure 5.16). According to the formulated precipitation theory, after 1 h of natural ageing solute rich clusters are forming inside the matrix and some vacancies have already been destroyed by atoms diffusion; this latter factor is likely to be the cause of the differences with 0 IP and 2 IP conditions.
- 2 IP features an initial lower number of available vacancies, so that a lower value of slope would be expected. Although solute rich clusters present in the microstructure

are bigger, so that the transformation of these early compounds into intermediate compounds occurs faster. Instead, in 1 IP the size of solute clusters is not big enough, and the influence of vacancy depletion is predominant.

- 4 IP marks almost the end of the *clusters formation* stage, where solute rich compounds are probably still growing in size. Nevertheless, the continuous destruction of vacancies balances out the advantage of a bigger compound, so that the hardening rate decreases and *time to maximum* remains constant.
- 7 IP lies in the *co-clusters formation* stage. Here clusters are evolving into early GPI, thus, as already observed in the macrohardness data, early stages of artificial ageing are characterized by a decrease in the material hardness attributable to the dissolution of some GPI. Moreover, from the above graph, it is discernable how this condition is characterized by an overall low level of reached hardness, probably linked to the particular condition of the microstructure. At the beginning of artificial ageing, in the microstructure there are indeed solute rich clusters evolving into early GPI, just formed GPI which evolves into elongated GPI, dissolving GPI and newly nucleating artificial ageing co-clusters. It is therefore likely this heterogeneity of precipitates reduces the overall solute amount available for *artificial ageing stable co-clusters*, so that the final hardness level is generally lower. To the lower hardness is then attributable the lower *time to maximum* registered.
- 12 IP and 24 IP prove how, by increasing the incubation period, the amount of big GPI present at the beginning of artificial ageing increases. Thus artificial ageing co-clusters need the dissolution of some of them to evolve, since only few small GPI are available; therefore the longer the incubation period the deeper the registered microhardness drops. Besides, as a proof of the high microstructure heterogeneity after 12 and 24 hours of holding at room temperature, the variation between the different measurements of the last two conditions should be compared to that observed in the previous ones.

Finally it is possible to claim the artificial ageing behavior of Al-3.6Zn-1.8Mg has been rationally explained based on the formulated precipitation theory, thus providing a validation to this one.

Having said of the Cu free alloy, it is now time to discuss the behavior of Al-6Zn-2.2Mg-2.3Cu, shown in Figure 5.18.

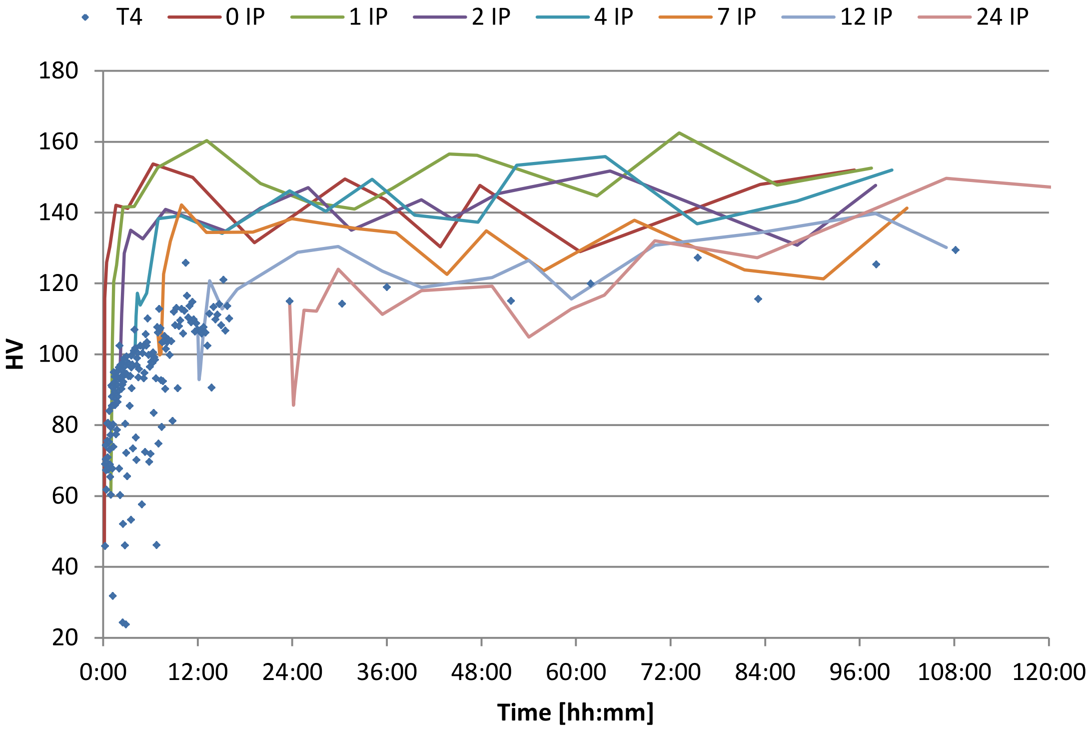

Figure 5.18: Microhardness evolution of Al-6Zn-2.2Mg-2.3Cu during the first 120 hours of natural ageing (T4) and in the different artificial ageing conditions (#IP).

Unlike in natural ageing, where the microhardness difference between the two alloys was almost constant from early ageing to the end of the treatment, in artificial ageing Al-6Zn-2.2Mg-2.3Cu shows a lower hardness increase with respect to Al-3.6Zn-1.8Mg, even though its microhardness values are averagely higher. This occurs because in artificial ageing precipitates are bigger than in natural ageing, therefore, even if the number of compounds forming in the indented area is not characterized by a big variation, their effect on hardness increase is not negligible.

Here as well, to clearly analyze the artificial ageing trend as a function of the incubation period, the hardening rate of early ageing stages and the *time to maximum* were plotted with respect to the *vacancy induced hardness*.

The procedure adopted for Al-3.6Zn-1.8Mg did not provide a good fit for this alloy, therefore the trendline characterized by the best R^2 was used to fit *vacancy induced hardness* data (Figure 5.19).

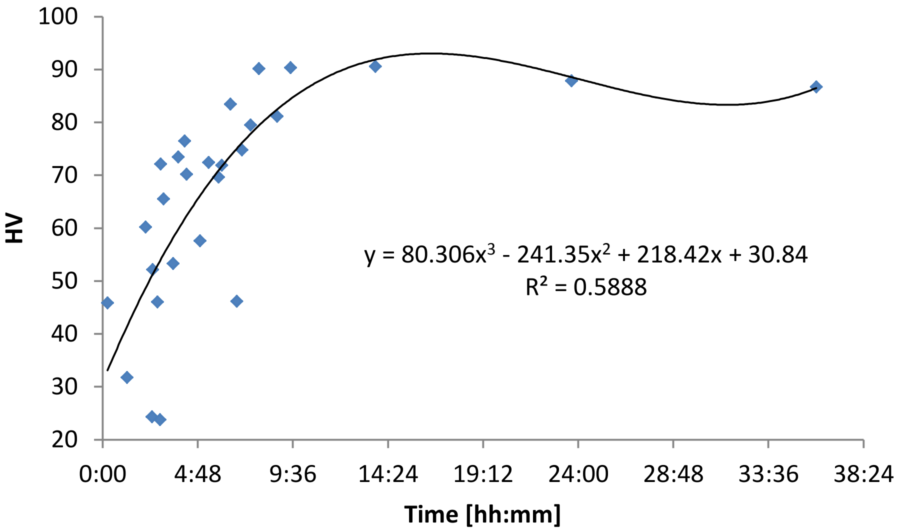

Figure 5.19: Fitting of *vacancy induced hardness* data in the first 30 h of natural ageing of Al-6Zn-2.2Mg-2.3Cu.

Based on the shown equation, *vacancy induced hardness* values were then calculated as a function of the incubation period (Figure 5.20).

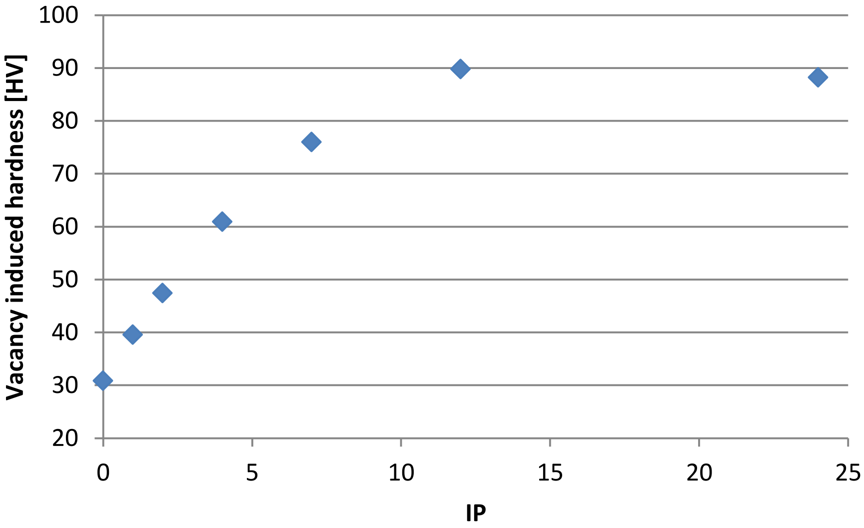

Figure 5.20: Calculated *vacancy induced hardness* values as a function of the incubation period in Al-6Zn-2.2Mg-2.3Cu.

Following, the initial hardening rate was calculated and the time required to reach the maximum hardness located, so that these quantities were eventually plotted as a function of the *vacancy induced hardness* (Figure 5.21, Figure 5.23).

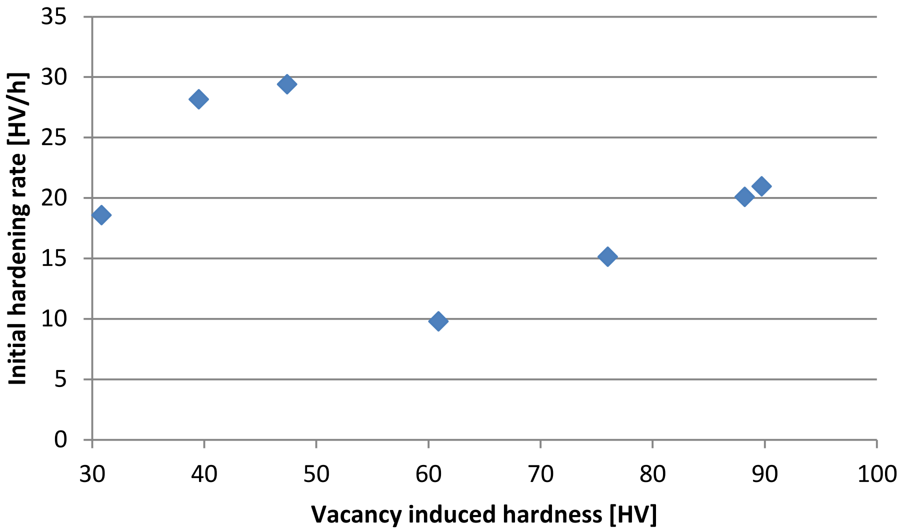

Figure 5.21: Initial hardening rate of Al-6Zn-2.2Mg-2.3Cu during artificial ageing as a function of *vacancy induced hardness*.

According to the image above, it would be easy to claim the aforementioned theory, about atoms mobility decreasing with increasing incubation period, is not true. Although, it should be reminded the hardening rate in Al-6Zn-2.2Mg-2.3Cu is strongly affected by parameters such as Cu content and Zn/Mg ratio, other than the depletion of vacancies. The presence of Cu indeed, by promoting the formation of small and densely dispersed precipitates and preventing the dissolution of forming clusters, results into high hardening rates. On the other side, the initial slope is influenced by Zn/Mg ratio to the extent that, since the hardening phenomenon is related to the growth of small precipitates by attraction of Zn atoms, a higher Zn content results into a faster growth. It is therefore likely both these parameters, which characterize Al-6Zn-2.2Mg-2.3Cu, overcome the effect of *vacancy induced hardness* on the hardening rate, so that a trend is not discernable in the above graph.

As proof of what just mentioned, it is interesting to notice how in Figure 5.21 initial hardening rate values are averagely higher than in Al-3.6Zn-1.8Mg.

Nevertheless, if the initial slope is considered in function of the incubation period only (Figure 5.22), the shown trend gains again significance, as it will be further discussed.

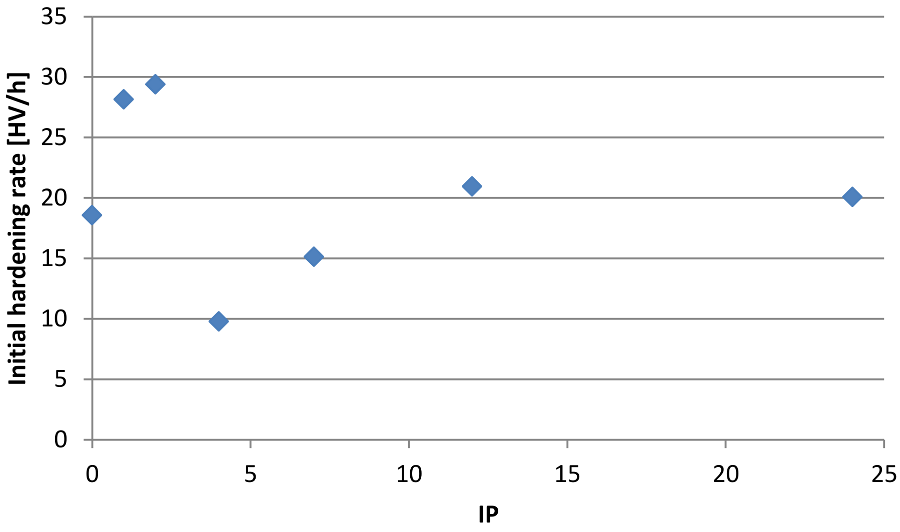

Figure 5.22: Initial hardening rate of Al-6Zn-2.2Mg-2.3Cu during artificial ageing as a function of the incubation period.

The influence of Cu and Zn/Mg ratio vanishes soon after the early stages of ageing, so that atoms mobility and *vacancy induced hardness* become again the predominant parameters affecting precipitates growth. Therefore *time to maximum* is characterized by an increasing trend with respect to *vacancy induced hardness*, since with fewer vacancies available, atoms diffuse slower, and *artificial ageing stable co-clusters* need more time to be formed.

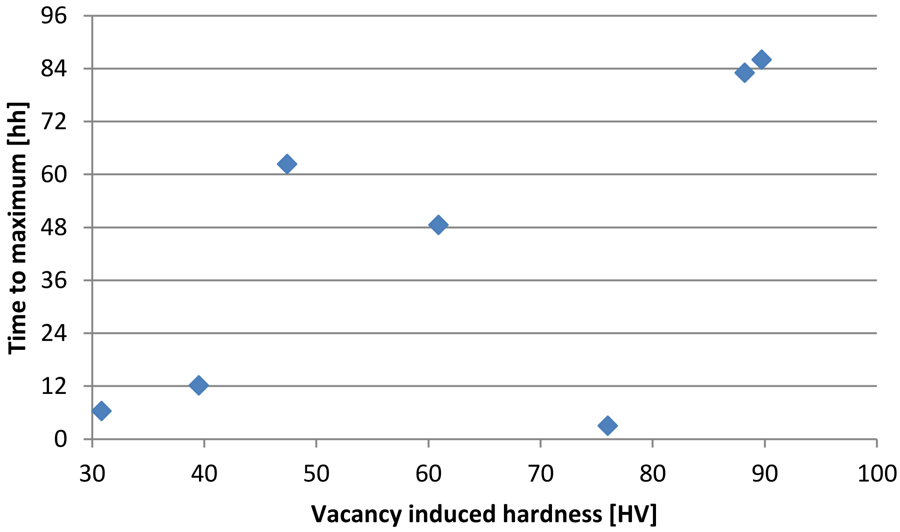

Figure 5.23: Artificial ageing time required to reach the maximum hardness as a function of *vacancy induced hardness*, in Al-6Zn-2.2Mg-2.3Cu.

Every single artificial ageing condition is now going to be analyzed in relationship to the formulated precipitation theory. For the sake of clarity, Figure 5.18 is proposed again underneath without natural ageing data (Figure 5.24).

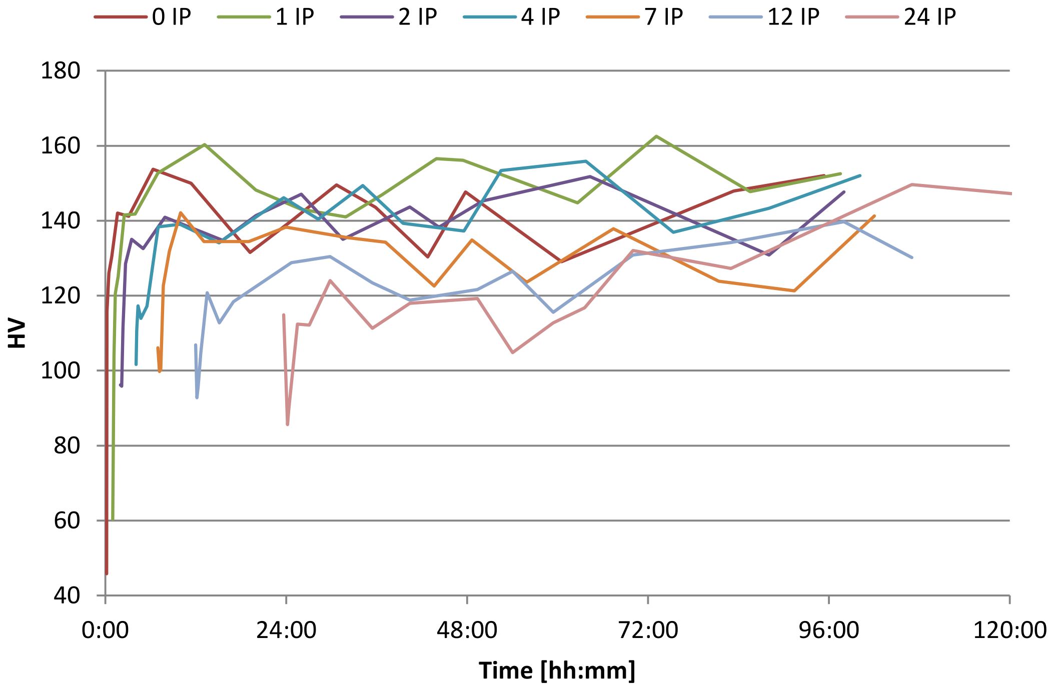

Figure 5.24: Microhardness evolution of Al-6Zn-2.2Mg-2.3Cu in the different artificial ageing conditions.

- 0 IP, unlike in Al-3.6Zn-1.8Mg, shows that the high Cu content and Zn/Mg ratio promote a constant hardness increase rate in early ageing, so that the curve reaches the peak hardness in a very short time.
- 1 IP lies in the middle of region *Ia* (Figure 5.9), where solute rich clusters are present in the microstructure. Then, when samples are artificially aged, the presence of these already formed clusters leads to a steeper initial slope of the curve than in the 0 IP condition (Figure 5.22). It is essential to stress that in Al-3.6Zn-1.8Mg 1 IP was characterized by a hardening rate lower than 0 IP but, again, in Al-6Zn-2.2Mg-2.3Cu the high Cu content and Zn/Mg ratio overcome the effect of a reduced atoms mobility, which, instead, becomes appreciable in the increase of the *time to maximum* figure.
- 2 IP curve, like in the Cu free alloy, is characterized by the presence of bigger solute rich clusters at the beginning of artificial ageing, which leads to an initial hardening

rate higher than in 1 IP. Instead, the increase with respect to 0 IP is again attributable to the Cu content and Zn/Mg ratio.

- 4 IP presents a drop in the hardening rate during early artificial ageing, since the effect of Cu is vanished after 4 hours of incubation period and vacancies depletion is no longer negligible.
- 7 IP, 12 IP and 24 IP curves are again characterized by the already mentioned dissolution of GPI zones, which causes a decrease in the microhardness with respect to natural ageing. Nevertheless, differently than in Al-3.6Zn-1.8Mg, the initial slope is higher in these curves than in the 4 IP condition, and almost the same for 12 IP and 24 IP; with the dissolution of GPI indeed, Cu and Zn atoms are released in the matrix and become newly available to speed up the hardening process. Although, as it was said before, their effect vanishes fast, and the lower atoms mobility leads to high *time to maximum* values. Exception is made for the 7 IP curve, where, as discussed in the Cu free alloy, the microstructural condition characteristic of the *co-clusters formation* stage results into an overall low hardness level, and therefore into a shorter *time to maximum*.

In conclusion, with the formulated precipitation theory it was possible to explain the observed artificial ageing behavior of Al-6Zn-2.2Mg-2.3Cu, thus proving once more its validity.

6. Conclusions and recommendations

In the present project, macrohardness and microhardness evolution analyses, during natural and artificial ageing, of CDS cast 7xxx series aluminum *wrought alloys* were carried out to formulate a valid precipitation theory.

- From the microhardness data obtained during natural ageing it was possible to recognize three main sequences in the T4 precipitation process: *clusters formation* stage, *co-clusters formation stage* and *co-clusters growth* stage.
    - *clusters formation* stage (0 to 5 hours of natural ageing): solute atoms diffuse in the metal matrix to form Mg rich clusters. Here, the hardness increase is related to the rising number of solute clusters and to the depletion of vacancies caused by atomic diffusion. In Al-6Zn-2.2Mg-2.3Cu the hardening rate, during the first 2 hours, is higher than in Al-3.6Zn-1.8Mg, since Cu atoms prevent clusters dissolution.
    - *co-clusters formation* stage (5 to 10 hours of natural ageing): Zn atoms slowly join Mg rich clusters to form early co-clusters, characterized by a Zn/Mg ratio lower than 1. The observed slow hardening rate is the consequence of the co-clusters size increasing and of the continuous vacancy depletion.
    - *co-clusters growth* stage (after 10 hours of natural ageing): newly formed GPI zones grow in size by attracting Zn atoms, until Zn/Mg reaches 1.
- Two matrix regions were identified through the analysis of microhardness data obtained during natural ageing; regions with precipitates or without precipitates. The former lead to hardness values that were addressed as *precipitates induced hardness*, while the latter generate those values referred as *vacancy induced hardness*.
- Macrohardness data clearly showed how a higher solute content leads to a higher hardness level and to a lower hardening response. Besides, they provided useful information on how the presence of Cu and a high Zn/Mg ratio are essential factors for the promotion of a rapid hardness increase during early ageing.
- In artificial ageing, microhardness evolution was characterized by an initial steep increase, related to the formation of intermediate precipitates (probably elongated

GPI), followed by a knee, where just evolved artificial ageing co-clusters grow in size, and a flat region, where *artificial ageing stable co-clusters* are present.

- Macrohardness data pointed out how the overaged condition was not reached in 4 days of holding at 120 °C, which may induce to believe that stable η precipitates did not nucleate inside the microstructure and only η' and GPI were present.
- The time spent at room temperature between quenching and the beginning of artificial ageing highly influences the hardness evolution of the material. More precisely, the longer the incubation period, the fewer the remaining vacancies for atoms diffusion and the longer precipitates take to form. On the other side, early ageing hardening rate is affected by factors like incubation period, Cu content and Zn/Mg ratio, with long incubation periods leading to low hardness increase rates, unless the rapid hardening effect of the other two parameters takes over.
- Based on the best initial slope of the curves and on the shortest time required to reach the peak hardness, it is advisable to let samples rest at room temperature before artificial ageing is begun. For Al-6Zn-2.2Mg-2.3Cu the suggestion is to adopt an incubation period of 1 h, while 2 h seem optimal for Al-3.6Zn-1.8Mg.
- To clearly define the type of precipitates characterizing the matrix, further microscopical and chemical analyses should be carried out.

In conclusion, it is possible to claim a valid precipitation theory was formulated to explain microstructural evolutions of CDS cast Al-6Zn-2.2Mg-2.3Cu and Al-3.6Zn-1.8Mg during T4 and T6 heat treatments.

7. References

[1] Vox, "What are US fuel-efficiency standards for cars and trucks?," [Online]. Available: http://www.vox.com/cards/obama-climate-plan/what-are-u-s-fuel-efficiency-standards-for-cars-and-trucks. [Accessed 12 06 2014].

[2] M. Johannaber, M. Espig, R. Wohlecker, H. Wallentowitz. and J. Leyers, "Determination of Weight Elasticity of Fuel Economy for Conventional ICE Vehicles, Hybrid Vehicles and Fuel Cell Vehicles," FORSCHUNGSGESELLSCHAFT KRAFTFAHRWESEN mbH AACHEN, Aachen, 2007.

[3] L. Sobrino, *Caratterizzazione meccanica di lamiere per uso autoveicolistico tramite tecniche non convenzionali,* Torino: Politecnico di Torino, 2012.

[4] P. Li, B. Xiong, Y. Zhang and Z. Li, "Temperature variation and solution treatment of high strength AA 7050," *Trans. Nonferrous Met. Soc. China,* vol. 22, pp. 546-554, 2012.

[5] J. Zhang, Y. Deng, W. Yang, S. Hu and X. Zhang, "Design of the multi-stage quenching process for 7050 aluminum alloy," *Materials and Design,* vol. 56, pp. 334-344, 2013.

[6] K. Symeonidis, *The Controlled Diffusion Solidification Process: Fundamentals and Principles,* Worcester Polytechnic Institute, 2009.

[7] S. Shankar, D. Saha, D. Apelian and M. M. Makhlouf, "Casting of Aluminum-Based Wrought Alloys Using Controlled Diffusion Solidification," *Metallurgical and Materials Transactions A,* vol. 35 A, pp. 2174-2180, 2004.

[8] D. Apelian, M. Makhlouf and D. Saha, "CDS Method for Casting Aluminum-Based Wrought Alloy Compositions: theoretical framework," *Materials Science Forum,* Vols. 519-521, pp. 1771-1776, 2006.

[9] R. Ghiaasiaan, X. Zeng and S. Shankar, "Controlled Diffusion Solidification (CDS) of Al-Zn-Mg-Cu (7050): Microstructure, heat treatment and mechanical properties," *Materials Science & Engineering A,* vol. 594 A, pp. 260-277, 2014.

[10] J. Tang, H. Chen, X. Zhang, S. Liu, W. Liu, H. Ouyang and H. Li, "Influence of quench-induced precipitation on aging behavior of Al-Zn-Mg-Cu alloys," *Trans. Nonferrous Met. Soc. China,* vol. 22, pp. 1255-1263, 2012.

[11] J. Manickaraj, G. Liu and S. Shankar, "Effect of incubation coupled with artificial aging in T6 heat treatment of A356.2 aluminum casting alloy," *International Journal of Metalcasting ,* pp. 17-36, 2011.

[12] A. Khalaf, P. Ashtari and S. Sumanth, "Formation of Nondendritic Primary Aluminum Phase in Hypoeutectic Alloys in Controlled Diffusion Solidification (CDS): A Hypothesis," *Metallurgical and Materials Transactions B,* vol. 40 B, pp. 843-849, 2009.

[13] A. Khalaf and S. Shankar, "Favorable Environment for a Nondendritic Morphology in Controlled Diffusion Solidification," *Metallurgical and Materials Transactions A,* vol. 42 A, pp. 2456-2465, 2011.

[14] S. Liu, Q. Zhong, Y. Zhang, W. Liu, X. Zhang and Y. Deng, "Investigation of quench sensitivity of high strength Al-Zn-Mg-Cu alloys by time-temperature-properties diagrams," *Materials and Design ,* vol. 31, pp. 3116-3120, 2010.

[15] M. Gwozdz and K. Kwapisz, *Influence of ageing process on the microstructure and mechanical properties of aluminium-silicon cast alloys - Al-9%Si-3%Cu and Al-9%Si-0.4%Mg,* Jonkoping University, 2008.

[16] J. Samei and D. Green , *lecture slides from "Characterization Techniques in Metal Forming",* University of Windsor, 2013.

[17] E. Sjolander and S. Seifeddine, "The heat treatment of Al-Si-Cu-Mg casting alloys," *Journal of Materials Processing Technology,* vol. 210, pp. 1249-1259, 2010.

[18] "http://www.spaceflight.esa.int/," European Space Agency. [Online]. [Accessed 27 3 2014].

[19] A. Mohamed and F. Samuel, "A Review on the Heat Treatment of Al-Si-Cu/Mg Casting Alloys," in *Metallurgy - Advances in Materials and Processes*, InTech, 2012.

[20] W. D. Callister, Materials Science and Engineering: an Introduction, John Wiley & Sons, 2007.

[21] N. Han, X. Zhang, S. Liu, D. He and R. Zhang, "Effect of solution treatment on the strength and fracture toughness of aluminum alloy 7050," *Journal of Alloys and Compounds,* vol. 509, pp. 4138-4145, 2011.

[22] K. Chen, H. Liu, Z. Zhang, S. Li and R. Todd, "The improvement of constituent dissolution and mechanical properties of 7055 aluminum alloys by stepped heat

treatments," *Journal of Materials Processing Technology ,* vol. 142, pp. 190-196, 2003.

[23] A. Mohamed, F. Samuel and S. Al kahtani, "Influence of Mg and solution heat treatment on the occurence of incipient melting in Al-Si-Cu-Mg cast alloys," *Materials Science and Engineering A,* vol. 543 A , pp. 22-34, 2012.

[24] A. Samuel, H. Doty, S. Valtierra and F. Samuel, "Defects related to incipient melting in Al-Si-Cu-Mg alloys," *Materials and Design,* vol. 52, pp. 947-956, 2013.

[25] P. Lang, T. Wojcik, E. Povoden-Karadeniz, A. Falahati and E. Kozeschnik, "Thermo-kinetic prediction of metastable and stable phase precipitation in Al-Zn-Mg series aluminum alloys during non-isothermal DSC analysis," *Journal of Alloys and Compounds,* 2014.

[26] M. Ibrahim, A. Samuel and F. Samuel, "A preliminary study on optimizing the heat treatment of high strength Al-Cu-Mg-Zn alloys," *Materials and Design ,* vol. 57, pp. 342-350, 2014.

[27] X. Chen, W. Kasprzak and J. Sokolowski, "Reduction of the heat treatment process for Al-based alloys by utilization of heat from the solidification process," *Journal of Materials Processing Technology,* vol. 176, pp. 24-31, 2006.

[28] D. Xu, P. Rometsch and N. Birbilis, "Improved solution treatment for an as-rolled Al-Zn-Mg-Cu alloy. Part I. Characterization of constituent particles and overheating," *Materials Science and Engineering,* vol. A, pp. 234-243, 2012.

[29] J. Sokolowski, X.-C. Sun, G. Byczynski, D. Northwood, D. Penrod, R. Thomas and A. Esseline, "The removal of copper-phase segregation and the subsequent improvement in mechanical properties of cast 319 aluminum alloys by a two-stage solution heat treatment," *Journal of Materials Processing Technology,* vol. 53, pp. 385-392, 1995.

[30] J. H. Sokolowski, M. B. Djurdjevic, C. A. Kierkus and D. O. Northwood, "Improvement of 319 aluminum alloy casting durability by high temperature solution treatment," *Journal of Materials Processing Technology,* vol. 109, pp. 174-180, 2001.

[31] D. Hall and I. Mudawar, "Optimization of quench history of aluminum parts for superior mechanical properties," *Int. J. Heat Mass Transfer,* vol. 39, pp. 81-95, 1996.

[32] G. Sha and A. Cerezo, "Early-stage precipitation in Al-Zn-Mg-Cu alloy (7050)," *Acta Materialia,* vol. 52, pp. 4503-4516, 2004.

[33] Y. Liu, D. Jiang, B. Li, W. Yang and J. Hu, "Effect of cooling aging on microstructure and mechanical properties of an Al-Zn-Mg-Cu alloy," *Materials and Design ,* vol. 57, pp. 79-86, 2014.

[34] P. Archambault and D. Godard, "High temperature precipitation kinetics and TTT curve of a 7xxx alloy by in-situ electrical resistivity measurements and differential calorimetry," *Scripta Materialia,* vol. 42, pp. 675-680, 2000.

[35] J. Buha, R. Lumley and A. Crosky, "Secondary ageing in an aluminum alloy 7050," *Materials Science and Engineering,* vol. 492, pp. 1-10, 2008.

[36] S. Liu, X. Zhang, M. Chen and J. You, "Influence of aging on quench sensitivity effect of 7055 aluminum alloy," *Materials Characterization,* vol. 59, pp. 53-60, 2008.

[37] L. Berg, J. Gjonnes, V. Hansen, X. Li, M. Knutson-Wedel, G. Waterloo, D. Schryvers and L. Wallenberg, "GP-zones in Al-Zn-Mg alloys and their role in artificial aging," *Acta Materialia,* vol. 49, pp. 3443-3451, 2001.

[38] L. Wu, M. Seyring, M. Rettenmayr and W. Wang, "Characterization of precipitate evolution in an artificially aged Al-Zn-Mg-Sc-Zr alloy," *Materials Science and Engineering,* vol. A, pp. 1068-1073, 2010.

[39] Ecole Polytechnique Federale de Lausanne, "Interdisciplinary centre for electron microscopy," [Online]. Available: http://cime.epfl.ch/page-26783.html. [Accessed 31 7 2014].

[40] The National Institute of Standards and Technology, "3D Atom Probe Tomography," [Online]. Available: http://www.nist.gov/mml/mmsd/microanalysis/atom-probe.cfm. [Accessed 31 7 2014].

[41] M. Gasko and G. Rosenberg, "Correlation between hardness and tensile properties in ultra-high strength dual phase steels-short communication," *Materials Engineering,* vol. 18, pp. 155-159, 2011.

[42] Wilson Instruments, "Fundamentals of Rockwell Hardness Testing," [Online]. Available: www.instron.com. [Accessed 28 5 2014].

[43] "Tendre ou Dure," Boulipedia, [Online]. Available: http://www.boulipedia.com/tendre-ou-dure. [Accessed 21 6 2014].

[44] "Vickers indentation using CSM's Micro Scratch Tester (MST)," CSM instruments,

[Online]. Available: http://www.csm-instruments.com/Vickers-indentation-using-CSMs-Micro-Scratch-Tester. [Accessed 22 6 2014].

[45] Buehler, "Operating and maintenance instructions," in *Micromet II microhardness testers*, Lake Bluff, 1984.

[46] "Elements, Atomic Radii and the Periodic Table," Crystalmaker Software Ltd. , [Online]. Available: http://crystalmaker.com/support/tutorials/crystalmaker/atomic-radii/index.html. [Accessed 20 07 2014].

[47] TransportPolicy.net, "US: Vehicle definitions," [Online]. Available: http://transportpolicy.net/index.php?title=US:_Vehicle_Definitions. [Accessed 7 8 2014].

8. Appendices

8.1 Appendix A

In this section the macrohardness evolution observed in each artificial ageing condition is reported individually. Graphs are shown according to increasing incubation periods and Al-3.6Zn-1.8Mg is presented first.

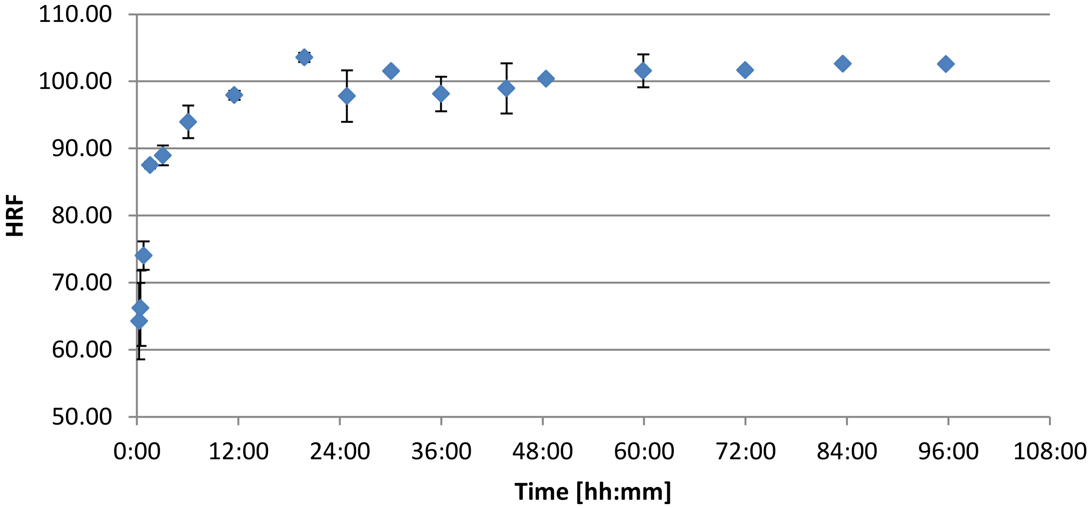

Figure 8.1: Macrohardness evolution of Al-3.6Zn-1.8Mg during artificial ageing, after 0 h of incubation period.

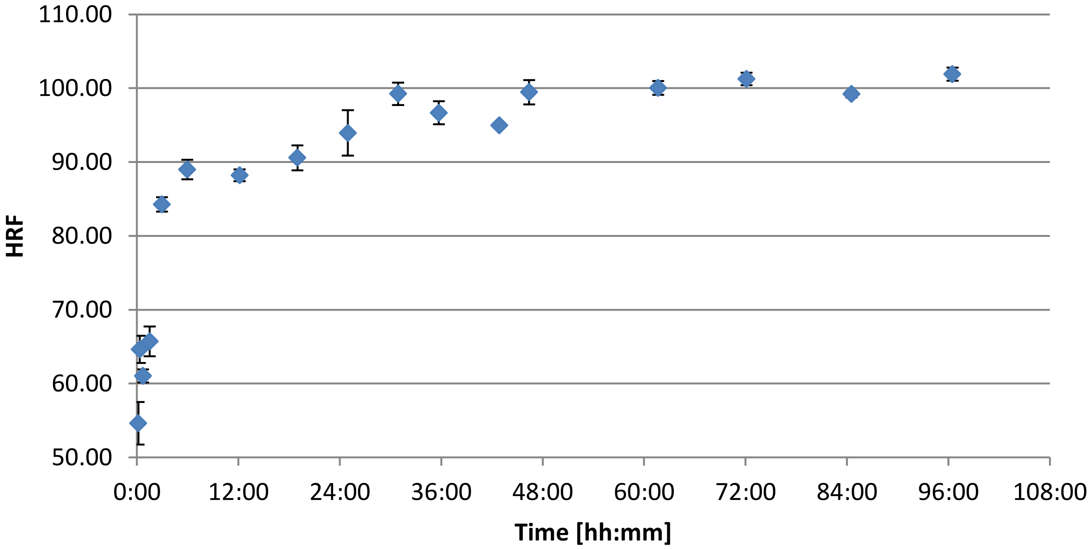

Figure 8.2: Macrohardness evolution of Al-3.6Zn-1.8Mg during artificial ageing, after 1 h of incubation period.

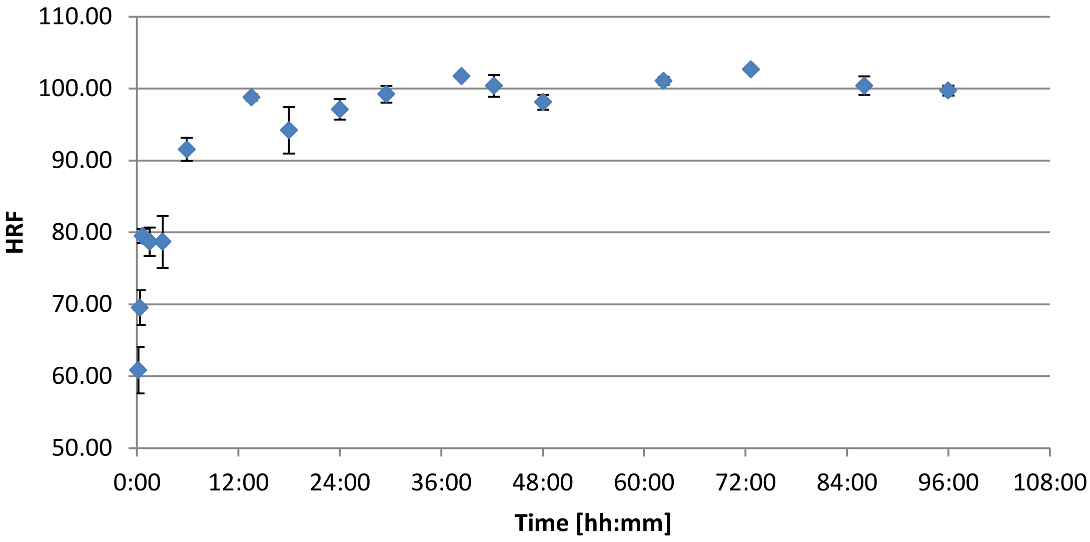

Figure 8.3: Macrohardness evolution of Al-3.6Zn-1.8Mg during artificial ageing, after 2 h of incubation period.

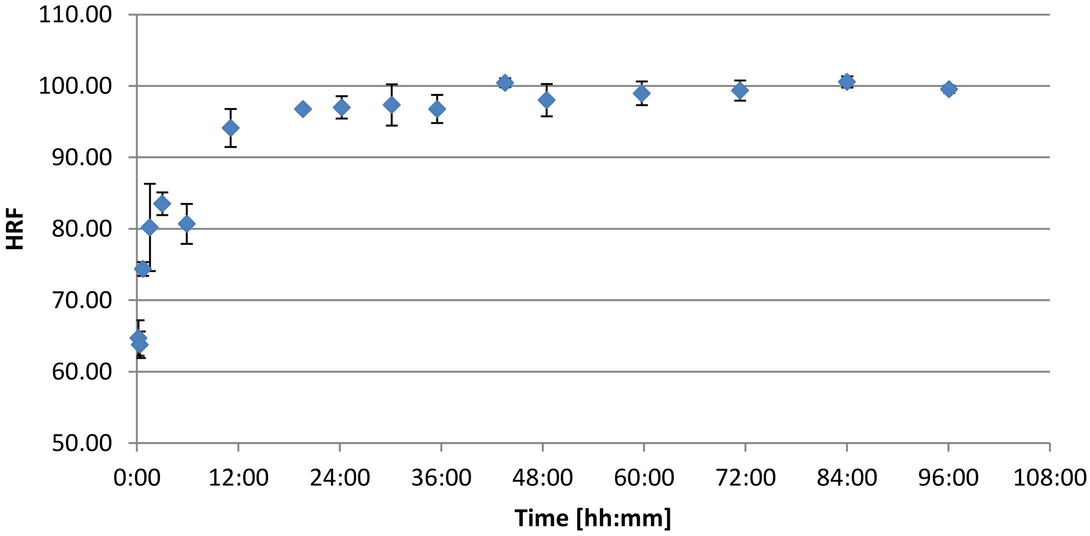

Figure 8.4: Macrohardness evolution of Al-3.6Zn-1.8Mg during artificial ageing, after 4 h of incubation period.

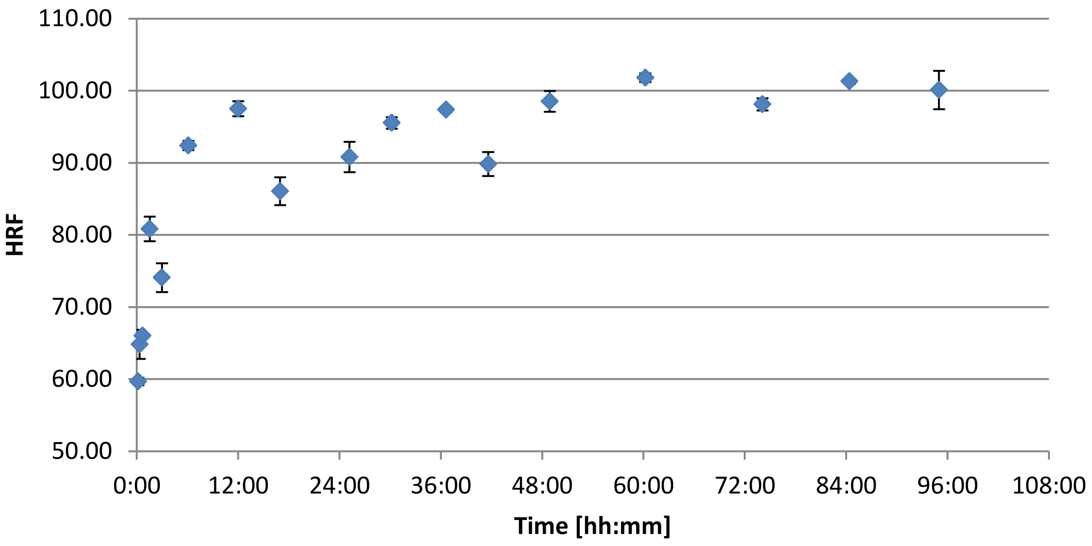

Figure 8.5: Macrohardness evolution of Al-3.6Zn-1.8Mg during artificial ageing, after 7 h of incubation period.

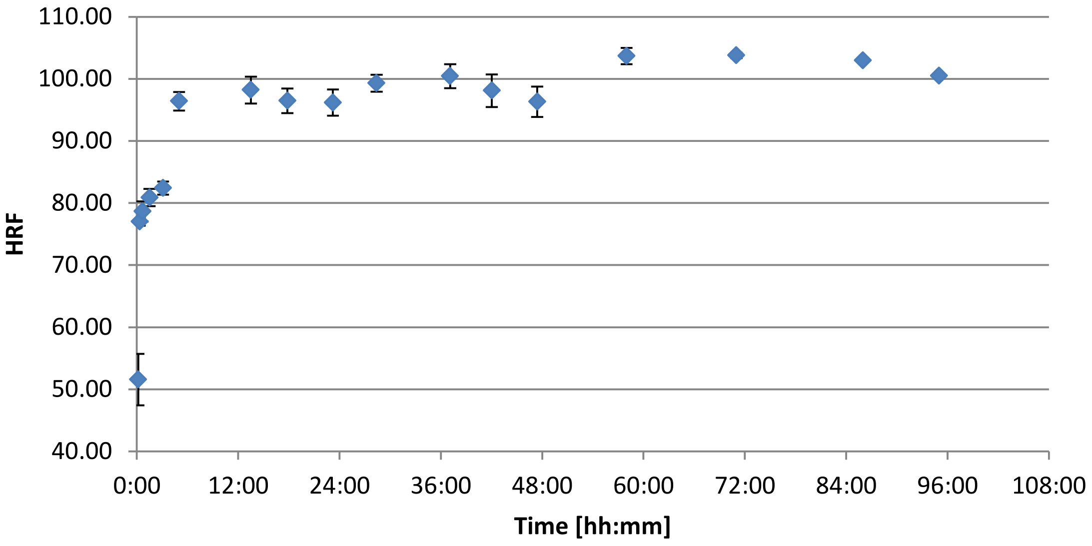

Figure 8.6: Macrohardness evolution of Al-3.6Zn-1.8Mg during artificial ageing, after 12 h of incubation period.

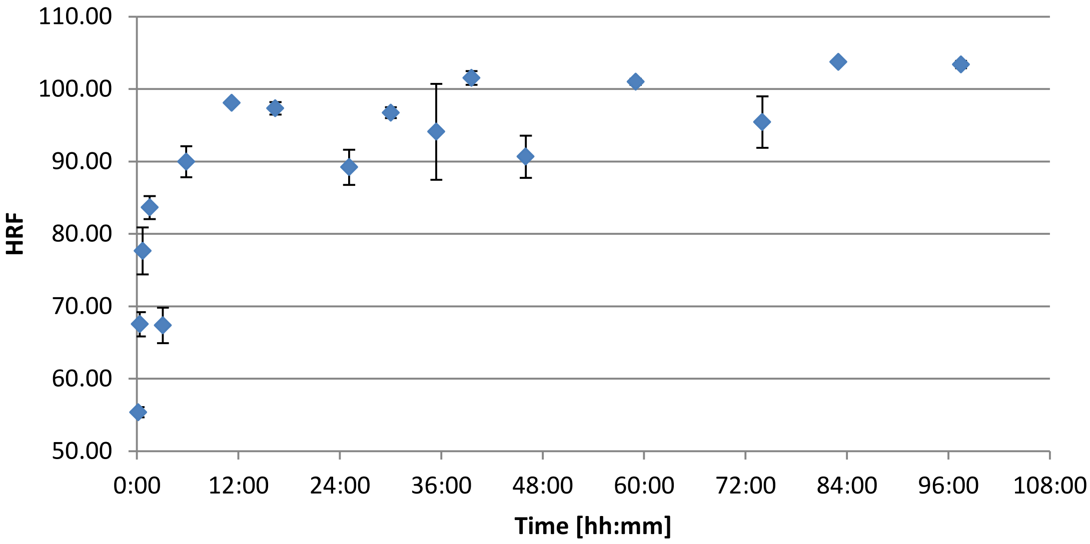

Figure 8.7: Macrohardness evolution of Al-3.6Zn-1.8Mg during artificial ageing, after 24 h of incubation period.

The following graphs refer to Al-6Zn-2.2Mg-2.3Cu.

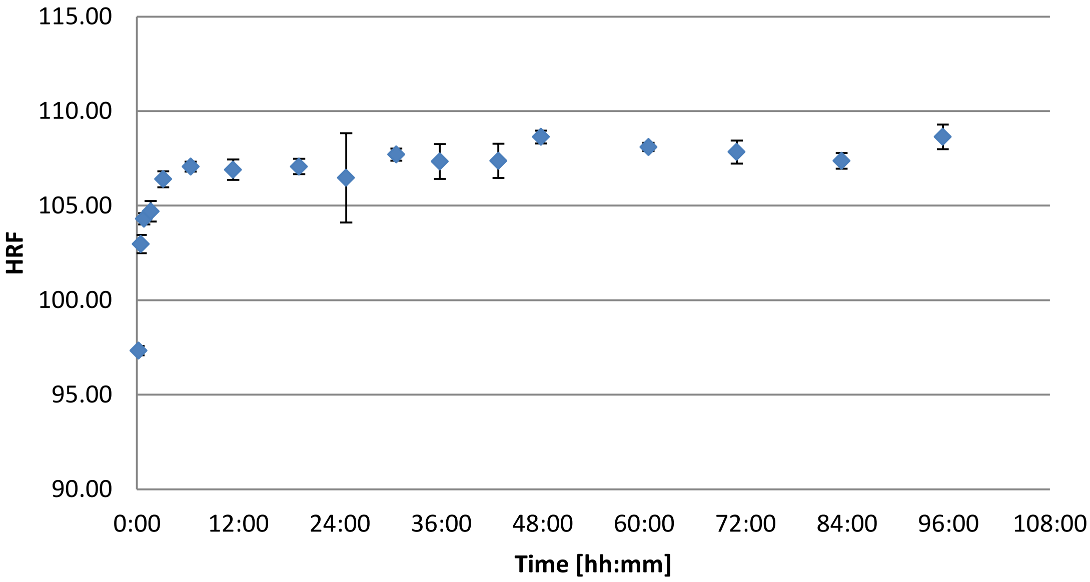

Figure 8.8: Macrohardness evolution of Al-6Zn-2.2Mg-2.3Cu during artificial ageing, after 0 h of incubation period.

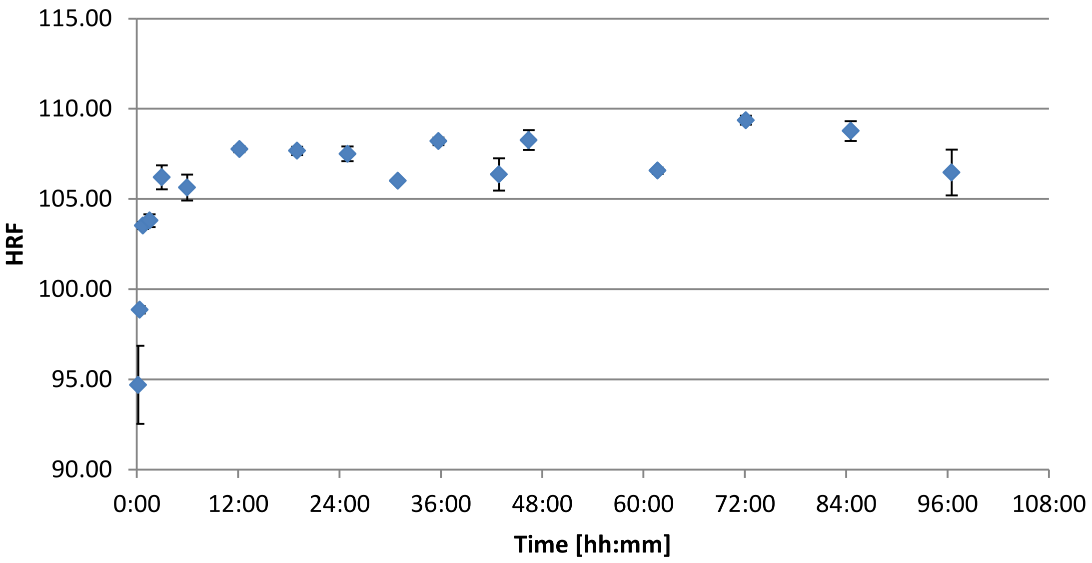

Figure 8.9: Macrohardness evolution of Al-6Zn-2.2Mg-2.3Cu during artificial ageing, after 1 h of incubation period.

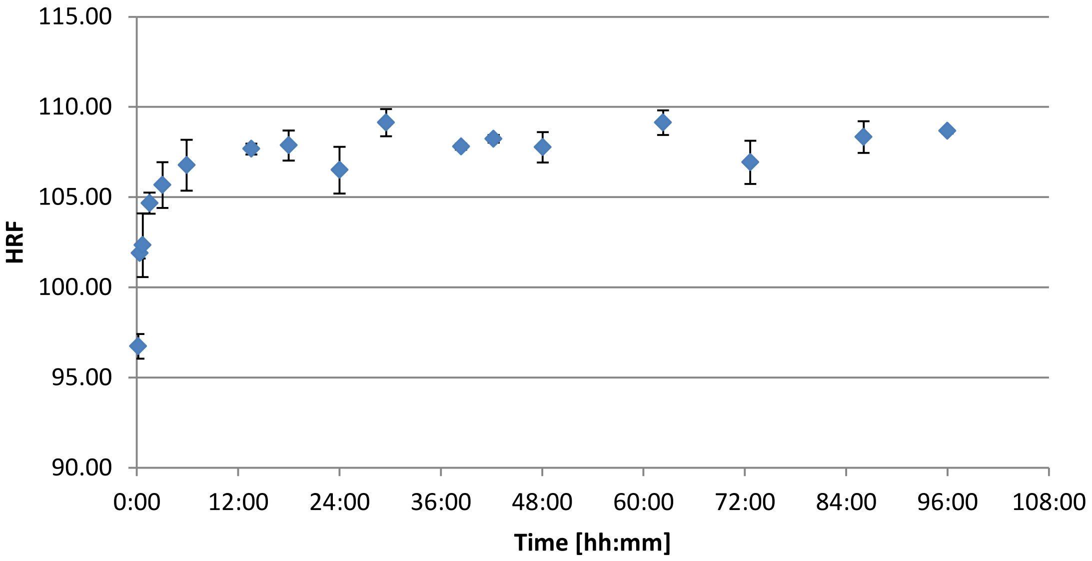

Figure 8.10: Macrohardness evolution of Al-6Zn-2.2Mg-2.3Cu during artificial ageing, after 2 h of incubation period.

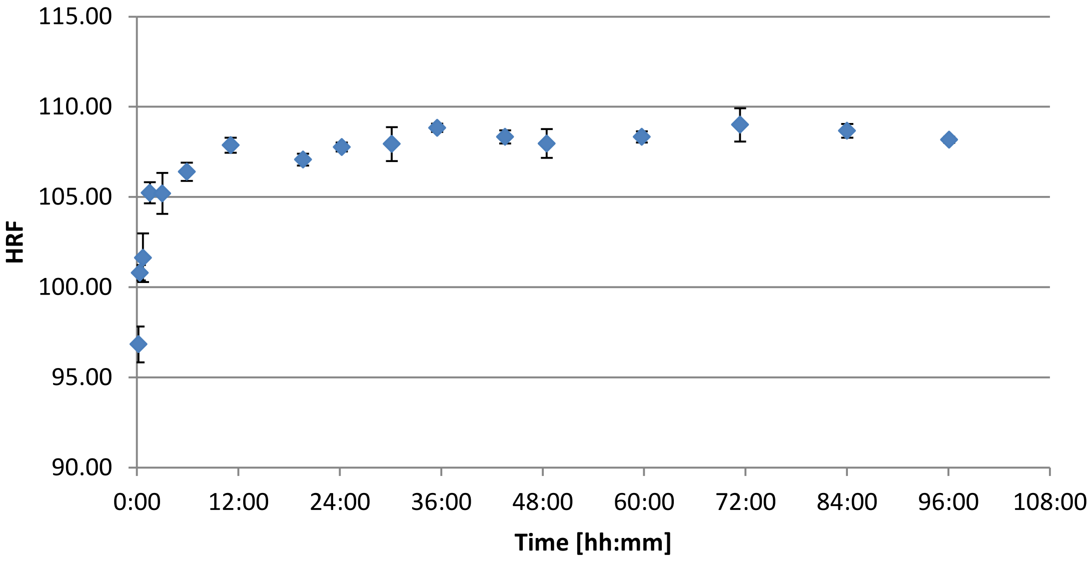

Figure 8.11: Macrohardness evolution of Al-6Zn-2.2Mg-2.3Cu during artificial ageing, after 4 h of incubation period.

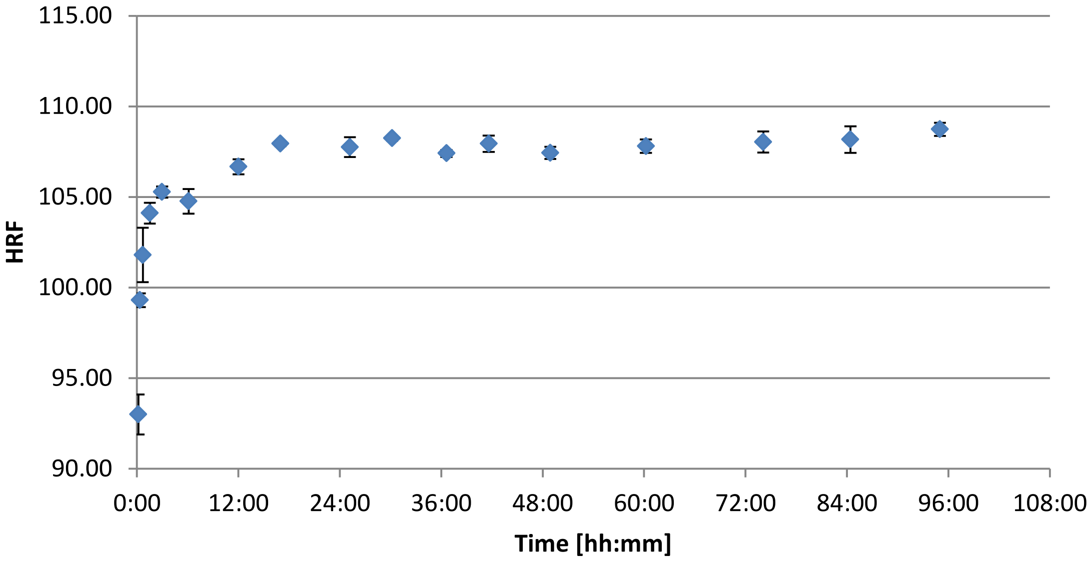

Figure 8.12: Macrohardness evolution of Al-6Zn-2.2Mg-2.3Cu during artificial ageing, after 7 h of incubation period.

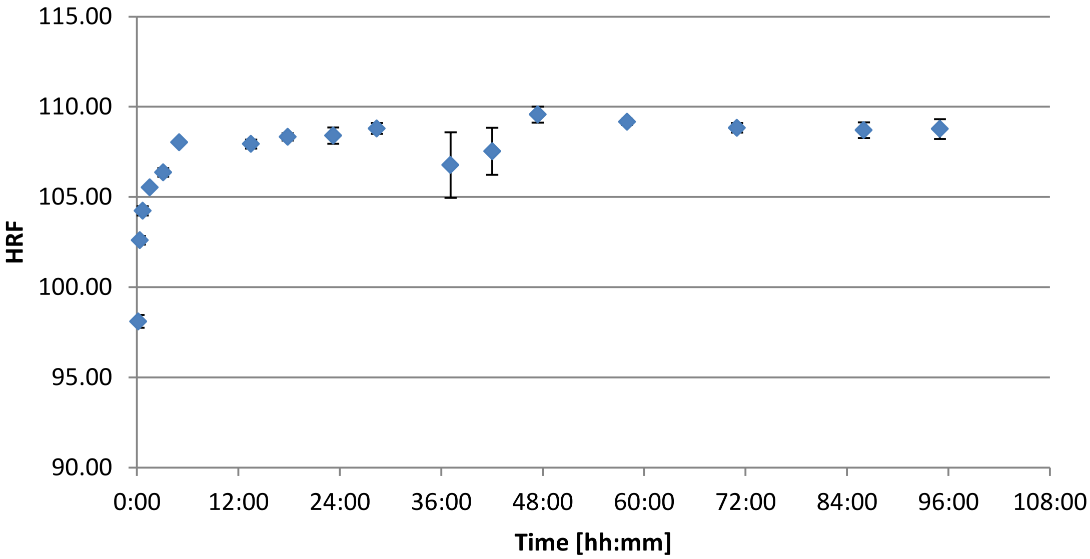

Figure 8.13: Macrohardness evolution of Al-6Zn-2.2Mg-2.3Cu during artificial ageing, after 12 h of incubation period.

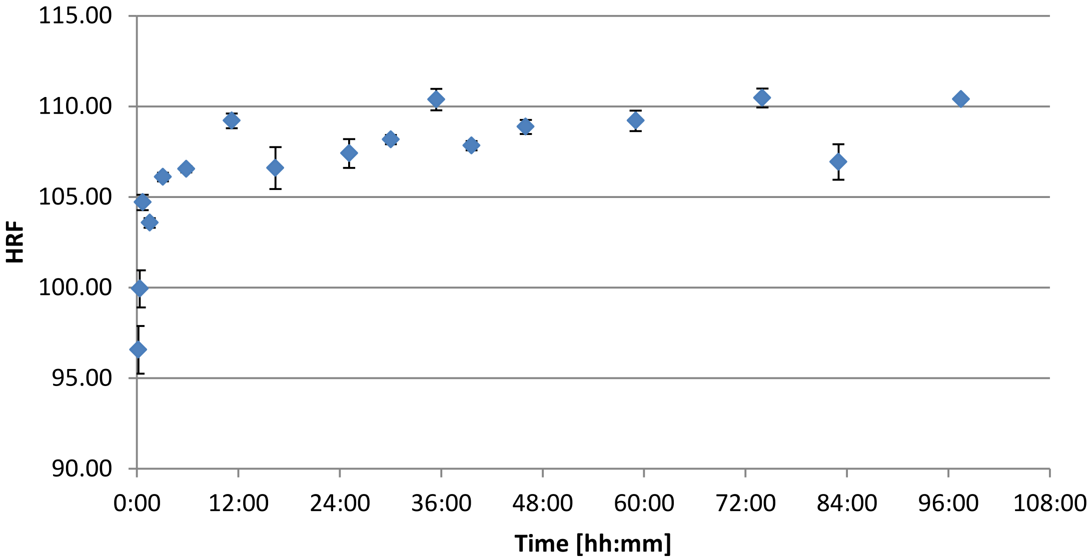

Figure 8.14: Macrohardness evolution of Al-6Zn-2.2Mg-2.3Cu during artificial ageing, after 24 h of incubation period.

8.2 Appendix B

In this section the microhardness evolution observed in each artificial ageing condition is reported individually. Graphs are shown according to increasing incubation periods and Al-3.6Zn-1.8Mg is presented first.

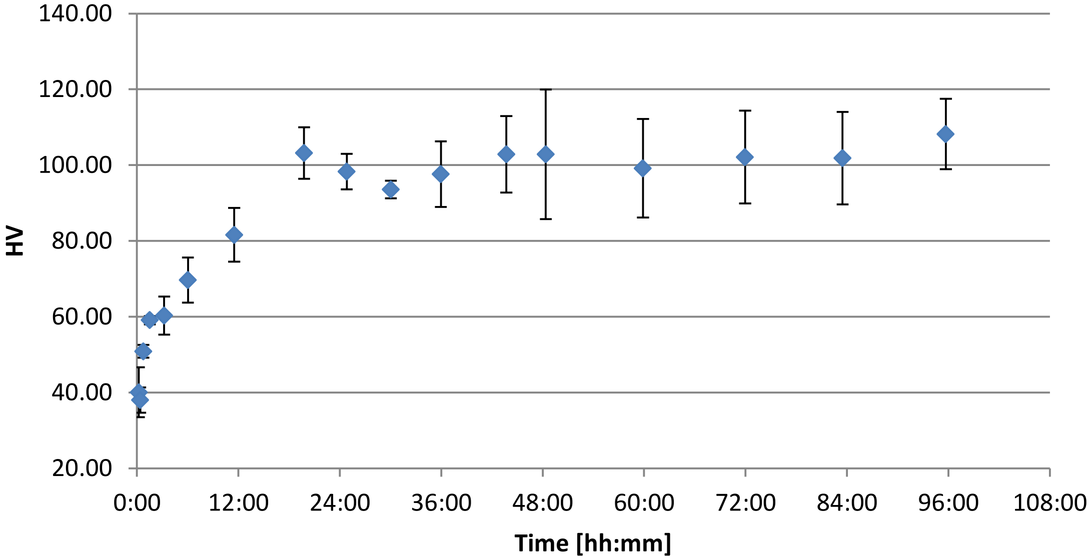

Figure 8.15: Microhardness evolution of Al-3.6Zn-1.8Mg during artificial ageing, after 0 h of incubation period.

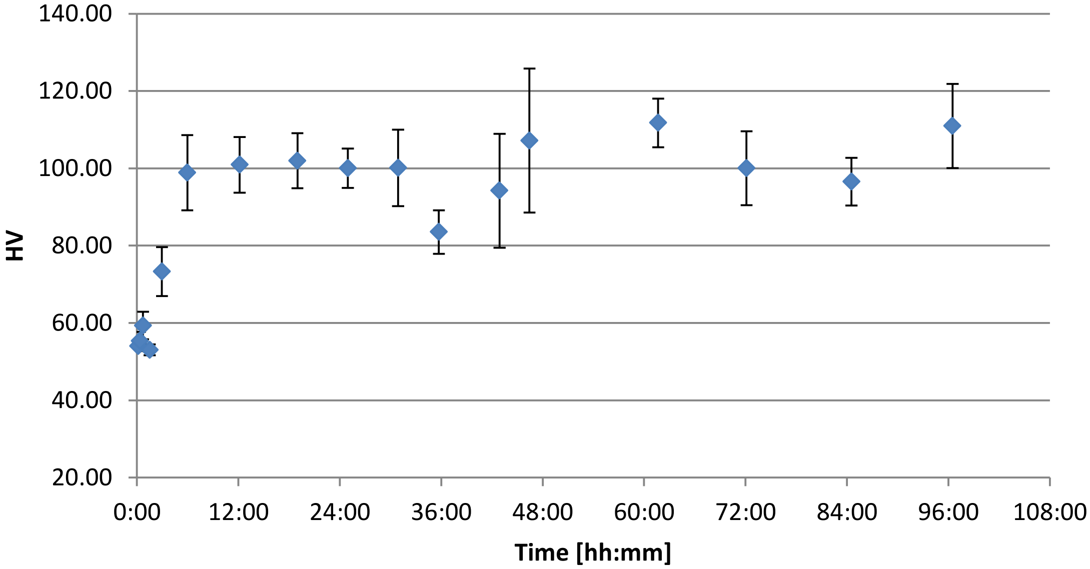

Figure 8.16: Microhardness evolution of Al-3.6Zn-1.8Mg during artificial ageing, after 1 h of incubation period.

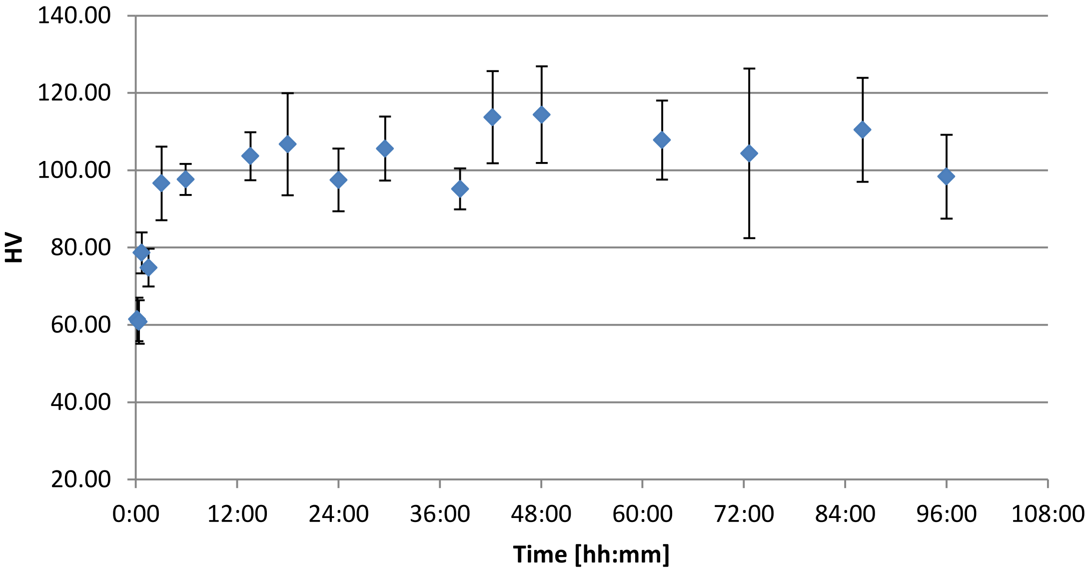

Figure 8.17: Microhardness evolution of Al-3.6Zn-1.8Mg during artificial ageing, after 2 h of incubation period.

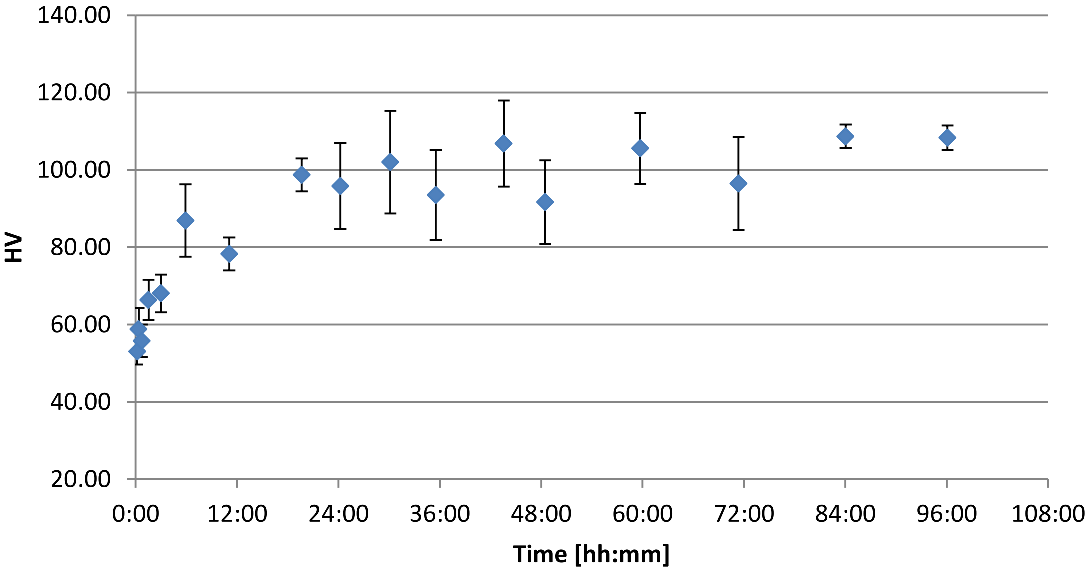

Figure 8.18: Microhardness evolution of Al-3.6Zn-1.8Mg during artificial ageing, after 4 h of incubation period.

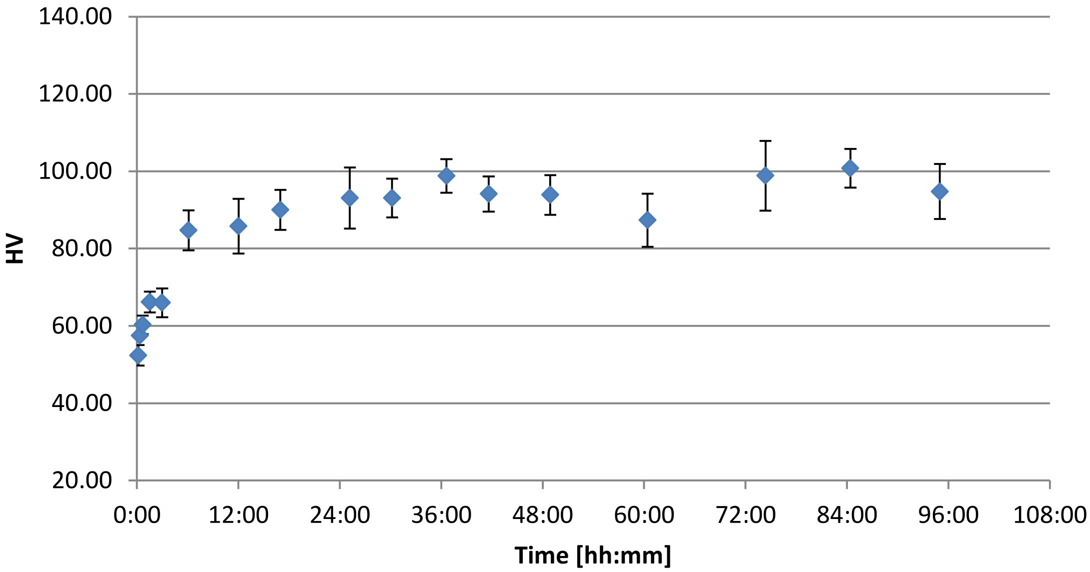

Figure 8.19: Microhardness evolution of Al-3.6Zn-1.8Mg during artificial ageing, after 7 h of incubation period.

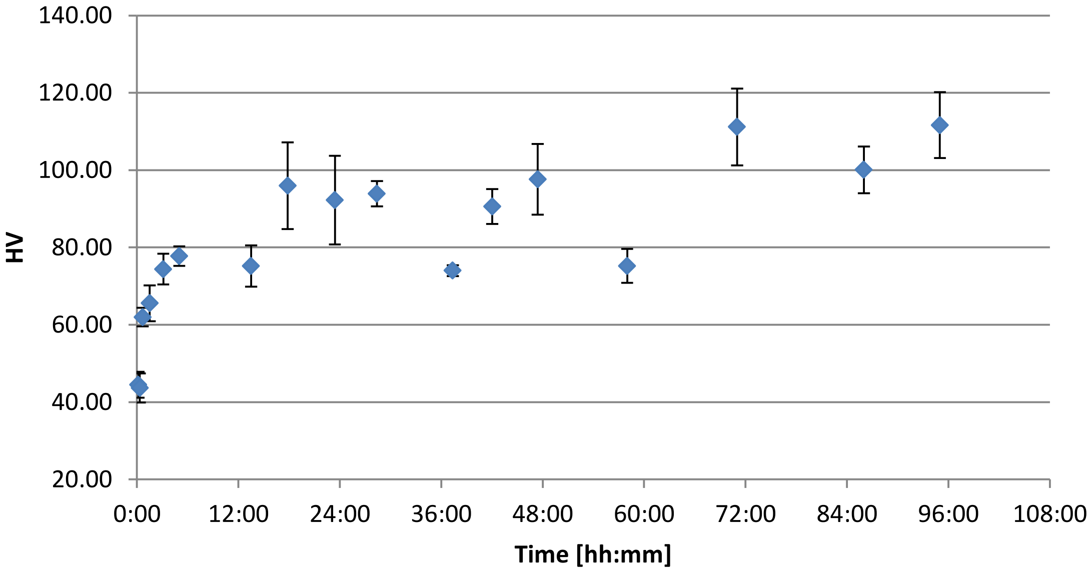

Figure 8.20: Microhardness evolution of Al-3.6Zn-1.8Mg during artificial ageing, after 12 h of incubation period.

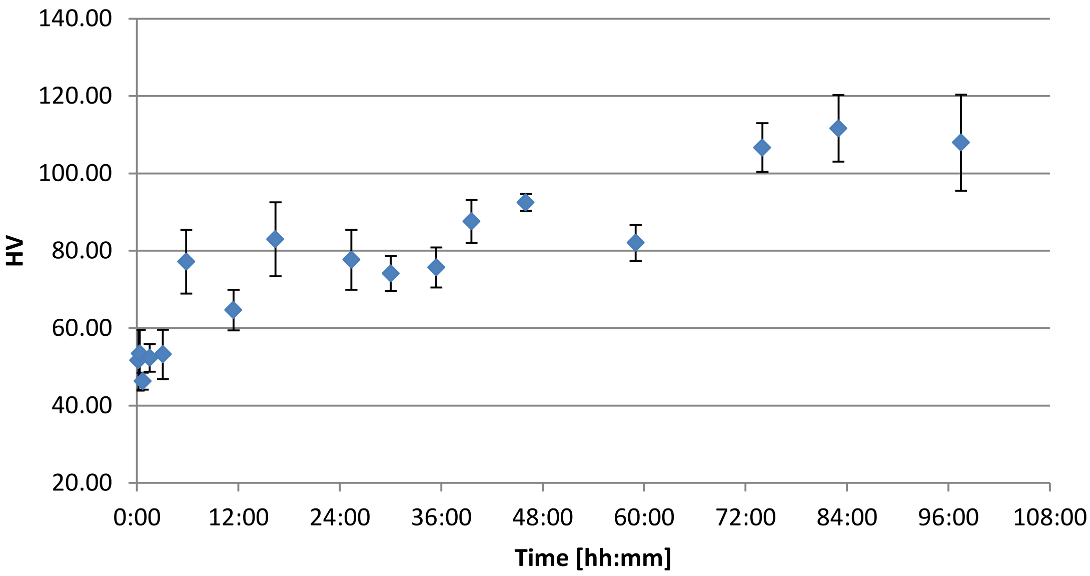

Figure 8.21: Microhardness evolution of Al-3.6Zn-1.8Mg during artificial ageing, after 24 h of incubation period.

The following graphs refer to Al-6Zn-2.2Mg-2.3Cu.

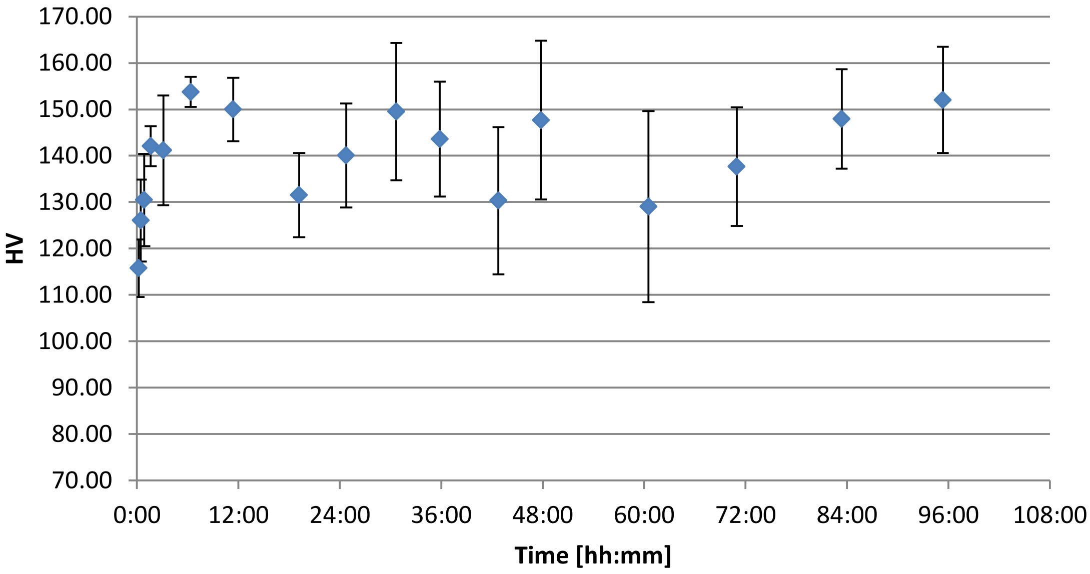

Figure 8.22: Microhardness evolution of Al-6Zn-2.2Mg-2.3Cu during artificial ageing, after 0 h of incubation period.

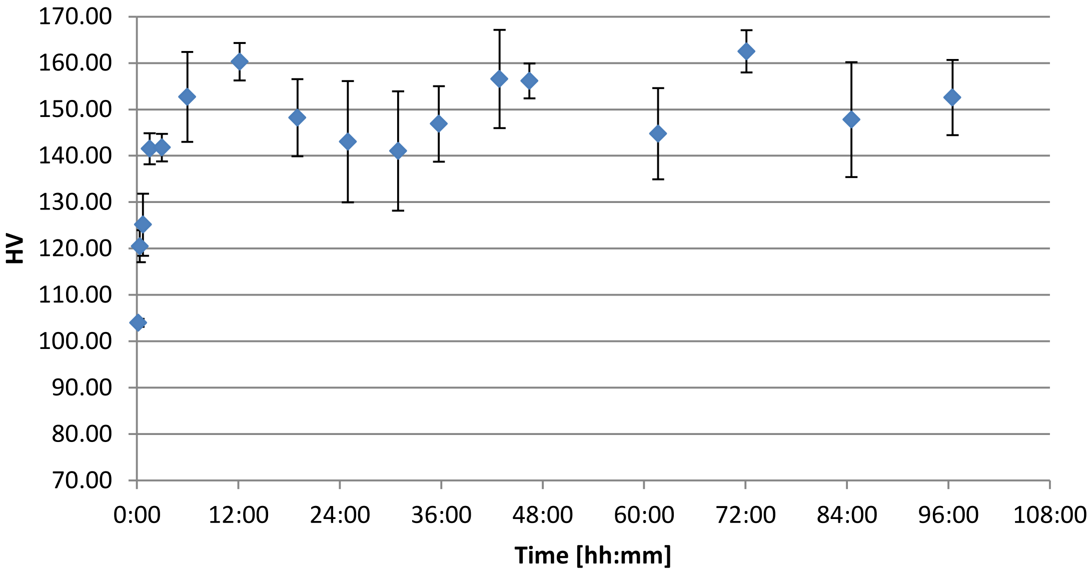

Figure 8.23: Microhardness evolution of Al-6Zn-2.2Mg-2.3Cu during artificial ageing, after 1 h of incubation period.

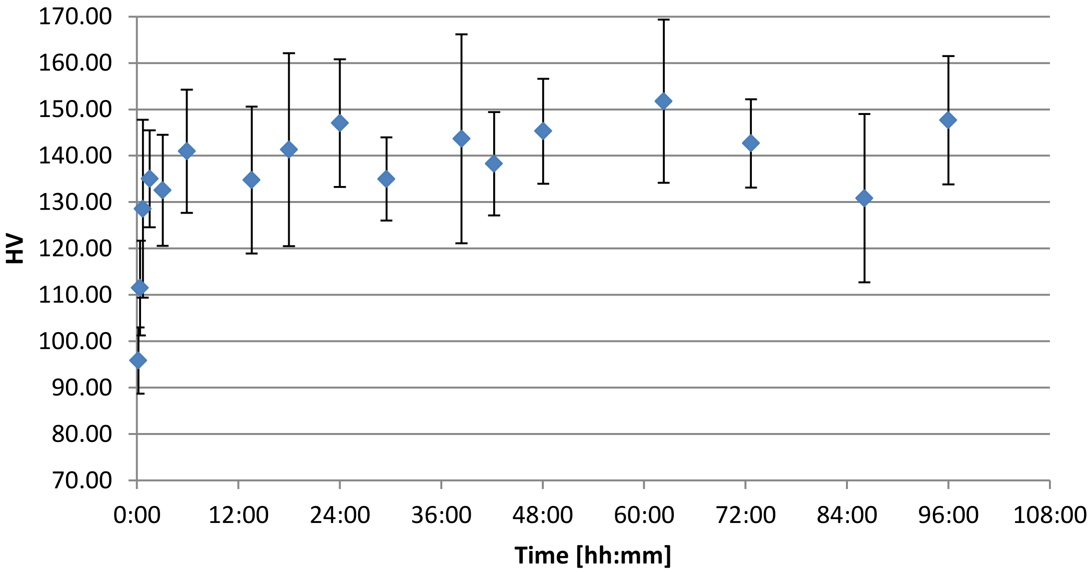

Figure 8.24: Microhardness evolution of Al-6Zn-2.2Mg-2.3Cu during artificial ageing, after 2 h of incubation period.

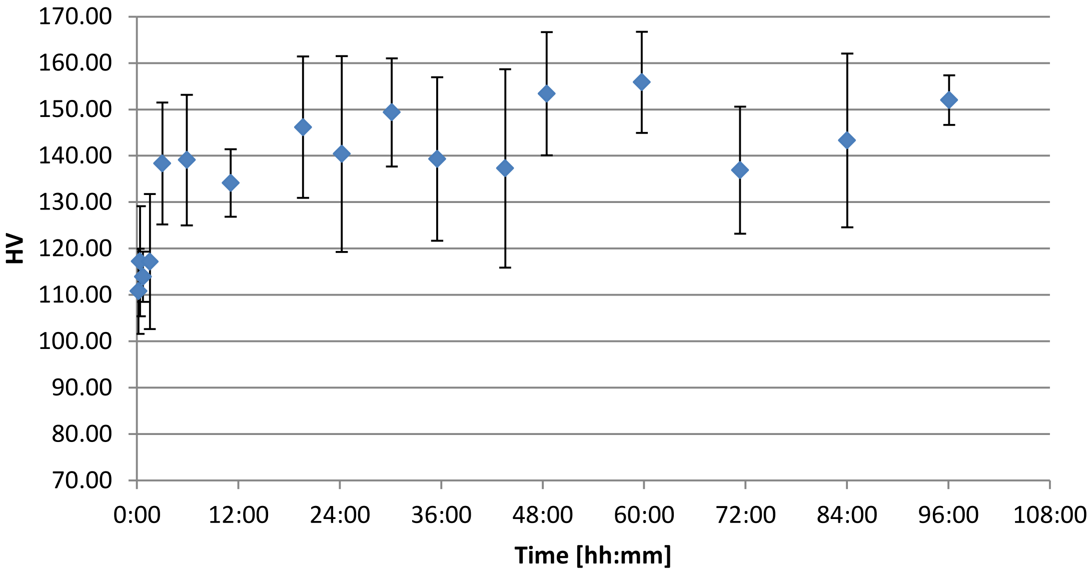

Figure 8.25: Microhardness evolution of Al-6Zn-2.2Mg-2.3Cu during artificial ageing, after 4 h of incubation period.

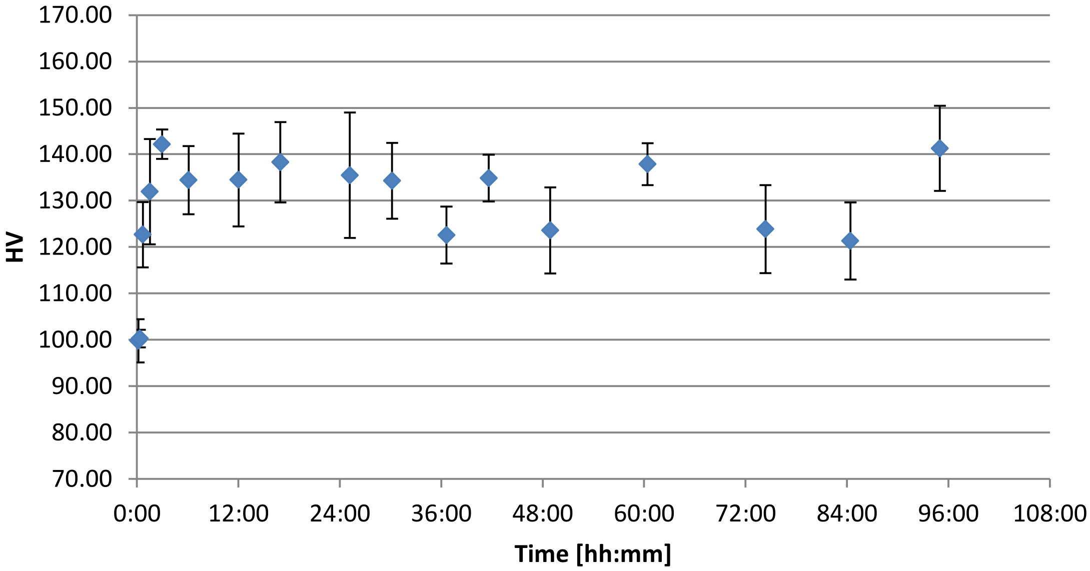

Figure 8.26: Microhardness evolution of Al-6Zn-2.2Mg-2.3Cu during artificial ageing, after 7 h of incubation period.

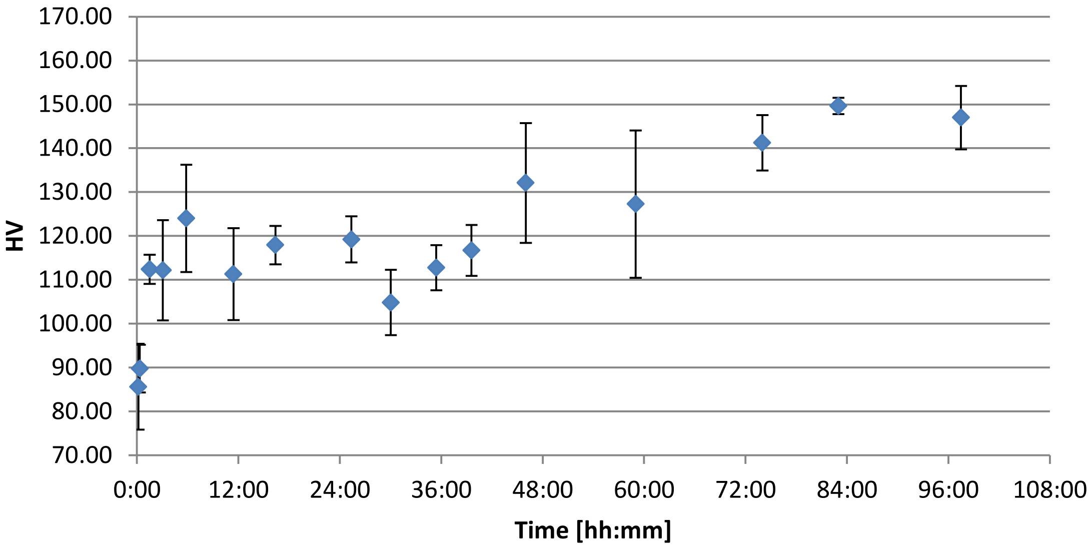

Figure 8.27: Microhardness evolution of Al-6Zn-2.2Mg-2.3Cu during artificial ageing, after 12 h of incubation period.

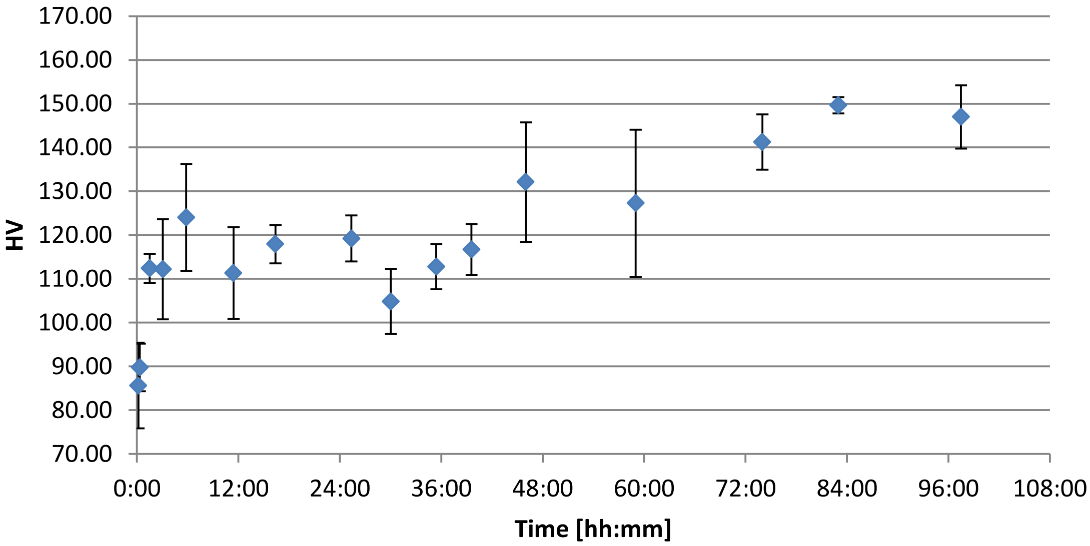

Figure 8.28: Microhardness evolution of Al-6Zn-2.2Mg-2.3Cu during artificial ageing, after 24 h of incubation period.

VITA AUCTORIS

Name: Luca Sobrino

Place of birth: Asti, Italy

Year of birth: 1990

Education: Liceo Scientifico “L. Cocito”, Alba, Italy, 2009

Politecnico di Torino, B.Sc in Automotive Engineering, Torino, Italy, 2012

Politecnico di Torino, M.A.Sc in Automotive Engineering, Torino, Italy, 2014

University of Windsor, M.A.Sc in Mechanical Engineering, Windsor, Canada, 2014